Development of micro-PIV techniques for applications in microfluidic systems

Hagsäter, Melker

Publication date:
2008

Document Version
Publisher's PDF, also known as Version of record

DTU Nanotech
Department of Micro- and Nanotechnology

PhD Thesis – s050745

Development of micro-PIV techniques for applications in microfluidic systems

Sven Melker Hagsäter

31 January 2008

Department
Department of Micro- and Nanotechnology
Technical University of Denmark

Supervisors
Professor Jörg P. Kutter
PhD Carsten Hein Westergaard
Professor Henrik Bruus

Thesis Defence
11 April 2008, 13:00
Building 341, auditorium 23
Technical University of Denmark

Assessment Committee
Assoc. Professor Kirstine Berg-Sørensen
Department of Physics
Technical University of Denmark, Denmark

Assoc. Professor Carl Meinhart
Department of Mechanical Engineering
University of California, Santa Barbara, USA

Assoc. Professor Johan Nilsson
Department of Electrical Measurements
Lund University, Sweden

Degree awarded
29 May 2008

For my parents and my grandparents

Abstract

Micron-resolution particle image velocimetry (micro-PIV) is a technique developed for measuring flow fields in microfluidic systems. The technique utilizes the motion of tracer particles, acquired from consecutive image frames recorded by a camera, to obtain two dimensional velocity vector fields with high spatial resolution. The success of micro total analysis systems (μTAS) depends on a proper understanding of the flow behavior inside these systems. Therefore, flow characterization methods play an important role in the development of microfluidic devices.

The aim of this thesis was to explore new improvements and developments of the micro-PIV technique itself, and furthermore, to apply the technique for relevant and novel investigations. This task has been tackled with an open-minded curiosity, and several different aspects of the measurement technique have been considered. This report describes the most important results, namely: (1) Investigations on micro-PIV with light emitting diode (LED) illumination. Different illumination strategies were examined, resulting in a novel front-lit configuration. Through various improvements, recordings with illumination pulse lengths down to 1 μs were feasible, which is more than a factor 10 shorter than what has been demonstrated in previous studies. The light source is typically the most expensive component in a micro-PIV setup, and therefore, the development of a low cost LED illumination system has increased the accessibility of the technique. (2) Examination of resonant patterns in acoustically actuated microdevices using full-image micro-PIV. An investigation approach was developed through which both acoustic radiation forces and acoustic streaming could be measured qualitatively. These experimental results were also compared with, and supported by, numerical solutions. Several different microdevices were investigated, and in particular important findings were made on the formation of acoustic resonances in straight separation channels. (3) A novel stereoscopic micro-PIV realization, using mm-sized mirror introduced in front of the microscope objective was developed and validated experimentally. The advantage with this system, compared to alternative stereoscopic micro-PIV realizations, is that it provides a high level of adaptability.

The overall goal of this project has been to popularize and contribute to the development of the micro-PIV technique.

Resumé

Particle image velocimetry med mikrometer opløsning (mikro-PIV) er en teknik, som er udviklet til at måle flowlinier i mikrofluide systemer. Denne teknik benytter sig af bevægelsen af tracer partikler, optaget med et kamera, til at danne et to-dimensionelt vektorhastighedsbillede med høj rumlig opløsning. En succesfuld udvikling af mikroanalysesystemer (μTAS) afhænger af en god forståelse for hvordan væske bevæger sig i disse systemer. Derfor spiller flow karakteriseringsmetoder, som denne en vigtig rolle.

Målet med denne afhandling har været at udvikle og undersøge mikro-PIV teknikken og at finde nye relevante anvendelsesområder. Denne opgave er blevet grebet an med nysgerrighed og et åbent sind og adskillige aspekter af måleteknikken er blevet undersøgt. Rapporten indeholder de vigtigste resultater, som er: (1) Undersøgelse af mikro-PIV med lysdiode (LED) illuminering. Forskellige lysindfaldsstrategier er blevet undersøgt, hvilket har resulteret i en ny forsidebelysningskonfiguration. Systemet er blevet optimeret til at kunne måle eksitationspulser ned til 1 μs, hvilket er mere end en størrelsesorden kortere end en hvad der har været demonstreret i tidligere studier. Lyskilden er typisk den dyreste komponent i et mikro-PIV setup. Derfor kan udviklingen af et billigt LED baseret system væsentligt øge udbredelsen af denne teknik. (2) Undersøgelse af resonansmønstre i akustisk aktuerede mikrokanaler ved brug af mikro-PIV. Herved kunne både acoustic radiation kræfter og acoustic streaming måles kvalitativt. Disse eksperimentelle resultater blev også sammenlignet og understøttet af numeriske beregninger. Adskillige slags mikrosystemer blev undersøgt og en af de vigtigste opdagelser var formation af akustiske resonansmønstre i lige kanaler. (3) Et nyt stereoskopisk mikro-PIV system, som benytter spejle på et par mm, mellem chip og mikroskop objektiv, er blevet udviklet og undersøgt eksperimentelt. Fordelen ved dette setup sammenlignet med alternative stereo mikro-PIV systemer er at det er meget let at tilpasse til forskellige typer eksperimenter.

Det overordnede mål med dette projekt har været at øge anvendelsesmulighederne for mikro-PIV og bidrage til den videre udvikling af denne spændende teknik.

Preface

This thesis is written as a requirement for obtaining the PhD degree at the Technical University of Denmark (DTU). The PhD project was performed at the Department of Micro- and Nanotechnology, from February 2005 to January 2008, within the ChemLabChip group. The PhD project was supervised by Prof. Jörg P. Kutter (main supervisor), Prof. Henrik Bruus and Dr. Carsten Hein Westergaard.

I would like to begin by sending a big THANK YOU to my three grand supervisors, whom each in their own way have been invaluable for my project. My appreciation also goes to all the people at the Department of Micro- and Nanotechnology, and most of all my colleagues in the ChemLabChip group. I would like to thank my senior colleagues Detlef Snakenborg and Klaus Bo Mogensen, who I have had the pleasure to share my office with, for their help with a lot of small things. In this context, I also would like to mention Fredrik Eriksson, Ómar Gústafsson, Fridolin Okkels and Henning Klank. My appreciation goes to Oliver Kuhn, who instructed me in the PIV technique during the spring of 2005, and to Thomas Glasdam Jensen and Peder Skafte-Pedersen for their contribution with the numerical analysis of acoustic phenomena. I also want to acknowledge my external collaborators: Martin Wiklund at the Royal Institute of Technology (KTH, Stockholm), who initiated our collaboration on acoustics, and Otto Manneberg for the work we did together; the staff at the Department of Electrical Measurements (LTH, Lund), in particular Andreas Lenshof, Thomas Laurell, Filip Petersson and Mikael Evander for many discussions on acoustics and several joint efforts; Fredrik Vestin and his colleagues at the division of combustion physics (LTH, Lund), who have assisted me with equipments and materials. I also would like to thank Fredrik for many discussions during the last years on matters related to research and that of being a researcher. My regards also go to the staff at Danchip, in particular Henrik Nielsen, Stig Ahrent Petersen and Helle Vendelbo Jensen. I wish to send special thanks to the administration and especially Peter B. Rasmussen who has always kindly helped me out with all sorts of things related to Danish bureaucracy. The Copenhagen Graduate School of Nanoscience and Nanotechnology and Dantec Dynamics should be acknowledged for financing my project. Last by certainly not least, I would like to express my appreciation for my lovely Katarina, without whom my life would have been very different.

S. Melker Hagsäter, 31 January 2008

Contents

List of Figures

List of Tables

List of symbols

Symbol	Description	Unit
c	Speed of sound	$\mathrm{m\,s^{-1}}$
f	Frequency	$\mathrm{Hz} = \mathrm{s^{-1}}$
F	Force	N
I	Image intensity	
NA	Numerical aperture	
p	Pressure	Pa
QE	Quantum efficiency	
QL	Quantization levels	bits
t	Time	s
t_p	Pulse length	s
T	Temperature	K
Δt	Time separation	s
u	Velocity	$\mathrm{m\,s^{-1}}$
U	Velocity	$\mathrm{m\,s^{-1}}$
v	Velocity	$\mathrm{m\,s^{-1}}$
V	Velocity or Volume	$\mathrm{m\,s^{-1}}$ or $\mathrm{m^3}$
V_{max}	Maximum velocity	$\mathrm{m\,s^{-1}}$
W	Velocity	$\mathrm{m\,s^{-1}}$
β	Compressibility	$\mathrm{Pa^{-1}}$
λ	Wavelength	m
η	Viscosity	Pa s
ρ	Mass density	$\mathrm{kg\,m^{-3}}$
Φ	Cross-correlation algorithm	
ω	Resonance frequency	$\mathrm{Hz} = \mathrm{s^{-1}}$

Chapter 1

Introduction

1.1 PIV – introduction

Particle image velocimetry (PIV) is a particle based flow visualization method, through which whole field velocity information can be obtained. The term PIV dates back to the mid 80's [1], and for a historical overview, the reader is recommended the review paper by Adrian [2]. Furthermore, the book *Particle image velocimetry - a practical guide* by Raffel *et al.* [3] (second edition released in 2007), provides an overview of the particle image velocimetry technique. I have only had the opportunity to evaluate the first edition of the book from 1998 [4], which also works well as an introduction to the technique, albeit parts of it are today mainly of historical interest. There is also another more recent book on PIV from the same research group [5].

In the following, a brief overview of the concepts of PIV relevant for the understanding of this thesis are presented. Even though my ambition is to strive for correctness, some simplified descriptions are used, where too much detail would unnecessarily muddle and complicate the understanding of the most important features. For instance, with respect to PIV recording techniques, only double frame/single exposure will be discussed.

1.2 PIV – working principle

In particle image velocimetry, tracer particles are used to obtain velocity information of a flow field. Depending on the application, different particles can be used, where the important feature of the tracers is that they move *with* the flow medium, rather than *in* the same. The measurement procedure is to make consecutive recordings (typically in sets of two image frames) of the seeding particles, with a time separation Δt in between. The velocity information can be obtained if the displacement of particles between consecutive recordings can be identified, since the length-scale of the system under investigation readily can be measured, and Δt is set by the user. Instead of identifying the displacement of individual particles, in PIV the image field is divided into interrogation regions of a certain size, and the displacement of all the particles within an interrogation region are considered. The basic principle of this procedure is illustrated in Fig. 1.1.

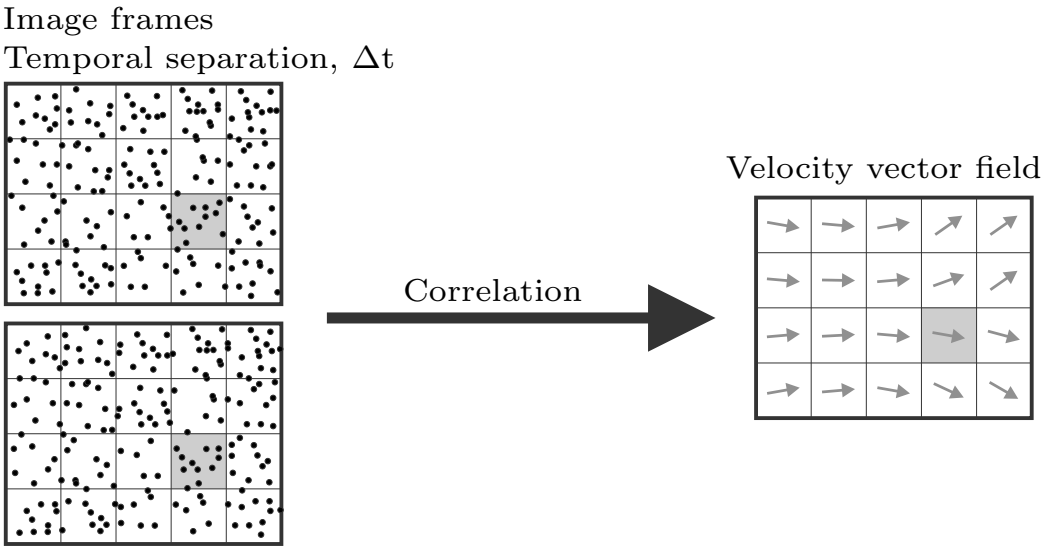

Figure 1.1: The basic principle of PIV analysis. Two image frames are recorded with a time separation Δt. The image frames are divided into interrogation regions, as indicated by the grid. One velocity vector is obtained for each interrogation region by correlation of the image frames. The result is a velocity vector field, as shown on the right of the figure.

More precisely, the displacement is found through cross-correlation of the images frames [4]:

$$\Phi(x,y) = \sum_{i=1}^{K}\sum_{j=1}^{L} I(i,j)I'(i+x,j+y). \tag{1.1}$$

I and I' are the image intensity values (gray values) for the two images frames, where i and j indicate the pixel position. $\Phi(x,y)$ is thus a measure of the similarity of the two interrogation regions (of size $K \times L$) for a displacement with respect to each other (x,y), where $(0,0)$ corresponds to no displacement. By calculating Φ for a range of displacements (x,y), a cross-correlation plane is formed, where the highest value (or peak) in this plane indicates the displacement of the particles.

For reference, it should be mentioned that the approach to identify the displacement of *individual* particles is also widely used. This method, denoted particle tracking velocimetry (PTV) [6], is sometimes described as a sub-technique of PIV. One requirement in "pure" PTV is that the displacement of the tracer particles between the recorded image frames needs to be smaller than the distance between the individual particles [7]. If this criterion is not fulfilled, it is not possible to separate the different particles from each other. Naturally, this requirement poses a limitation to the resolution of particle tracking velocimetry. However, as described by Keane *et al.* [6], if an estimate is first obtained by PIV analysis, it is thereafter possible to perform PTV with high spatial resolution.

1.3 Micro-PIV

Micron-resolution particle image velocimetry (micro-PIV) is essentially PIV analysis performed on micro-systems with a spatial resolution of the velocity measurements in the order of 1–10 microns [8]. Most of the equipment required for micro-PIV is common to that of a *standard* PIV setup. This includes: a **camera** (typically of CCD or CMOS type), a personal **computer** with **software** to handle the recording as well as to perform post processing of the images, and a **light source** (continuous or pulsed, typically a laser). However, in several ways micro-PIV differs from standard PIV, both in how the equipment is applied, and because certain physical phenomena are more pronounced in systems of these length scales.

First of all, in standard PIV the tracer particles are typically illuminated by a narrow laser light-sheet. The particles outside of this light-sheet are not illuminated, and thus, the measurement volume is well defined. In micro-PIV, however, physical and practical limitations prevent the creation of a light sheet within a device, and therefore so called volume illumination is typically applied [9]. The measurement depth is instead defined by the depth of focus of the microscope objective, but also other factors, such as the size of the tracer particles and the emission wavelength [10]. Volume illumination is a most important concept in micro-PIV, as it imposes limitations to both the accuracy and the applicability of the technique.

Secondly, the flow behavior in small scale systems is typically of laminar nature, equivalent to low Reynolds numbers (no turbulent effects). This implies that averaging over a series of consecutively recorded image sets often can be applied in micro-PIV analysis, as a means of increasing the measurement accuracy and resolution. This specific feature has also been demonstrated and utilized in several publications, for instance in the work by Meinhart *et al.* [11].

Other features, specific for micro-PIV, include the influence of Brownian motion [12, 13]. Brownian motion is especially important for small particles and short time intervals Δt. However, by averaging over several particles (as is the case within an interrogation region) and over several sets of recordings (as discussed above) the error due to Brownian motion can be reduced substantially.

For further reading, in [14] there is a chapter on micro-PIV written by Wereley and Meinhart, which at the time of writing is also available to download from the net. The previously mentioned book [3] also features material on micro-PIV in particular.

1.4 Outline of the thesis

- **Chap. 2: Micro-PIV with LED illumination**
  The way in which the illumination is applied in micro-PIV (microscope volume illumination) has an influence on the desired and required features of the light source. About a third of the PhD project was spent investigating low-cost illumination sources for micro-PIV. In particular, light emitting diode (LED) systems were studied. The most important outcome of this work was the realization of a front-lit configuration, which has substantially increased the applicability of micro-PIV with LED illumination. The main results from this study were summarized in the paper *Investigations on LED illumination for micro-PIV including a novel front-lit configuration* [15], as included in this chapter. Not least was the progress made within this area important for the continuation of my PhD project, where LED illumination has been used extensively.

- **Chap. 3: Additional material on micro-PIV with LED illumination**
  In this chapter additional material on micro-PIV with LED illumination is presented. The first part of the chapter provides a more in depth description of the light emitting diodes and the different illumination approaches and configurations that were used in this study. This include characterizations of LED pulse lengths and optical output, optimizations of LED power and a presentation of various LED products. The second part of the chapter elaborates on the topic of recording in scattered mode versus recording in fluorescent mode. Examples are provided of both, differences and common features between the two recording modes.

- **Chap. 4: Investigations of acoustic phenomena using micro-PIV**
  Acoustic forces can be utilized for several lab-on-a-chip applications, including basic functionalities such as pumping, separation, sorting, cleaning and mixing. The second major part of the PhD study has featured investigations of different acoustically actuated microfluidic devices. This chapter includes the paper *Acoustic resonances in microfluidic chips: full-image micro-PIV experiments and numerical simulations* [16], which provides an introduction to the topic and describes the method that was developed for investigation of these phenomena.

- **Chap. 5: Micro-PIV investigations of acoustic microdevices**
  The first part of this chapter is based on the paper *Acoustic resonances in straight micro-channels: Beyond the 1D-approximation* [17]. Here, the investigation scheme presented in [16] is applied for the examination of an acoustic separator, which makes it a logical continuation to that previous study. The second part of the chapter presents various examples comprising additional findings about both the acoustic effects in micrometer-scale systems, and the measurement approach which has been applied to investigate the same. These examples are included with the ambition to further broaden the understanding of acoustic devices, and emphasizing the knowledge about these systems, which has been obtained during the course of this PhD project.

- **Chap. 6: Stereoscopic micro-PIV**
  The third major part of the PhD study was devoted to stereoscopic micro-PIV. In this project, a novel approach for simultaneous recording of images of the same flow field from two separate views was investigated. This chapter is based on the paper *A compact viewing configuration for stereoscopic micro-PIV utilizing mm-sized mirrors* [18], which summarizes the final outcome of these efforts.

- **Chap. 7: Additional material on stereoscopic micro-PIV**
  This chapter describes some of the underlaying work that led to the stereoscopic realization presented in Chap. 6. This includes a presentation of earlier prototypes, details on the design process, and more information on the experimental arrangements. Finally, suggestions on further developments of the stereoscopic micro-PIV configuration presented in this study are provided.

1.5 Publications during the project

Papers in peer reviewed journals

1. *Investigations on LED illumination for micro-PIV including a novel front-lit configuration*
   S. M. Hagsäter, C. H. Westergaard, H. Bruus and J. P. Kutter
   Experiments in Fluids, 2008, **44**, 211–219.

2. *Acoustic resonances in microfluidic chips: full-image micro-PIV experiments and numerical simulations*
   S. M. Hagsäter, T. Glasdam Jensen, H. Bruus and J. P. Kutter
   Lab on a Chip, 2007, **7**, 1336–1344.

3. *Acoustic resonances in straight micro-channels: Beyond the 1D-approximation*
   S. M. Hagsäter, A. Lenshof, P. Skafte-Pedersen, J. P. Kutter, T. Laurell and H. Bruus
   Lab on a Chip, 2008, **8**, 1178–1184.

4. *A compact viewing configuration for stereoscopic micro-PIV utilizing mm-sized mirrors*
   S. M. Hagsäter, C. H. Westergaard, H. Bruus and J. P. Kutter
   Experiments in Fluids, 2008, **45**, 1015–1021.

5. *Spatial confinement of ultrasonic force fields in microfluidic channels*
   O. Manneberg, S. M. Hagsäter, J. Svennebring, H. M. Hertz, J. P. Kutter, H. Bruus and M. Wiklund
   Ultrasonics, 2008, DOI: 10.1016/j.ultras.2008.06.012.

Conference proceedings with peer review

1. *Full image microPIV analysis of transient and stationary flow patterns in microfluidic structures under piezo actuation*
   S. M. Sundin[1], T. Glasdam Jensen, H. Bruus and J. P. Kutter
   Proc. μTAS 2006, Tokyo, Japan, November 2006, vol. **1**, p. 47–49.

2. *A compact stereoscopic viewing configuration for micro-PIV utilizing mm-sized mirrors*
   S. M. Sundin[1], C. H. Westergaard, H. Bruus and J. P. Kutter
   7th international symposium on particle image velocimetry, Rome, Italy, September 2007.

[1] name hereafter changed to Hagsäter

Chapter 2

Micro-PIV with LED illumination

2.1 Introduction

The first part of the PhD project was a feasibility study of micro-PIV using LED illumination. This topic has been subject to little attention in previous work on micro-PIV, and the author is only familiar with one previous pulsed LED-system for this application, namely the Micro-Strobe from Dantec Dynamics. Compared to that system, major improvements have been made, both with respect to the applicability and the performance. In the following paper [15], presented in Sec. 2.2, the main findings of this study are described. Additional material is provided in Chap. 3.

2.2 S. M. Hagsäter *et al.*, Exp. Fluids, 2008, 44, 211–219

beginning of paper

Investigations on LED illumination for micro-PIV including a novel front-lit configuration

S. M. Hagsäter[1], C. H. Westergaard[2], H. Bruus[1], and J. P. Kutter[1]

[1] *MIC – Department of Micro- and Nanotechnology, DTU Bldg. 345 east, Technical University of Denmark, DK-2800 Kgs. Lyngby, Denmark*

[2] *Vestas Wind Systems A/S, Frederiksborgvej 399, 4000 Roskilde, Denmark*

In this study, we provide a general investigation on micro-PIV with LED illumination. A number of improvements over previous LED-based systems are suggested, in particular, we present a novel front-lit configuration. As a demonstration of its versatility we have used this front-lit configuration to perform micro-PIV measurements around a 50 μm squared pillar in a micro-channel with rectangular cross section, in both fluorescent mode and scattered mode. A comparison between the two modes is supplied, showing very good agreement between the respective velocity field results.

2.2.1 Introduction

Micro-PIV is a technique developed for measuring flow fields in microfluidic systems [8]. In a typical particle image velocimetry (PIV) experiment, a light sheet formed by a laser is used to illuminate only a section of the flow, where the thickness of the light sheet is smaller than the depth of focus of the image recording system. In most cases, this approach is impractical for micro-PIV, and instead so-called volume illumination is applied [9]. Here, the whole volume of the flow is illuminated, and now the depth of focus of the microscope objective defines the measurement region.

Dual cavity lasers, capable of delivering more than 10 mJ at pulse lengths typically in the range of 10–100 ns, originally developed for PIV, are also excellent for use in micro-PIV. However, for most microfluidic investigations the full capacity of these lasers is not utilized. Continuous light sources, such as arc lamps or CW-lasers, can also be used for volume illumination. Their applicability is highly dependant on the type of recording camera, but without the use of a shutter they are generally limited to low velocity flows.

In this article, we will show that light emitting diodes (LEDs) are well suited for micro-PIV, and a new, more versatile illumination configuration will be introduced. PIV with LED illumination is little described in the literature. Estevadeordal and Goss have demonstrated LED illumination PIV with shadows of particles in air-flow [19]. They also demonstrated measurements in pulse mode and supplied a discussion on some general considerations for PIV with LEDs. Chételat and Kim presented a MPIV (miniature PIV) system with LED illumination, also including a discussion on alternative illumination variants [20].

Since the experimental conditions in micro-PIV are considerably different to those in larger scale PIV, a separate investigation and description of LED illumination for micro-PIV is appropriate. There are a few previous micro-PIV studies where LEDs have been used as illumination sources, for example in the work of Singh *et al.* and Bitsch *et al.* [21, 22]. However, these articles did not consider specific aspects of the LED illumination configurations.

Compared to a standard PIV laser system, a LED system has several advantages: small size, adaptability to different fluorescent dyes (a range of wavelengths are available), incoherent light (no speckle or interference phenomena), freely adjustable pulse length and repetition rate, low energy consumption and very low cost. The main disadvantages are the lower light intensity, the broad wavelength spectrum and a broad spatial radiation pattern. Some of these problems can be dealt with by adjustments in the setup, as will be described in more detail below. With the ongoing developments in camera sensitivity as well as LED power, micro-PIV with LED illumination is poised to become a very promising and strong alternative to conventional laser-based systems. As a LED light source provides full freedom in terms of setting pulse lengths and repetition rates, our configuration is not limited to a specific type of application or camera, and it can also be used for other tasks where stroboscopic illumination in microscopy is required [23].

2.2.2 Illumination configurations and contrasting method

When applying LED illumination for micro-PIV analysis, both the illumination configuration and the contrasting method need to be chosen according to the optical and material properties of the sample under investigation. In this context, contrast is denoted as the ability to distinguish seeding particles from the background. By use of epi-fluorescent microscopy, with a barrier filter used to remove excitation light, emitted light from fluorescent particles on a dark background can be recorded. Realizations for micro-PIV using pulsed lasers, CW lasers and white light illumination are common. Obviously, these light sources are quite different in performance, and the excitation light source needs to be chosen in accordance with the requirements of the application. However, with respect to the measured signal the type of light source is relatively unimportant, since it is only used to excite the fluorescent dye embedded in the particles. If fluorescence is not used, contrast can be achieved by either strong scattering of light from particles on dark background, or by weak scattering of light from particles on a bright background of light coming from the backside, either directly or by reflection.

In this paper, we will demonstrate LED illumination applied for recordings of both fluorescent and scattered light, and moreover, supply a comparison between the two.

Principal configurations

In Fig. 2.1 the four principal micro-PIV illumination configurations studied in this work are presented: (a) front-lit configuration, (b) back-lit configuration and (c) and (d) two side-lit configurations. To get a better understanding of the illumination constraints specific to micro-PIV, these configurations should be compared with the description of illumination variants for the miniature PIV system, as supplied by Chételat and Kim [20].

Optical access is often limited when working with microfluidics. Fluidic connections, reservoirs and auxiliary equipments can clutter the workspace around the sample or chip. In all configurations 2.1(b–d) the positioning of the LEDs further limits this workspace. It is, therefore, preferable to work in front-lit mode, where the light from the illumination source is guided through the microscope, and it is in fact the most common choice in micro-PIV when a laser is used. In Fig. 2.1(a) such a configuration with a LED is presented. The light from the LED is reflected by the mirror in the filter cube of the microscope and is then focused by the objective onto the sample volume. This method, with LED illumination presented for the first time here, will be referred to as *front-lit configuration* and will be explained in more detail in Sec. 2.2.2 – Novel front-lit configuration.

In Fig. 2.1(b) a back-lit configuration, as presented by Bitsch *et al.* [22], is shown. In their system, a single high power LED (Lumileds Luxeon Star, 1W) was used, placed behind a frosted glass plate to diffuse the light, in close proximity to the backside of the sample. Clearly, this configuration has a limitation in that it can only be used for transparent samples. The usability is further limited by the fact that the illuminator needs to be realigned if the sample, or the illuminator, is moved. However, with simple adaptations this setup can be improved, as will be explained in Sec. 2.2.2 – Improved back-lit configuration.

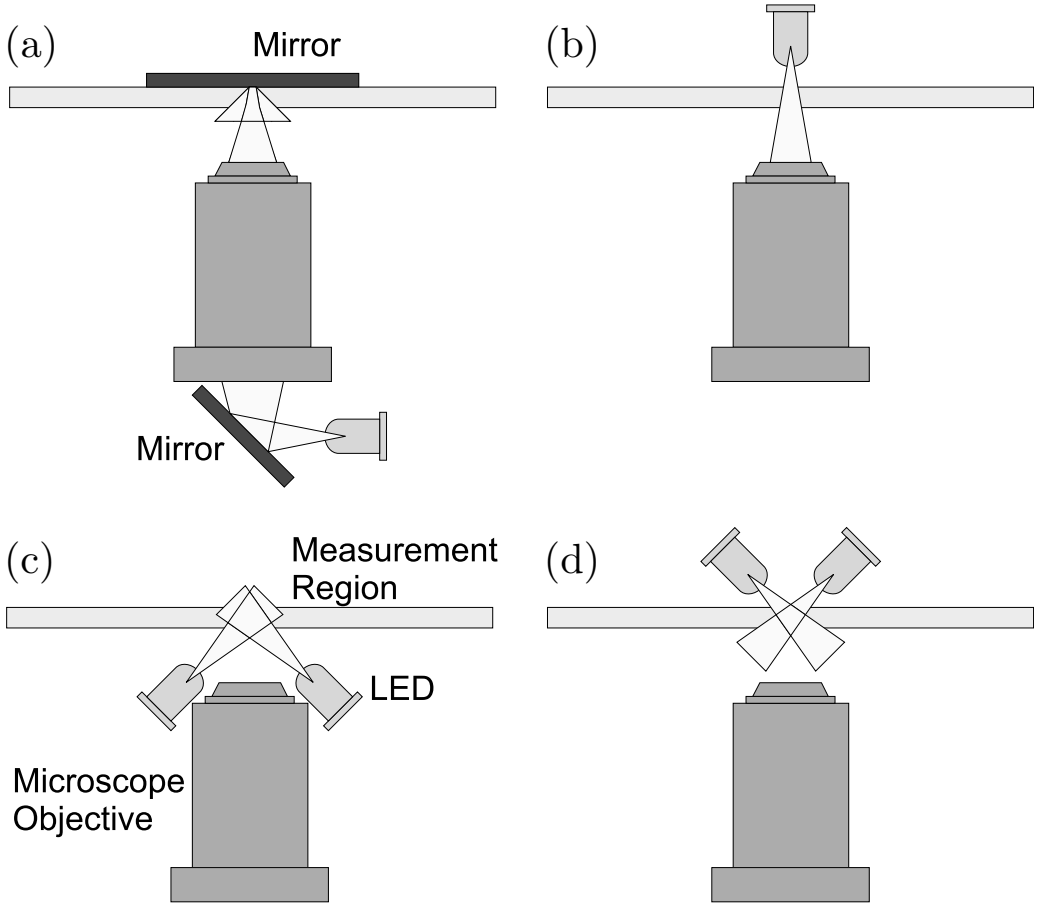

Figure 2.1: (a) Front-lit illumination with a reflector behind the substrate. Note that the figure shows a simplification of the positions of the mirror and the LED. (b) Back-lit illumination. (c) Side illumination from objective side. (d) Side illumination from backside of substrate.

In micro-PIV, it is generally physically not possible to apply side illumination perpendicular to the viewing angle of the microscope objective. Instead, side illumination will either be applied from the backside or the front side of the sample as shown in Figs. 2.1(c) and (d), respectively. A system as shown in Fig. 2.1(c), with a ring of 24 LEDs, has been demonstrated by Singh *et al.* [21], and is also utilized in the LabSmith SVM340 video microscope [24]. One drawback with this method is that the light distribution to the investigation volume decreases drastically for higher magnification objectives with shorter working distances, as the diodes then need to be placed at a small angle with respect to the object plane. Another drawback is that in order to achieve an even illumination with side illumination, several diodes, which need to be aligned around the objective, are required. For low magnification, long working distance objectives, and for special applications, side-illumination can still be advantageous, but in this study it is not investigated further.

Novel front-lit configuration

In the front-lit configuration the LED is coupled to the microscope using the optical pathway of a standard epi-fluorescent microscope. In this way, a more rigid system is obtained, as the light source does not need to be realigned every time the substrate under investigation is moved or the microscope objective is exchanged. Moreover, the workspace around the sample or chip is not further limited in this configuration.

The light from a LED is not collimated, but is spreading at a relatively large angle, and consequently the luminous flux diminishes rapidly with increasing distance from the light source [25]. This causes a problem in the front-lit configuration, where the LED needs to be placed relatively far away from the microfluidic system. Moreover, the radiation pattern is typically Lambertian, with a very strong central intensity.

If a LED is placed directly behind the rear lamp house port of an epi-fluorescent microscope, the LED will only illuminate a limited part of the field of view. In order to achieve a more uniform light distribution, expander optics are required, and in this study we have used a fiber adapter. With this solution a larger fraction of the light can be utilized, but if the LED is not aligned accurately, the setup will still produce a curved light intensity distribution over the field of investigation. For the experiments in this study the LED was mounted on a xyz optical stage, which allowed the LED to be fine-positioned while light intensity and distribution were observed by the camera. One way to achieve a flat illumination distribution is by putting a diffuser into the beam path. However, this causes an overall decrease of the illumination intensity over the entire field, and is therefore not recommended.

In the front-lit configuration, you can readily switch between recording fluorescent and scattered light, by exchanging the microscope filter cube. The two filter cubes used in this study are described in Fig. 2.2. It should be noted that the illumination intensity with the bright field filter cube inserted is not the same as when the I3 filter cube is inserted. This is due to the fact that in the first case, the mirror in the filter cube is a 50–50 beam splitter (half of the light is transmitted and half is reflected), whereas in the second case the mirror is dichroic (reflection or transmission depending on wavelength of incident light).

In the case of scattered light measurements, the most important factor that determines the contrast between the seeding particles and the background is the light reflecting properties of the substrate. This is true both in the situation with extinction of light (background will be even brighter with a more reflective substrate), and in the situation with scattering of light (backward scatter is much weaker than forward scatter). For transparent samples, when the front-lit configuration is preferred over the back-lit configuration, a mirror placed behind the chip can be used as a reflector. This has been shown to be a practical approach (see Sec. 2.2.4). With an upright microscope this can be readily achieved by affixing a mirror to the optical stage of the microscope. If the substrate is a naturally non-transparent reflector, such as silicon, the bottom of the microfluidic device itself functions as a mirror. However, if a flow close to a reflecting boundary is to be inspected, it should be remembered that the images of reflected particles can contribute to the correlation.

In the case of fluorescent light measurements, the fluorescent signal depends on the level

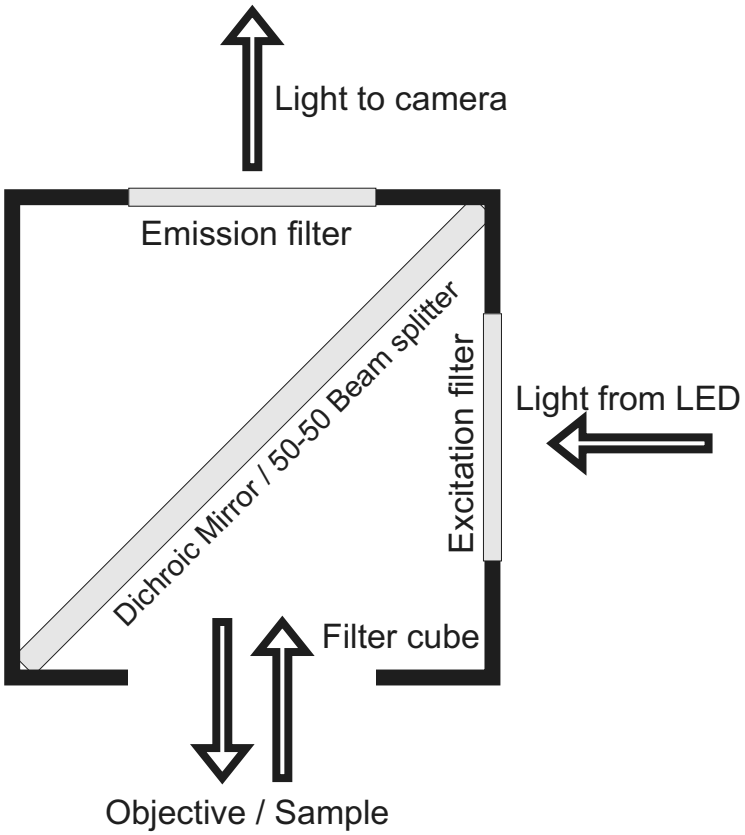

Figure 2.2: A sketch of a microscope filter cube. The I3 filter cube has a band pass excitation filter, 450–490 nm, a dichroic mirror, 510 nm, and a long pass emission filter, 515 nm. The bright field, BF, filter cube has no excitation or emission filter, and it has a 50–50 beam splitter instead of a dichroic mirror.

of light exposure of the particles. Moreover, the type of fluorescent dye and the amount of dye per particle is of major importance in determining the achievable contrast. Micro-PIV in fluorescent mode is a standard method, and it has been described in numerous publications (e.g., Santiago *et al.*) [8].

Improved back-lit configuration

The drawbacks of the back-lit configuration as used in previous studies [22] are that transparent samples are required, and that the illumination source needs to be placed close to the backside of the microfluidic device. This requirement limits the workspace around the chip, because fluidic connections, reservoirs, and other equipment clutter the region in which the LED needs to be placed. The way the chip is cramped in between the microscope objective and the light source also makes the setup vulnerable, and if the chip is moved, or replaced, it is likely that the alignment of the light source needs

to be re-adjusted. Regarding the first requirement, i.e., a transparent sample, this can obviously not be relaxed. However, with the use of optics it is possible to get around the problem with the proximity of the light source. In this study, a low-cost plastic lens, specially designed for Luxeon diodes, was chosen. With such a lens, which focuses the light, the diode can be moved much further away from the chip, while still achieving a high light intensity and a relatively flat intensity profile over the whole illuminated region. In comparison with the close proximity setup, this setup can therefore be used in a larger number of applications, is easier to align and much less sensitive to disturbances.

Additionally, if recordings of fluorescent light are to be made, an excitation filter needs to be fitted between the LED and the sample. This was not attempted in this study; here, the back-lit configuration was only used for recordings of scattered light.

2.2.3 Materials and methods

Experimental setup

Images were recorded with a HiSense MkII progressive scan interline CCD camera (Dantec Dynamics), mounted with a 0.63× TV-adapter on an epi-fluorescent microscope (Leica DMLB). Objectives used were: N Plan 10×, N Plan L 20× and PL Fluotar L 63× with numerical apertures (NA) of 0.25, 0.40 and 0.70, respectively. In the front-lit configuration, a blue LED (Lumileds Luxeon K2) was aligned with a xyz optical stage to a fiber adapter with expander optics mounted on the rear lamp port of the microscope. The filter cubes inserted into the optical path were bright field, BF, and I3 (Leica) for recordings in scattered mode and fluorescent mode, respectively (see Fig. 2.2). In the improved back-lit configuration, on the other hand, the LED was placed below the substrate, and a plastic focusing lens (Carclo-Optics, 20 mm fiber coupling optic) was used.

The LED was powered by an in-house built power supply and controlled by a PIV timing system (Dantec Dynamics). If the diode is set to emit light for very short pulse durations, a much higher power than what would be possible for continuous illumination can be used. In the experiments described in this paper, a power supply designed to deliver a power of 26.4 W over the diode was used.

Image acquisition was performed on a PC with Flowmanager software (Dantec Dynamics). A small planar mirror was used for some of the measurements in the front-lit configuration. For reference, green fluorescent polystyrene particles (1 μm diameter, Duke Scientific) were used in all experiments, even though the fluorescent signal was not distinguishable when the bright field filter cube was inserted. For the contrast measurements, particles adhering to the coverslips of glass slides were used, similar to what was described by Meinhart *et al.* [9]. For the micro-PIV comparison the flow around a 50 μm squared pillar in a 400 μm wide and 200 μm deep microfluidic channel, fabricated in silicon via deep reactive ion etching (DRIE), was measured. Anodic bonding was used to seal the structure with a 500 μm thick pyrex glass lid on the channel side. A sketch of the whole system with the LED mounted for front-lit illumination, can be seen in Fig. 2.3.

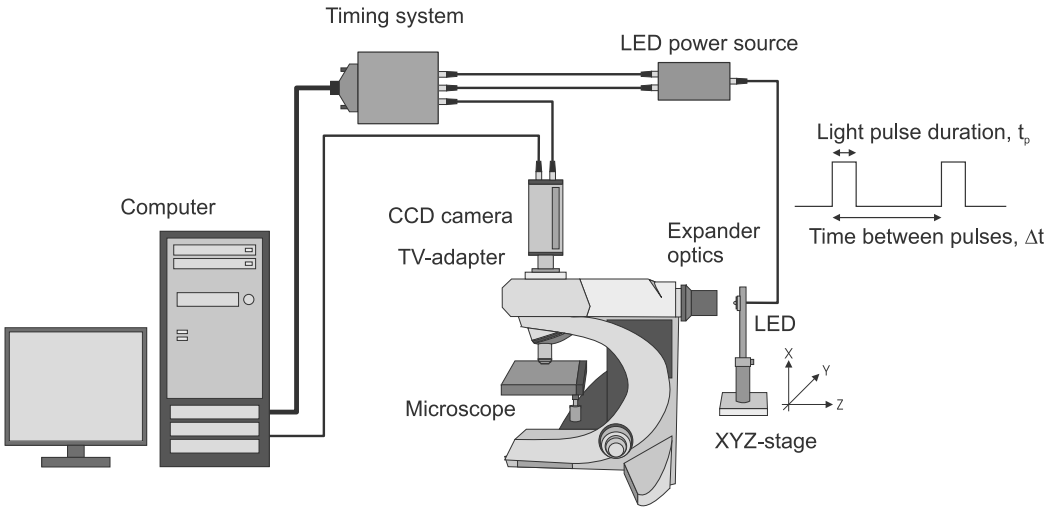

Figure 2.3: The micro-PIV setup used in the experiments. The LED is positioned as used in the front-lit configuration. Light pulses are synchronized individually with the camera. The camera is running in PIV mode, separating images into image pairs.

Optical power and contrast

The different ways in which contrast between the particles and the background can be enhanced, were described in Sec. 2.2.2. Independent of the method used, the contrast, or image quantization (i.e., bits/pixel), is dependant on the level of illumination. As shown by Willert [26], the image quantization has only a minor influence on the measurement uncertainty in PIV, and an increase from 4 to 8 bits/pixel has hardly any influence on the measurement accuracy. This result is intriguing when comparing LEDs with lasers, because the former delivers considerably less light during short pulse lengths (t_p). If time averaging is used, even lower quantization levels are sufficient [11]. On the other hand, for super-resolution PIV and particle tracking velocimetry (PTV), larger contrast is beneficial [6].

It should be noted that the usable power can differ immensely between different batches of diodes, and even within diodes from the same batch. This has been shown by Benavides and Webb [27], who have characterized Luxeon diodes. In this study, the primary interest was to compare the illumination properties between different substrates and configurations, and not between different diodes. Therefore, the same diode was used for all measurements presented in this article. The rise time for Luxeon diodes is less than 100 ns, so a pulse length down to 1 μs, which was the shortest one used in this study, is feasible [25]. This has previously been shown by other groups [19, 27].

Even when the diode is properly aligned and is given sufficient power, the limitations for using LED illumination still depend to a large extent on the properties of the sample under investigation, the particle density, the properties of the tracer particles, the recording system/camera, the applied recording technique, and the requirements on measurement

accuracy. Therefore, highly specific limitations for LED illumination in micro-PIV cannot be given. However, if applied correctly, LED illumination can undoubtedly represent an alternative to other illumination sources for many applications, as evidenced by the results presented below. A guiding comparison between different light sources (calculated for a thin reflecting device under idealized conditions), can be found in Table 2.1. The numbers are given for a highly sensitive CCD camera, with a pixel size of 7×7 μm^2. Maximum velocities are calculated for a maximum particle displacement of 1 pixel during exposure, avoiding motion blur.

Table 2.1: Comparison between different light sources, where "Min t_p" is the pulse length limitation of the light source, and L. E. R. "Light exposure required" is the minimum exposure time required by the camera (HiSense MkII).

Light source	Min t_p	L. E. R.	V_{max} 10×	V_{max} 63×
Laser, Nd:YAG, flash lamp	∼10 ns	∼10 ns	70 m/s	11 m/s
High power LED (scatter)	∼100 ns	>1 μs	0.7 m/s	0.11 m/s
Normal power LED (scatter)	∼100 ns	>20 μs	35 mm/s	5.6 mm/s
Lamp with mechanical shutter	∼5 ms	<1 ms	140 μm/s	22 μm/s
Lamp with video camera	25 ms[a]	–	28 μm/s	4.4 μm/s

V_{max} is calculated for 10× and 63× magnification using 1 μm particles, and is calculated from the limiting factor of the system (Min t_p or Light exposure required)
[a]Video interframe time

2.2.4 Results

In Fig. 2.4, normalized spectral light distributions measured below the microscope objective and behind the camera adapter are shown. By comparing spectra (a) and (b) it is seen that the I3 filter cube excitation filter effectively blocks the light from the diode above 500 nm, and thus the camera will only record a fluorescent signal.

The fluorescent particles used in this study have their peak emission wavelength at 508 nm, with a Stokes shift of 40 nm, which is a typical value for fluorescent particles. Nonetheless, a large portion of the emitted light is lost in the I3 filter cube, which is seen by subtracting spectrum (b) from spectrum (c) and comparing the result with spectrum (d). This loss is not an effect from LED illumination in particular, and the same loss is to be expected if a laser is used as excitation source. However, since the optical power is a limiting factor in the case of LED illumination, and typically not so in the case of laser illumination, it would be interesting to explore how much of the emitted light could be collected by using customized filter cubes and particles.

Figure 2.5 shows two images of particles adhered to the cover slip of a glass slide, recorded with a 10× and a 63× magnification objective, respectively. From a range of such images, while using different objectives (10×, 20× and 63×) and pulse lengths (from 1 to 100 μs with the bright field filter cube, and from 50 μs to 2 ms with the I3 filter cube), quantization levels of particles for each combination were estimated manually. The results from these measurements are shown in Fig. 2.6. Three different substrates were

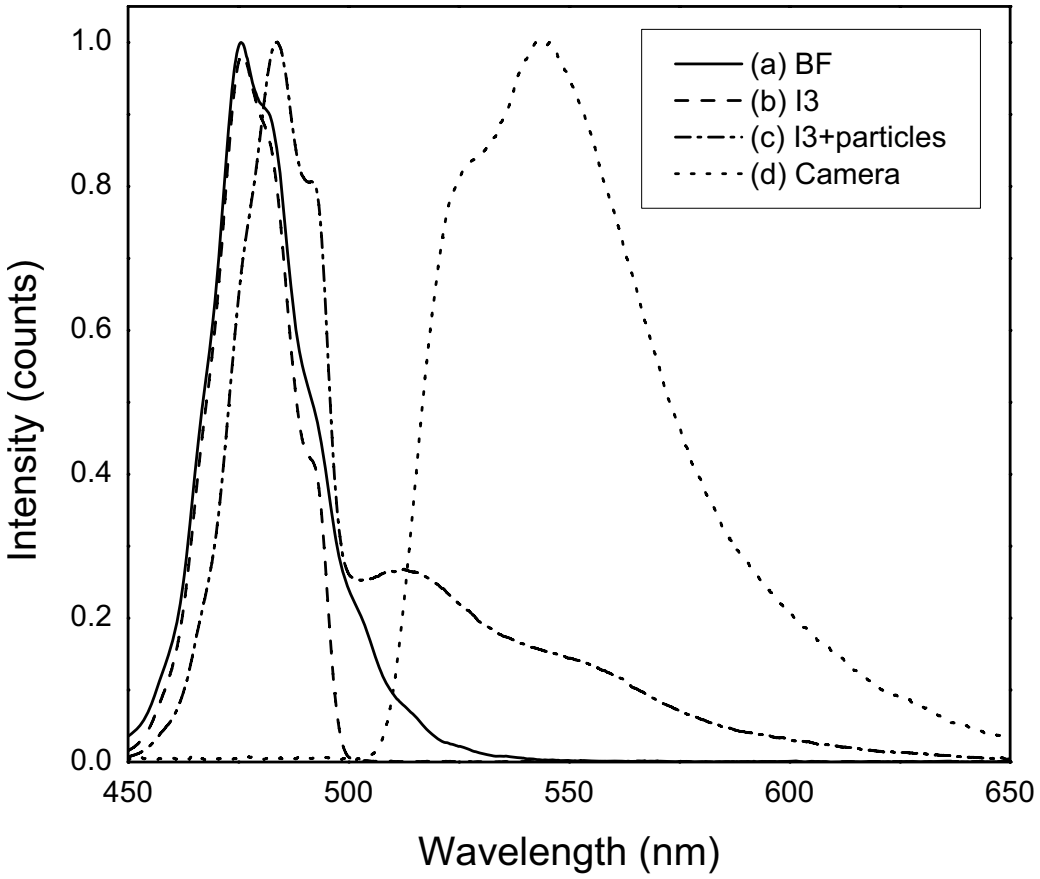

Figure 2.4: Normalized spectra of scattered light from a mirror placed below the microscope objective with (a), bright field filter cube inserted, and (b), I3 filter cube inserted. In (c) and (d), a drop containing fluorescent particles is placed underneath the microscope objective. Spectrum (c) is recorded with the spectrometer placed in close proximity to the side of the microscope objective (same as in (a) and (b)), whereas (d) is recorded with the spectrometer placed after the emission filter (in the position of the camera). Since spectra (b) and (d) have no overlap, it can be concluded that spectrum (d) is composed of fluorescent signal only.

investigated in the front-lit configuration: cover slips on glass slides with no reflector, cover slips on glass slides placed on a mirror, and cover slips placed directly on a silicon substrate, i.e., a diced silicon wafer. Moreover, the transparent sample was also measured with the three objectives in the improved back-lit configuration. However, in this configuration no fluorescent measurements were attempted.

As can be seen, for the front-lit configuration measurements on scattered light, the contrast (as expressed by the quantization levels, QL) decreases with increasing magnification of the objective (Figs. 2.6(a–c)). However, for scattered light measurements the substrate material is the most important factor. With the 10× and the 20× magnification objectives and transparent samples, a 20 times longer pulse length is required to obtain

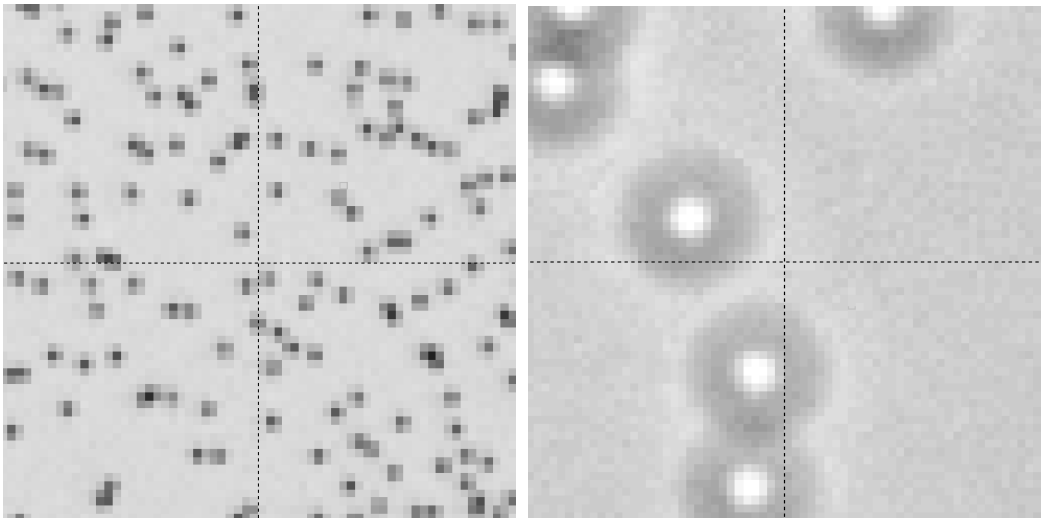

Figure 2.5: Images of 1 μm particles adhering to the coverslip of a glass slide recorded with (a) a 10× objective and (b) a 63× objective. For these particular recordings a mirror was used as reflector. The grid is shown for 32×32 pixels.

the same contrast as when a mirror is used as back reflector. For the transparent samples without a reflector, a t_p of more than 100 μs was needed with the 63× objective in order to get at least $QL = 4$, and these values are therefore not included in the figure.

Typically, a much longer pulse length is required to obtain the same contrast when fluorescent light is recorded, compared to when scattered light is recorded (Fig. 2.6, open symbols compared to filled symbols). However, fluorescent measurements are highly dependant on the nature and size of the particles used. As the 63× magnification objective has a significantly shorter focal length then the two other objectives, the thickness of the substrate layer plays a most important role in this case. Therefore, the measurements in Fig. 2.6(c) are highly specific for the investigated substrates in this study. It should also be considered that for micro-PIV measurements, the optimal size of the tracer particles, with respect to the measurement uncertainty, depends on the microscope magnification [4]. In this study, however, the same 1 μm particles were used in all of the measurements.

In these experiments we used the Dantec HiSense MKII camera with the Sony150ER CCD sensor, having a dynamic range of 1:1800 at a peak quantum efficiency of 70%. In practical PIV terms this camera performs quite similar to the PCO SensiCam QE with the Sony ICX265 CCD having a dynamic range of 1:3000 at a peak quantum efficiency of 62%. These are both about twice as effective as the previous camera generation based on the ICX061 CCDs with a dynamic range of ∼1:1000 and a quantum efficiency of ∼50%. Compared to the newer and current camera generations based on the Kodak KAI series CCDs having a typical dynamic range of ∼1:1200 and a quantum efficiency of ∼55%, the newer cameras are approximately 1.5 times less efficient than the one used in this

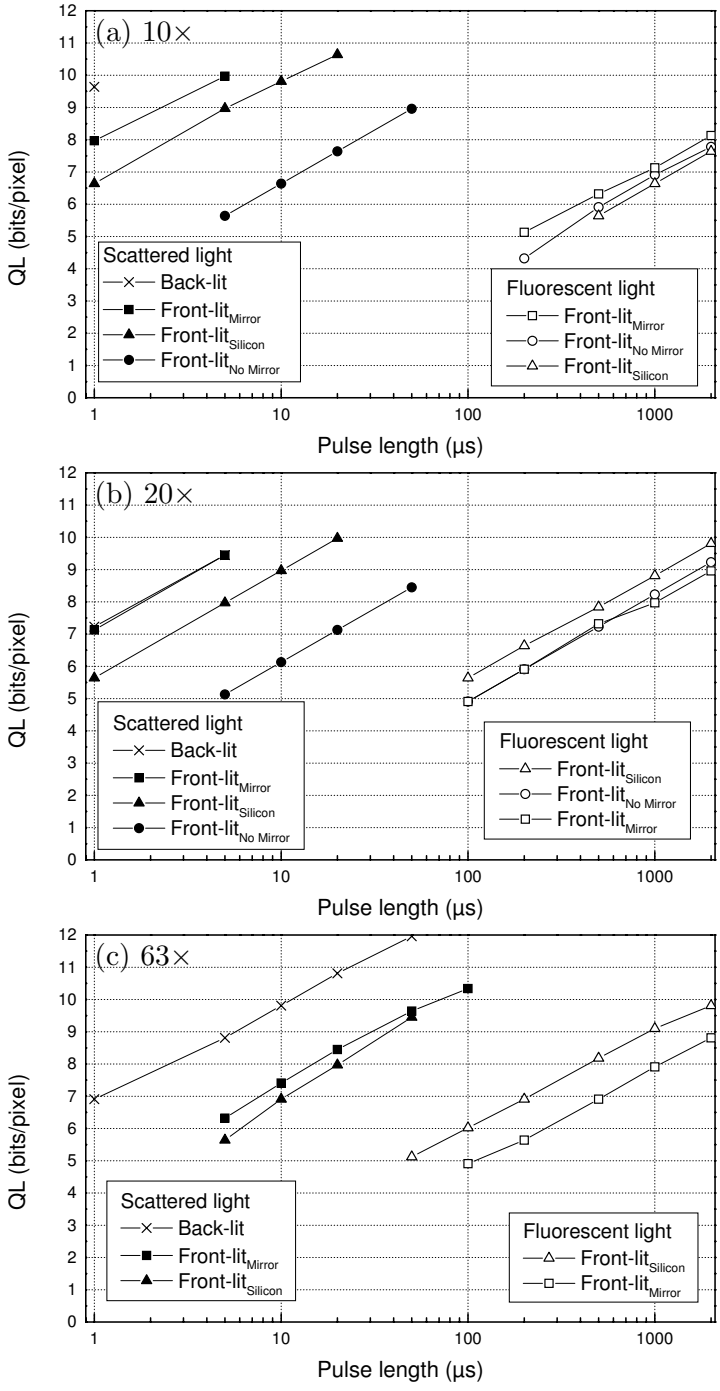

Figure 2.6: Quantization levels (QL) for particle images with (a) a 10× objective, (b) a 20× objective and (c) a 63× objective in the front-lit and back-lit configurations. Note that the y-axis increments are not linear but represent a $\log_2$ scale.

study. Note that the quantum efficiency and dynamic range are sufficient numbers when comparing similar sensors, but one has to be careful not to extrapolate these numbers to other types of cameras/sensors without considering all details of the specifications.

In the last experiment, LED illuminated micro-PIV was used to measure flow velocity around a square pillar, 50 μm on the side, positioned in the middle of a micro-channel, 400 μm wide and 200 μm deep, fabricated in silicon. The flow was driven by a syringe pump (Harvard), with the flow rate set at 0.2 ml/h, and PVC tubes were used as connections to the microdevice. The flow was seeded with 1 μm polystyrene particles, diluted in water to a concentration of 0.25%. In these measurements, the 0.63× TV-adapter and the 63× microscope objective were used, providing a field of view of 218×166 μm. The flow of particles was recorded at a depth of ∼45 μm, both in scattered and fluorescent mode, after background removal providing images as seen in Figs. 2.7(a) and (b). In each mode, 100 double image frames were recorded with a t_p of 100 μs, and a time between pulses of 1 ms. Vectors were calculated for each double image frame, using the adaptive correlation method (initial interrogation area size: 128×128 pixels), with a final interrogation area size of 64×64 pixels, 50 % overlap. The depth of correlation, as given by Olsen and Adrian [10], was calculated to be ∼6.0 μm for the fluorescent measurements, and ∼5.5 μm for the scatter measurements. After removing erroneous velocity vectors through peak validation, the average velocity was calculated for both sets of 100 double image frames [11], which resulted in two well matched velocity vector fields, each 31×39 vectors. A comparison between the two modes is seen in Fig. 2.8, where velocity plots of the u and v velocities for five different cross-sections over the width of the channel are seen. For each cross-section, the average and the maximum difference between the measured velocities in u and v are presented. Considering a bulk flow of ∼1,000 μm/s the magnitudes of these values indicate the excellent agreement between velocities calculated from, respectively, fluorescent and scattered light measurements. Moreover, it demonstrates the feasibility of both recording techniques, as well as the general applicability of micro-PIV with LED illumination. It is worthy to stress again that a pulse length of 100 μs was chosen to facilitate the comparison between the measurements in scattered and fluorescent mode. High-contrast measurements with much shorter pulse lengths are feasible in the scattered mode (especially with low magnification objectives), thus easily allowing LED illuminated PIV measurements for other microfluidic systems with flow velocities much higher than those demonstrated here (mm/s – dm/s).

2.2.5 Conclusions

In this study, we have shown that light emitting diodes are well suited as illumination sources for micro-PIV measurements. In particular, with the introduction of the *front-lit configuration*, which does not require transparent samples or otherwise imposes limitations to the workspace, the applicability of LEDs has been further improved. Moreover, through improved alignment and the use of higher output powers, we have shown that in scattered mode pulse lengths down to 1 μs are practical, which is more than a factor 10 shorter than what has been shown in previous studies. A comparison between measurements in scattered mode and fluorescent mode was also provided, showing excellent agreement

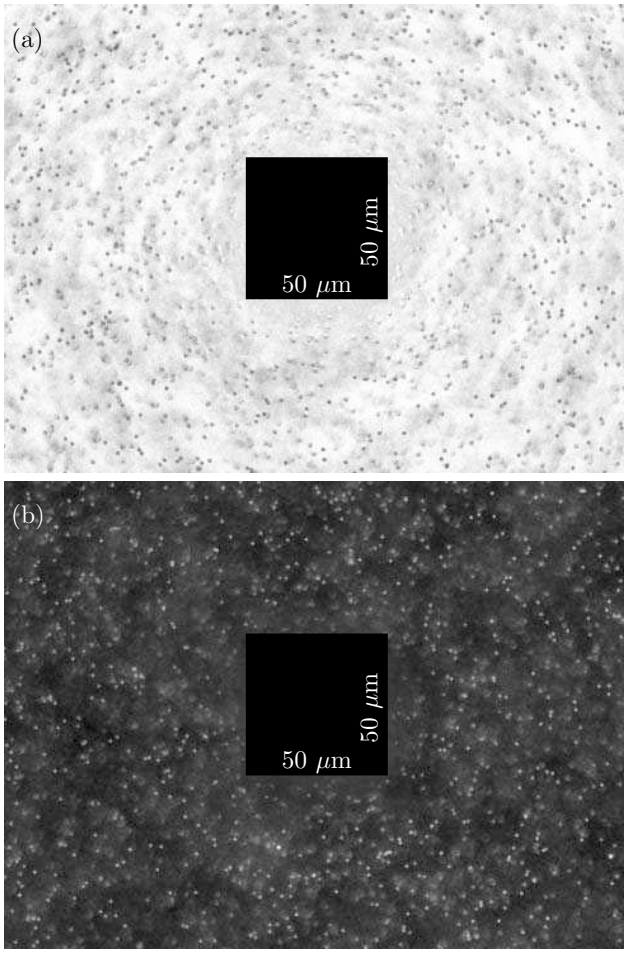

Figure 2.7: Background subtracted image frames of 1 μm particles flowing around a 50 μm×50 μm pillar structure at a depth of 45 μm. (a) Picture recorded in scattered mode, the bright field filter cube is inserted, and the particles appear dark in relation to the background. (b) Picture recorded in fluorescent mode, the I3 filter cube is inserted, and the particles appear bright in relation to the background. Both images are recorded with a t_p of 100 μs.

between the two. The main benefit of the scattered mode over the fluorescent mode when applying LED illumination is that faster flows can be measured.

Due to the large variety in design, materials and fabrication approaches, as well as in the restrictions and demands on the measurements, it is not possible to give a universal answer as to for which micro-PIV measurements a LED can be used or may be advantageous compared to a laser. However, with continuing developments towards increased camera sensitivity as well as towards even brighter LEDs, light emitting diodes have the potential to become even more competitive to other illumination light sources.

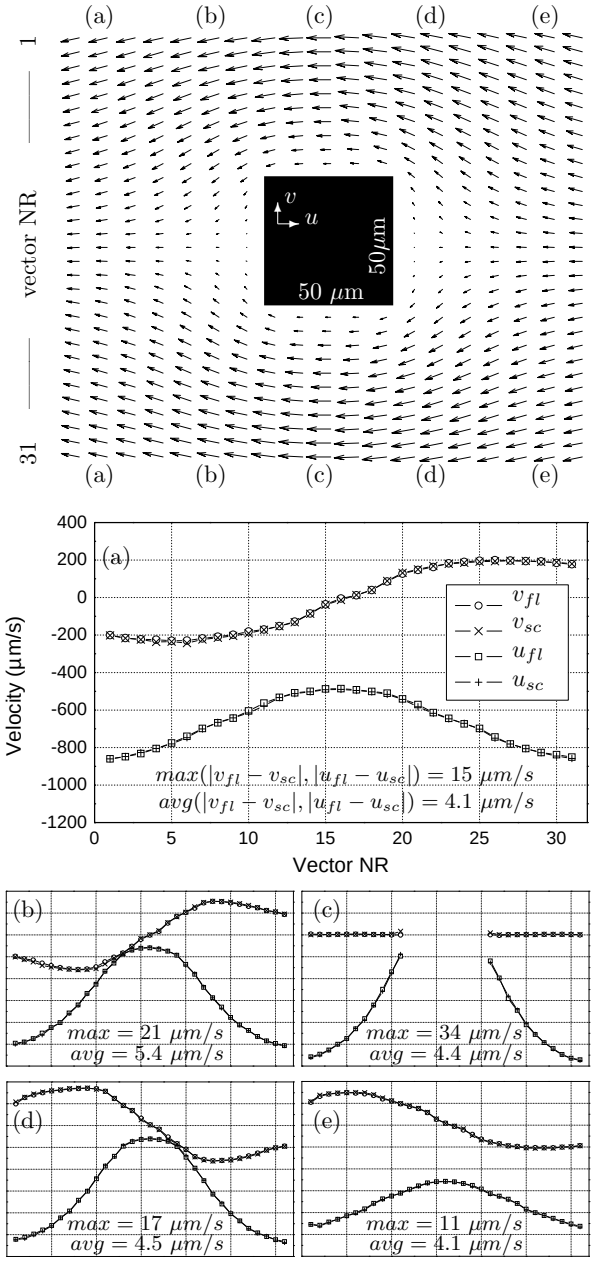

Figure 2.8: Top panel shows velocity vector fields around a 50 μm×50 μm pillar recorded in fluorescent mode. For clarity, only every second velocity vector in the channel flow direction is shown. Unit vectors equal 1 mm/s. A comparison between velocity vectors calculated from images recorded in fluorescent $_{fl}$ mode and scattered $_{sc}$ mode is seen in panels (a)–(e). The plots are showing the u and v velocities for five different cross sections over the width of the channel. The scale bars and symbols in panels (b)–(e) are the same as in panel (a), even though not shown.

Acknowledgement

SMH was supported through Copenhagen Graduate School for Nanoscience and Nanotechnology, in a collaboration between Dantec Dynamics A/S and MIC, Technical University of Denmark.

end of paper

Chapter 3

Additional material on micro-PIV with LED illumination

The most important findings concerning micro-PIV with LED illumination are well covered in Chap. 2. This chapter will provide a more detailed description of some of the features described in the previous chapter, and additional material intended to serve as a starting point for further studies.

The first section, 3.1 *LED – Materials and methods*, is devoted to explaining various improvements of LED illumination for micro-PIV that have been made during the course of this PhD study. This includes modifications using new equipment and other optimizations of the experimental conditions. It also comprises advancements made with respect to usable LED optical power and more efficient sample illumination. The second section, 3.2 *Fluorescent versus scattered mode*, will elaborate on the differences between recording in fluorescent mode and scattered mode.

3.1 LED – materials and methods

3.1.1 Position of LED behind adapter

As briefly mentioned in Chap. 2, the positioning of the LED in the front-lit configuration affects the intensity profile over the illuminated region. Adjustments in x- and y-directions only cause a lateral displacement of the illumination pattern, whereas movements in z-direction affect the curvature of the intensity profile, as illustrated in Fig. 3.1. As can be seen, the 40 mm position gives a fairly flat illumination and has the highest intensity of the four positions at the edges. On the other hand, if only the center of the field-of-view is of interest, then the 36 mm position could be favorable. Thus, the optimal LED position on the z-axis depends on the application. Naturally, the specific absolute numbers for the LED positions are only valid for the particular expander optics that were used in this study.

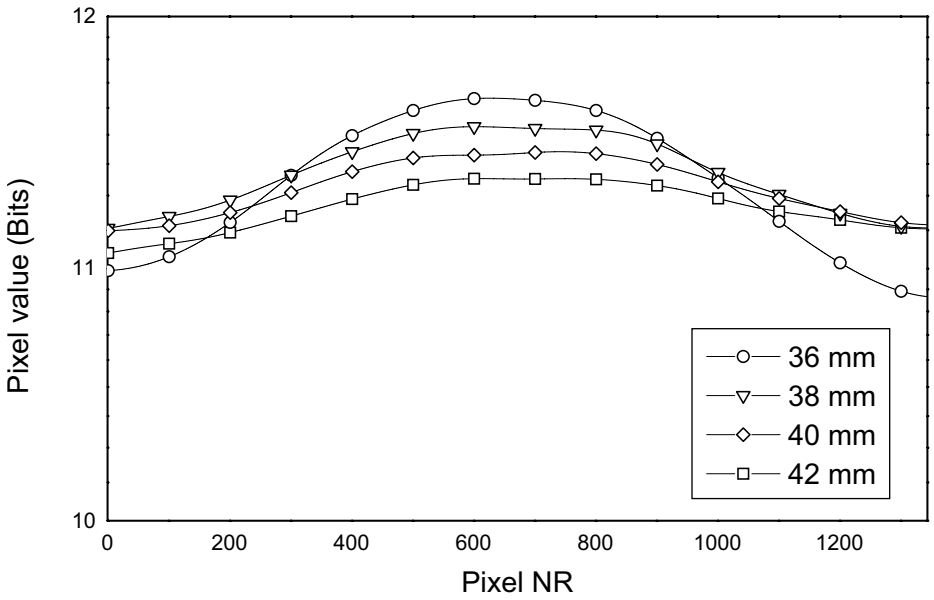

Figure 3.1: The effect on the light distribution over the diagonal of the pixel pitch caused by movement of the LED in z-direction from 36 to 42 mm behind the expander optics (see Fig. 2.3). The substrate is a planar mirror, and the figure shows the pixel value (e.g., brightness, $\log_2$ scale) of pixels over the diagonal of the pixel pitch recorded with a t_p of 5 μs and a 10$\times$ magnification objective.

3.1.2 Plastic lenses

In Sec. 2.2.2, it was mentioned that plastic lenses, specially designed for high power LEDs, could favorably be used in a back-lit system. Figure 3.2 shows a comparison between the Dantec Dynamics Micro-Strobe (used in [22]), and a LED mounted with a plastic lens. Apart from the advantage with having a larger distance between the sample and the light source, the lens approach is more effective in respect to the amount of light that is delivered to the investigation region. During this PhD study, a large amount of plastic lenses, primarily from Carclo Optics and Fraen Srl, have been tested and evaluated. These lenses come in various sizes and coatings, and are designed for different beam-widths and spatial distribution patterns. For micro-PIV measurements in back-lit mode, several of these lenses provide improved illumination, both concerning the illumination intensity and the illumination profile, compared to that of the Micro-Strobe system. The fiber injection types (fiber light injector lens, Fraen Srl and fiber coupling lens, Carclo optics) were found to be the most effective in focusing the light to a small spot, and for scenarios where high intensity illumination is required these are recommended. One the other hand, the 26.5 mm frosted optics (Carclo Optics) provide homogeneous illumination and are easy to align, so if very high intensity or extremely short pulses are not required, one of those lenses could be preferred. As a further note, Fraen Srl recently launched an illumination system (denoted AFTER) for back-lit fluorescent microscopy, which utilizes LEDs and plastic

lenses. The development of such products is promising, not the least for the prospect of future low-cost systems customized for front illumination, where there to date are no plastic lenses on the market that suffice.

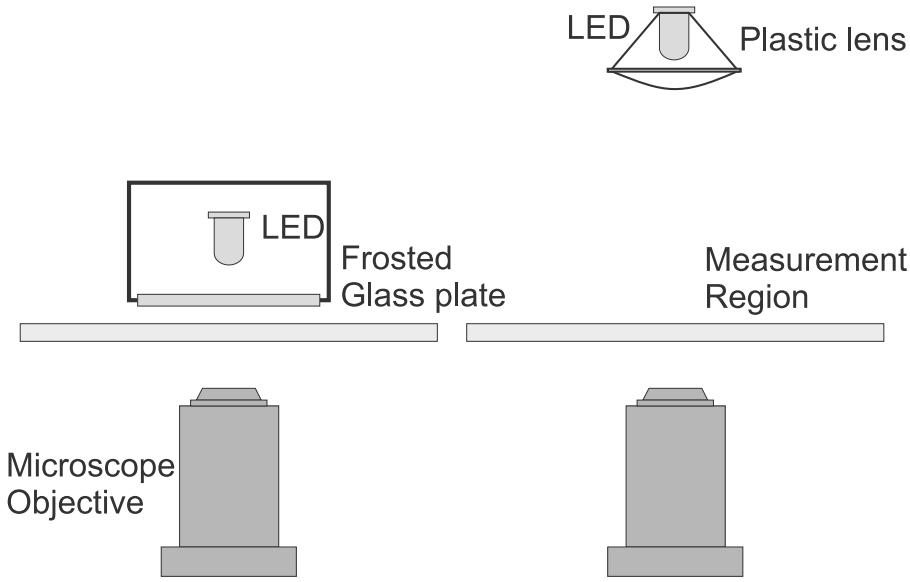

Figure 3.2: (a) The Micro-Strobe back-lit configuration as used in [22]. (b) The improved back-lit configuration with a plastic lens. In (a) the LED needs to be placed in close proximity to the sample, whereas in (b) it can be placed much further away.

3.1.3 LED color

Throughout this study, for several reasons, blue diodes have often been preferred. First of all, the measured light intensity is a combination of the brightness of the light source and the Quantum Efficiency QE of the camera. The Sony ER150 CCD, used in the HiSense MkII, has a peak QE of ∼70% at a wavelength of 500 nm. Of the tested K2 diodes (blue, royal blue, green, cyan and red), the strongest signal was measured for the blue diode. Secondly, for the fluorescent measurements, green fluorescent particles GFP (blue light excitation) were found to appear brighter than red fluorescent particles CY5 (green light excitation). This result is convenient, since it allows switching between recording in scattered and fluorescent mode without requiring a change of the diode. Third of all, a thin measurement depth is often desired, and as the depth of correlation [10] scales directly with the wavelength of the light, a shorter wavelength would thus generally be preferred.

3.1.4 LED products

In this study, one way in which the LED illumination system for micro-PIV was improved, was by simply updating to the latest generation of LEDs. In Table 3.1 the diodes evaluated

in this study are listed, and a picture of the same can be seen in Fig. 3.3. The Micro-Strobe (Dantec Dynamics), which was the only pulsed LED system for micro-PIV prior to this study, utilizes the Luxeon I LED (Lumileds). The Luxeon K2 (Lumileds) and the XLamp (Cree) were found to be similar in performance, of which the slightly brighter K2 was used for the measurements presented in Chap. 2. Thus, by changing from a Luxeon I to a Luxeon K2 (using the diodes' respective listed forward currents for continuous operation) almost three times higher optical output is to be expected (see Table 3.1). From the listed data, the Luxeon V appears to be a good choice, but from experiments it was found that this diode does not provide homogeneous illumination. The reason for this is that the diode is composed of four smaller diode-elements placed with a separation in between, which shows up as a reticule with lower illumination intensity in the center of the illuminated region.

LED type	Forward current (mA)	Typical Luminous Flux (lm)
Luxeon I	350	16
Luxeon III	1000	30
Luxeon V	700	48
Luxeon K2	1500	46
Luxeon Rebel	700	48
XLamp XR-E	350	30.6

Table 3.1: Comparison between forward current and typical luminous flux for different types of blue light emitting diodes used in this study [28, 29].

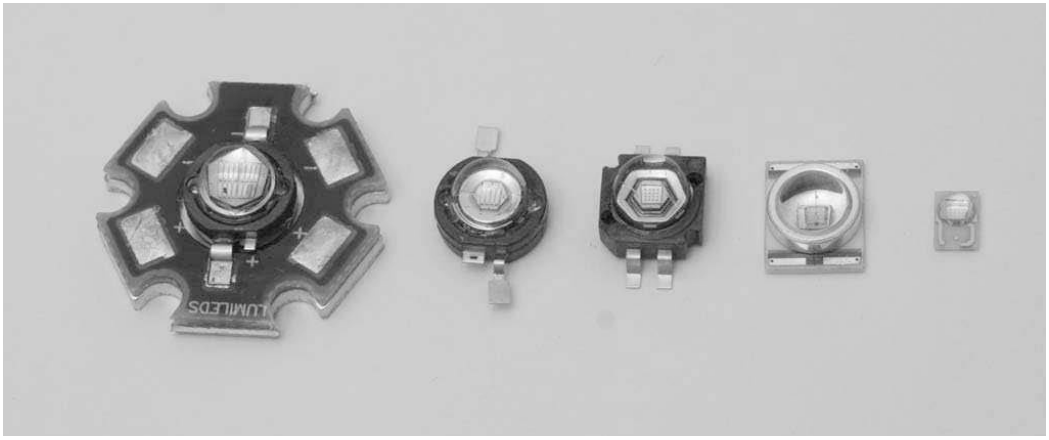

Figure 3.3: Different LED products. From left: Luxeon V Star, Luxeon III Emitter, Luxeon K2, Xlamp XR-E and Luxeon Rebel. The Luxeon I, III and V diodes are available in both Star and Emitter type.

Since the conclusion of the study presented in Chap. 2, new more powerful LEDs have arrived on the market. The one which currently is claimed to be the brightest is the TFFC

K2 (at the moment of writing only available in white), which is an improved version of the K2 utilizing the thin film flip chip technique [28]. As can be seen from Table 3.1, the brightest diode is the Luxeon Rebel, which is especially interesting considering that the Rebel is also substantially smaller than the other diodes. This could have its value for side-lit illumination, or other scenarios where a small sized diode would be beneficial. There is a promising continuous development of new improved products, and the performance of this latest addition of diodes will undoubtedly be surpassed in the next few years.

For micro-PIV applications, the ideal would be to have diodes intended and customized for flash operation. Naturally, it is unlikely that there will be dedicated industrial-scale research on micro-PIV illumination in particular (due to the small size of the market), but neighboring applications (such as flashes for pocket cameras) might provide suitable products. However, it should also be remembered, that the current laser systems are very expensive (several hundreds of thousands DKK), whereas the here presented LED system is of fairly low cost (material and assembly ∼1000–2000 DKK, including power supply and adapter). Thus, there is quite a gap between the two, where there could be a market for more advanced LED products with mid-range performance and mid-range price.

3.1.5 Optimization of LED power

The LEDs that have been used in this study are all designed for continuous lighting solutions. The optical output increases with increasing forward current, as can be seen in Fig. 3.4. This can be utilized in some applications, such as dimmers. For applications that require ambient illumination, with respect to optical output per watt, it is most efficient to use several diodes operating at a lower power. On the other hand, the aspiration for the micro-PIV illumination, in the way that it is applied in this study, is to obtain the maximum optical output from a single diode. Therefore, it is of interest to explore the diodes' performance at very high forward currents.

During operation the LED will, apart from visible light, also produce heat. If the diode is run at a high temperature the forward current will derate, the diode's lifetime be shortened and too high temperature will destroy the diode [28]. The temperature can be controlled by not exceeding the recommended drive current and by, for instance, applying external cooling.

Alternatively, if the LED is set to emit light for very short pulse durations (as in the case of micro-PIV illumination), the diode will heat up much slower than it would from continuous operation. As a consequence, a much higher power can be used, and thus, an increased optical output from the diode achieved (for the duration of the pulse). This was not utilized in Micro-Strobe, for which a forward current of 314 mA was measured over the diode.

In Fig. 3.5 the normalized light intensity versus estimated forward current for the three generations of power supplies used in this study are shown. The power supplies were built by Danchip's electronics workshop (see Appendix A for a sketch of the design). Each box was equipped with a switch for changing between two different power modes, and they were all designed to match the resistance of a K2 diode, which was used for the measurements presented in Fig. 3.5. In this comparison, it was found that the light intensity (recorded

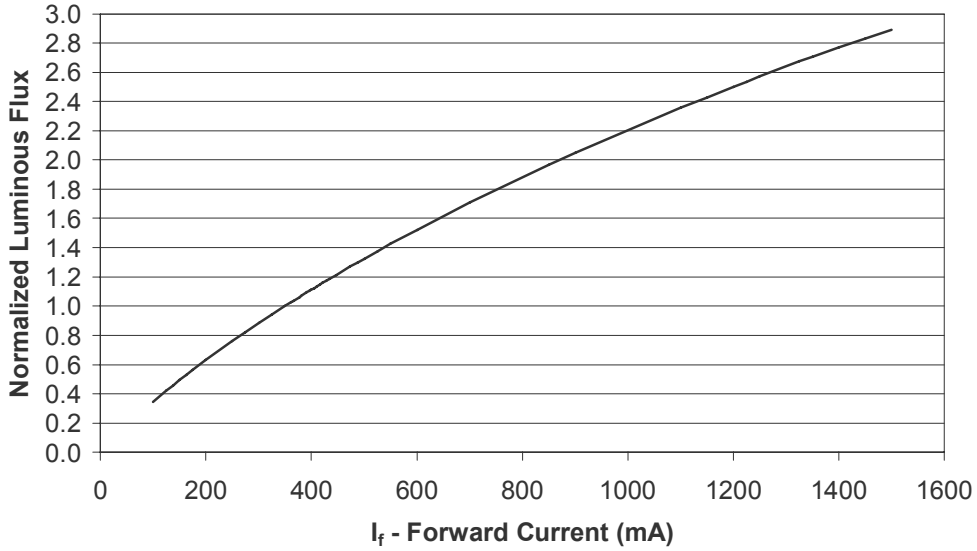

Figure 3.4: Relative luminous flux versus forward current for Lumileds Luxeon K2 diodes. Junction Temperature, TJ = 25°C [28].

by a spectrometer) was more than three times larger for the last power supply, designed to achieve a forward current of 6.6 A, than the first power supply with a forward current of 800 mA. As expected from Fig. 3.4, the gain in optical output (from increasing the forward current) tapers off with higher forward currents. For instance, between 4.0 A and 6.6 A a fairly small increase is seen. However, the distribution of the measurement points in Fig. 3.5 indicates that the actual forward currents provided by the power supplies were different from the estimated values, which were used in the figure. A similar deviation was seen for supplementary average gray-value measurements using the HiSense MkII camera, which strengthens this suspicion.

If the forward current is to be measured, at very high powers, it needs to be done with the diode operating in pulsed mode. This is non-trivial, and requires special equipment which was not available at the department's labs. Therefore, a further investigation of this subject has not been attempted in the course of this study. At the moment of writing, there is no reference data available from the LED manufacturers for forward currents in this regime. The author is neither familiar with any other study where measurements of the optical output for high forward currents using these diodes have been attempted. A final comment should be made that concerning micro-PIV, it is more direct, and can thus be preferable, to measure the achieved contrast for a specific setting (as in Sec. 2.2.4), rather than the intensity of the illumination.

3.1.6 LED pulse lengths

A test was performed to investigate how the illumination scales with decreasing pulse lengths. The rise time of the diodes are in the range of 100 ns, so short, and well defined

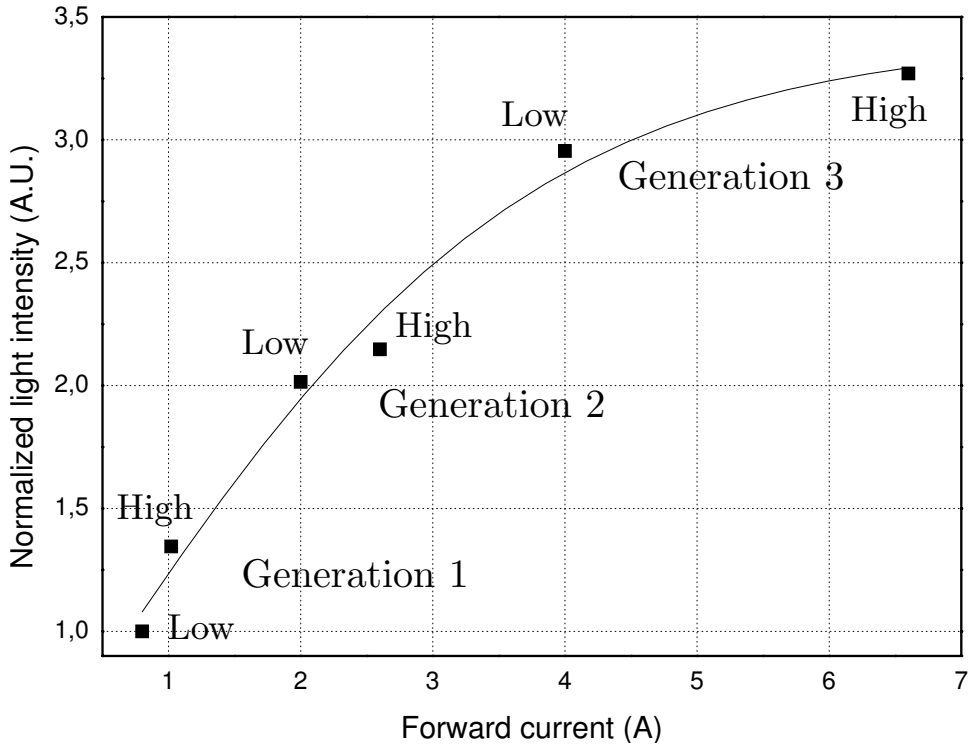

Figure 3.5: Normalized light intensity versus estimated forward current. A green Luxeon K2 diode was used, with an illumination pulse duration of 5 μs.

pulses are feasible [27, 28]. Of course, at the present time these pulse lengths are primarily of interest for micro-PIV recordings in scattered mode, since fluorescent mode requires substantially longer pulses. In Fig. 3.6 the optical output, measured with a spectrometer, for different pulse lengths is shown. The measurements were made in two sets, from 0.25−5 μs (set 1, five pulses) and from 5−20 μs (set 2, single pulse). The background was subtracted, and a linear fit was calculated from set 2. In addition, the spectral output from the measurement of set 1 is displayed in Fig. 3.7. The results confirm that short well defined pulses are feasible, and that the optical output scales linearly with the pulse length. Naturally, for very short pulses (below 1 μs) the rise time becomes increasingly important. However, a full investigation of pulse lengths in this regime falls beyond the scope of this study.

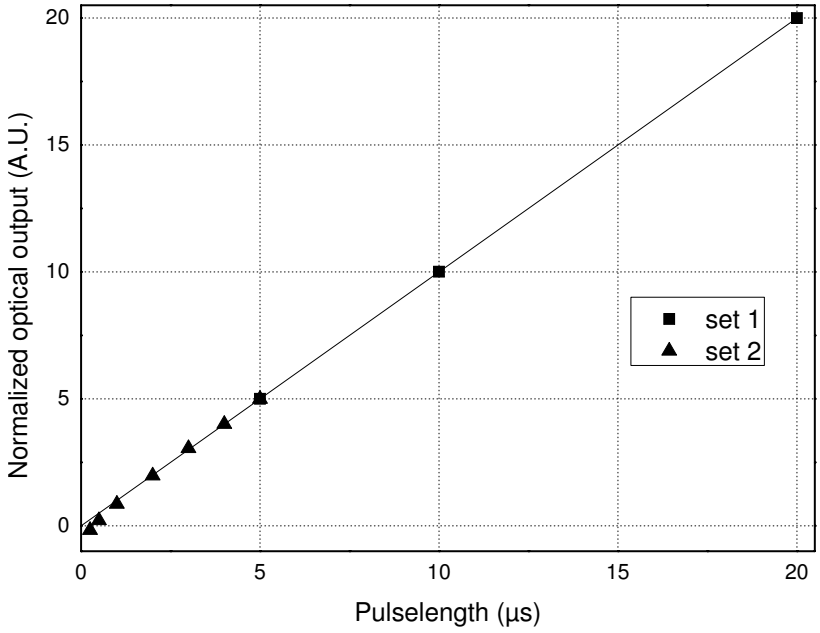

Figure 3.6: Normalized optical output versus pulse length. The fit is made from set 2 (with longer pulse lengths), with k=1. The measured optical output is linear down to a pulse length of 1 μs.

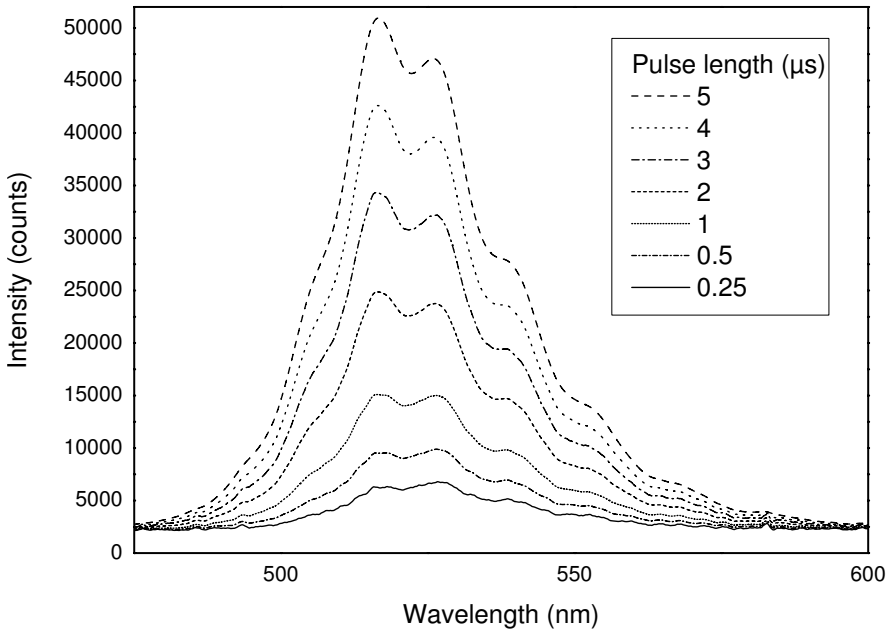

Figure 3.7: Spectral output for measurements with different pulse lengths.

3.2 Fluorescent versus scattered mode

Since the first publication on micro-PIV by Santiago *et al.* [8] in 1998, recording in fluorescent mode has been the totally dominating method in micro-PIV. In the mentioned work, continuous illumination from a Hg-arc lamp was utilized, and already in the following year micro-PIV with a double pulsed laser was demonstrated by Meinhart *et al.* [30]. In terms of capacity, the double pulsed laser system has not yet been surpassed, which is likely a contributing factor as to why alternative illumination sources and recording modes for "standard" micro-PIV has have not enjoyed more attention so far.

In Chap. 2, a first comparison between micro-PIV recordings in fluorescent and scattered mode was provided. Such a direct comparison has, to the author's knowledge, not been demonstrated previously. The study showed that both recording methods are feasible, and that they provide coinciding results. However, although a dark particle on a bright background and a bright particle on a dark background are analogous from a mathematical perspective, there are several differences between the two recording modes, not the least from an experimental, or practical, point of view. This subject deserves a much deeper examination than what has been reached within the current study. Primarily, a more thorough investigation of the possibilities and limitations of measurements in scattered mode would be desirable. This section, in which the author's thoughts and findings on this topic are summarized, is intended to inspire and provide a starting point for such further studies.

3.2.1 Illumination pulse length required

In order to obtain the same contrast, a shorter illumination pulse length is generally required when recording in scattered mode compared to recording in fluorescent mode (see Fig. 2.6). Notably, the amount of light required is increasing with higher magnification in scattered mode, whereas the opposite is true in fluorescent mode. However, additional measurements using a larger set of (fluorescent) particles of different sizes, are required in order to provide a more precise description.

3.2.2 Background glow

One feature of fluorescent microscopy is that emitted light from out-of-focus particles will raise the background light level, thus lowering the contrast between the bright in-focus particles and the background. This effect is often denoted as background glow. In micro-PIV, this is a limitation especially when recording with high magnification (and in deep channels), where a large number of particles per volume are required. From the author's experience, the effect is similar when recording in scattered mode. Instead of a background glow, the out-of-focus particles lower the background light level, which could be described as a "background shade". A comparison between particle images recorded in the two modes is shown in Fig. 3.8. The effect of more particles (decreasing the contrast) is similar, but it has not been investigated if the background glow and the background shade scale differently with magnification. Naturally, such a comparison would also need to

take different substrate materials into account. Additionally, apart from an experimental investigation, it would be desirable if this topic was approached analytically.

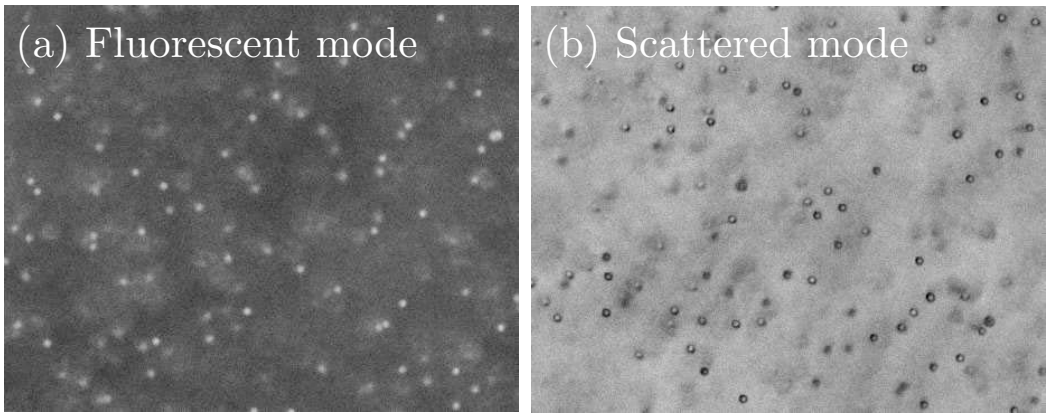

Figure 3.8: Images of particles in a micro-structure recorded with a 63× magnification objective (mounted with a 0.63× tv-adapter) in (a) fluorescent mode and (b) scattered mode. The out-of-focus particles give rise to a background glow in (a) and to a "background shade" in (b), in both cases diminishing the contrast between the particles in focus and the background. The micro-structure was fabricated in a silicon substrate and the images were recorded at a depth of 45 μm.

3.2.3 Light scattering and image quantization

In Fig. 3.9, a comparison between images of a 1 μm particle recorded in (a) scattered mode and (b) fluorescent mode recorded with a 63× magnification objective are shown. While the particle recorded in fluorescent mode appears as a bright spot with respect to the background, the particle recorded in scattered mode appears as a bright spot surrounded by a dark ring (in turn surrounded by a bright ring). This appearance is not intuitive to how we experience objects in the macroscopic world, but it is perfectly in line with what is expected from Mie's scattering theory for small particles [31]. This theory, which describes how light is scattered by a small particle (with a diameter larger than the wavelength of the light), tells us that the light is not simply blocked by the particle, but is scattered in all directions (although not uniformly). For a 1 μm particle in water, this pattern is dominated by a very strong forward scatter (along the direction of the incident light), which is what shows up as the central bright spot in the image. Additionally, these particle images are not related to the diffraction patterns originating from defocusing, although they could be mistaken for such. Image recordings of particles at different depths, such as in Fig. 3.8, rule out this possibility, since in that case similar patterns would be expected in both (a) and (b). However, there will still be diffraction patterns when recording in scattered mode, but those ring patterns will then be overlayed in addition to the ring patterns originating from Mie scattering.

One interesting feature of illumination in scattered mode comes as a consequence of that the cross-correlation is performed on the full image profile of the particle. This

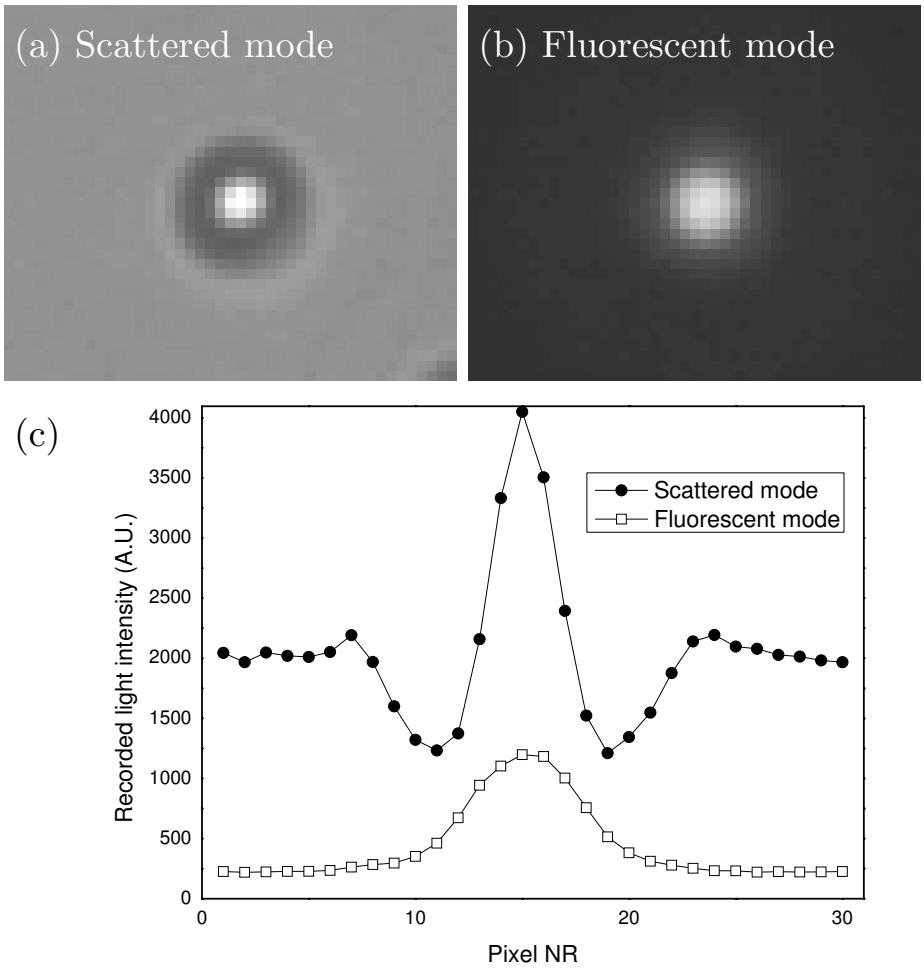

Figure 3.9: Recordings of a 1 μm particle with a 63× magnification objective (0.63× tv-adapter) in (a) scattered mode, back-lit (50 μs pulse) and (b) fluorescent mode, front-lit (2 ms pulse). (c) The respective gray-values on the pixel pitch for a line drawn over the center of the particle.

means that both the dark and the bright parts of the particle image, with respect to the background (see Fig. 3.9), contribute to the correlation. In practice, this corresponds to a very high bit-resolution. However, the forward scatter peak is not always detectable, especially so with lower magnification objectives. This is the reason why (if we once again examine the recordings in scattered mode in Fig. 2.6) the highest image quantization is achieved with the 63× magnification objective, although a longer illumination pulse length compared with a lower magnification objective is also required. The reason why the forward scatter peak is not visible when recording with lower magnification has not been fully investigated, but at least the following two points are of importance. First of all, with a very low magnification, both the dark and the bright parts of the particle image will be recorded in the same pixels, and therefore, the forward scatter peak will not be

distinguishable. Secondly, the light intensity of the background recorded by the camera will be lower when a higher magnification is used. The forward scatter for a specific particle will, on the other hand, be the same. Thus, the forward scatter signal will be relatively brighter in relation to the background when using a microscope objective with higher magnification.

3.2.4 Substrate materials and near wall effects

One important difference between recording in fluorescent and scattered mode is the impact of the substrate material. In scattered mode there are features that will appear dark when the sample is illuminated, for example structures such as steps, grooves or bumps. Shading effects are also often seen near walls, and rough surfaces can provide speckled backgrounds consisting of both dark and bright regions. Two examples are seen in Fig. 3.10. This kind of features can lower the contrast between the particles and the background, and even prohibit velocity vectors to be obtained from certain regions.

There is no simple answer to what influence this will have to the measurements, as this depends on several factors, such as the function and physical properties of the sample and the tracers, the magnification (measurement depth) and the ambition of the investigations. The influence on the measurements can sometimes also be decreased by an analytical approach, such as background subtraction or (local) averaging. In contrast, in fluorescent mode such features will not be recorded by the camera, since the excitation light is removed by a filter, and the only fluorescent objects are the tracers. Thus, with respect to this topic, though it in many cases even is possible to work in scattered mode if proper data treatment is applied, it is clearly more convenient and simpler to work in fluorescent mode.

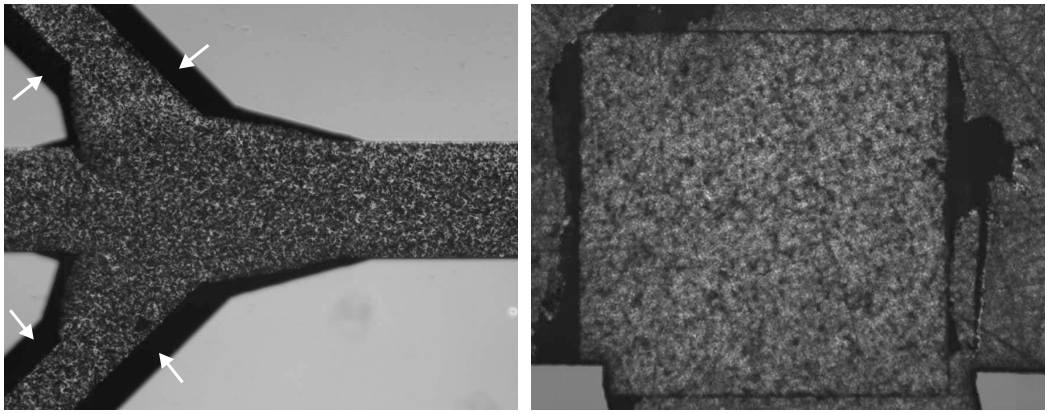

Figure 3.10: Left panel: Recording of a microdevice fabricated in silicon substrate filled with 5 μm tracer particles. The slanted walls (indicated by the white arrows) from the anisotropic wet etching appear black on the image frame, and no velocity vectors can be obtained from this region when recording in scattered mode. Right panel: Image of a piezo-element inside a microchannel (clear fluid, no particles added). The rough reflecting surface of the piezo-element has a speckled appearance under illumination, which makes recording in scattered mode problematic.

3.2.5 Scattered mode – special applications

Generally, for fluidic scenarios, recording in fluorescent mode is equal, or superior, to recording in scattered mode with respect to limitations and performance. For LED illumination in particular, due to the lower energy compared with a laser system, scattered mode can be preferred in some situations, such as for measurement of very high velocity flows. However, for lab-on-a-chip applications it is often of interest to investigate the flow behavior of particles with certain properties, or with a specific response to external forces. Relevant forces are, for instance, magnetic, acoustic, electric or gravitational forces, and examples of bodies could be magnetic particles, metallic particles, micelles, cells or other cellular components. Such natural tracers, are not always available in, or modifiable into, fluorescent versions. Therefore, for such scenarios recording in scattered mode can be a viable alternative. Apart from lab-on-a-chip systems, another type of applications where recording in scattered mode can be utilized is for *in vivo* investigations, such as measurements of the flow in blood vessels using natural bodies (red blood cells) as tracers [32].

Chapter 4

Investigations of acoustic phenomena using micro-PIV

4.1 Introduction

A large portion of this project has been focused on applying micro-PIV for the investigation of acoustic phenomena in microfluidic devices. The paper [16], presented in Sec. 4.3, describes the investigation scheme that was developed. In Appendix B supplementary measurements from the test chambers that were used in this study are provided, and the fabrication procedure that was used to manufacture the devices is included in Appendix C. Additional results and findings from measurements on other acoustic devices are presented in Chap. 5. In the following Sec. 4.2, the governing equations of acoustic forces on particles and acoustic streaming phenomena are provided.

4.2 Acoustofluidic theory and simulations

For the analytical treatment of the acoustofluidic phenomena, the Navier-Stokes equation for a Newtonian, compressible and viscous fluid [33],

$$\rho[\partial_t \mathbf{v} + (\mathbf{v} \cdot \nabla)\mathbf{v}] = -\nabla p + \eta \nabla^2 \mathbf{v} + \beta \eta \nabla(\nabla \cdot \mathbf{v}) \tag{4.1}$$

and the continuity equation (for the conservation of mass),

$$\partial_t \rho = -\nabla \cdot (\rho \mathbf{v}) \tag{4.2}$$

are used. Here, $\mathbf{v}$ is the particle velocity, p is the pressure, and β is a constant. ρ and η are the bulk density and viscosity, respectively. A perturbation approach is applied, namely,

$$p = p_0 + p_1 + p_2 + ... \tag{4.3a}$$
$$\rho = \rho_0 + \rho_1 + \rho_2 + ... \tag{4.3b}$$
$$\mathbf{v} = \mathbf{0} + \mathbf{v}_1 + \mathbf{v}_2 + ... \tag{4.3c}$$

for which we assume that $p_1 \ll p_0$ and $p_2 \ll p_1$. Remember that $p_1 = c^2\rho_1$, where c is the speed of sound. If we apply time-averaging, all of the first-order terms will become zero. Remaining are the pure second-order terms and the products of the first-order terms (the first-order fields act as sources for the second-order fields). The result is the following time-averaged Navier-Stokes equation:

$$\nabla\langle p_2\rangle = -\langle\mathbf{F}\rangle + \eta\nabla^2\langle\mathbf{v}_2\rangle + \beta\eta\langle\nabla(\nabla\cdot\mathbf{v}_2)\rangle \tag{4.4}$$

where the force field $\langle\mathbf{F}\rangle$ is given by

$$\langle\mathbf{F}\rangle \equiv \rho_0\langle\mathbf{v}_1(\nabla\cdot\mathbf{v}_1)\rangle + \rho_0\langle(\mathbf{v}_1\cdot\nabla)\mathbf{v}_1\rangle. \tag{4.5}$$

The full derivation of these equations can be found elsewhere [33, 34]. More details on how the simulations used in [16] and [17] were performed can be found in [35].

4.3 S. M. Hagsäter *et al.*, Lab Chip, 2007, 7, 1336–1344

beginning of paper

Acoustic resonances in microfluidic chips: full-image micro-PIV experiments and numerical simulations

S. M. Hagsäter, T. Glasdam Jensen, H. Bruus, and J. P. Kutter
MIC – Department of Micro- and Nanotechnology, DTU Bldg. 345 east, Technical University of Denmark, DK-2800 Kgs. Lyngby, Denmark

We show that full-image micro-PIV analysis in combination with images of transient particle motion is a powerful tool for experimental studies of acoustic radiation forces and acoustic streaming in microfluidic chambers under piezo-actuation in the MHz range. The measured steady-state motion of both large 5 μm and small 1 μm particles can be understood in terms of the acoustic eigenmodes or standing ultra-sound waves in the given experimental microsystems. This interpretation is supported by numerical solutions of the corresponding acoustic wave equation.

4.3.1 Introduction

For the typical dimensions of microfluidic structures there are two acoustic effects of main importance: *the acoustic radiation force* [36, 37, 38], which moves suspended particles either towards or away from pressure nodes depending on their acoustic material properties, and *acoustic streaming* [39, 40], which imparts movement onto the entire solvent. Both of these forces have been utilized, alone or in combination, for several lab-on-a-chip applications. Yasuda *et al.* [41, 42], demonstrated concentration of particles by acoustic radiation forces, and separation of particles by acoustic forces in combination with electrostatic forces. One of the most attractive applications for acoustics in microfluidics is for mixing [43, 44, 45], as this process typically is diffusion limited in microscale devices. Valveless ultrasonic pumps, utilizing acoustic streaming, have also been presented [46, 47]. Numerous examples of microsystems where acoustics are applied to handling and analysis of biological material have been suggested. Among others these include: trapping of microorganisms [48], bioassays [49], and separation and cleaning of blood [50, 51, 52]. Apart from on chip devices, acoustic forces have also been suggested for use in other μm-scale applications [53].

There are different imaging strategies and tools, which can be used in order to enhance the understanding, and to visualize the function of acoustic micro-devices during operation. For acoustic mixers the effect can be illustrated and measured by partly filling the mixing chamber with a dye prior to piezo-actuation [44, 45]. However, this approach is mainly limited to determine the total, and not the local, mixing behavior within the chamber. A more refined method, which is not limited to the study of micromixers, is to apply streak- or streamline analysis. This was shown by Lutz *et al.* [54, 55], who neatly demonstrated 3D steady micro streaming around a cylinder. Although streamline analysis can be employed to illustrate flow behavior, it is not suitable in determining local variations in velocity. For that purpose, the micron-resolution particle image velocimetry (micro-PIV) technique is the method of choice [8]. With this technique the motion of tracer particles, acquired from consecutive image frames, is utilized to obtain velocity vector fields. In a large chamber, local measurements of particle motion induced by acoustic radiation forces and acoustic streaming have been performed by Spengler *et al.* [56, 57], and further developed by Kuznetsova *et al.* [58]. Li and Kenny derived velocity profiles in a particle separating device utilizing the acoustic radiation force [52]. Jang *et al.* used confocal scanning microscopy to perform micro-PIV measurements on circulatory flows in a piezo-actuated fluidic chamber [59]. Furthermore, Manasseh *et al.* applied micro-PIV to measure streaming velocities around a bubble trapped in a microfluidic chamber [60].

As particles under the influence of acoustic fields do no longer function as true independent tracers in all situations, and as several acoustic effects come into play at the same time, extra caution and consideration have to be taken when applying micro-PIV for microfluidic acoustic studies. These considerations will be discussed in more detail in Sec. 4.3.2. The situation is further complicated by the coupling from the actuator to the structures and their acoustic resonances, which is a yet poorly understood mechanism. The resonances depend on the acoustic material parameters as well as the geometry of both the chip and the chamber. For substrate materials with low attenuation, such as

silicon, the actuation will result in strong resonances over the whole devices, whereas for substrate materials with high attenuation, the effect will be mostly confined to the proximity of the actuator. Moreover, in a real system the coupling strengths vary for different resonances, and amplitude fluctuations across the structures are often observed. Therefore, if investigations striving to yield a better understanding of acoustic resonances in low attenuation microfluidic chips are to be performed, it is not sufficient only to study the acoustic phenomena locally.

In this work, full-image micro-PIV analysis in combination with images of transient particle motion is suggested as a tool for studying acoustic resonances in microfluidic chambers under piezo-actuation. The acousto-fluidic phenomena mentioned above can be investigated by comparing these experimental images with plots of acoustic eigenmodes of the device structure obtained by numerical solution of the corresponding acoustic wave equation.

4.3.2 Materials and experimental methods

Microchip fabrication

In this study, two microfluidic chambers were investigated, one of quadratic footprint with a side-length of 2 mm and one of circular shape with a diameter of 2 mm. The size was chosen to be a few times the acoustic wavelength of 2 MHz ultrasound waves in water, and the specific shapes were employed to ensure simple patterns in the pressure field at the acoustic resonances. Both chambers were connected to 400 μm wide inlet and outlet channels, and the depth was 200 μm throughout. The microfluidic chips were fabricated in silicon via deep reactive ion etching (DRIE). The same technique was also applied on the backside of the chip to etch 300 μm diameter round fluidic inlets. Anodic bonding was used to seal the structures with a 500 μm thick pyrex glass lid on the channel side. Silicon rubber tubings were glued to the holes on the backside of the chip, for easy attachment of teflon tubing. A picture of one of our microfluidic chips is shown in Fig. 4.1, and a list of the geometrical parameters is given in Table 4.1.

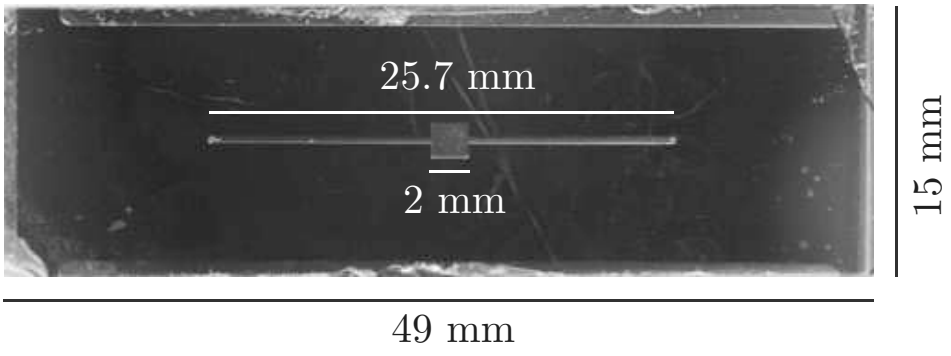

Figure 4.1: A top-view photograph of the silicon-glass chip (dark gray) containing a square chamber with straight inlet and outlet channels (light gray).

Experimental setup and procedure

The piezo-actuator (Pz27, Ferroperm) was pressed to the backside of the chip using an ultrasonic gel (ECO, Ceracarta) and biased by a 20 V ac tone generator (Model 195, Wavetek). Images were captured with a progressive scan interline CCD camera (Hisense MkII, Dantec Dynamics), mounted with a 0.63× TV-adapter on an epifluorescent microscope (DMLB, Leica). The objective used was a Plan 5× with a numerical aperture NA of 0.12. For the given fluidic geometries, this combination allowed capture of full-image PIV vector fields, while utilizing the largest number of pixels on the CCD. A blue light emitting diode, LED, (Luxeon Star 3W, Lumileds) was used as illumination source in a front-lit configuration, which is described elsewhere [15]. The LED was powered by an in-house built power supply controlled by a PIV timing system (Dantec Dynamics). Image acquisition was performed on a PC with Flowmanager software (Dantec Dynamics). As tracer fluids solutions of 1 μm polystyrene micro-beads (Duke Scientific), 5 μm polyamide micro-beads (Danish Phantom Design), diluted milk, and fluorescein have been used.

The investigations were performed by scanning the applied frequency from the tone generator and identifying those frequencies which led to a strong response, an acoustic resonance, in the microfluidic chamber. At the resonance frequencies, the behavior of the different tracer particle solutions was observed. Between successive recordings the chip was flushed to assure homogeneous seeding. Furthermore, to make sure that only particle motion caused by acoustic forces were recorded, no external flow was applied during measurements.

Micro-PIV considerations

In micro-PIV tracer particles are chosen for their ability to truthfully follow the motion of the flow that is to be investigated. Particles under the influence of an acoustic field do no longer fulfil this criterium in all situations. Therefore, extra caution and considerations have to be taken regarding what movements are actually measured when applying micro-PIV for these types of studies. Given that particle motion caused by thermal or gravitational forces can be neglected, the main task is to determine if particle motion is caused by acoustic radiation forces, acoustic streaming or a combination of the two. In this study, this problem was tackled by applying three tracer solutions with different physical properties.

chip length	L_0	49 mm	silicon thickness	h_s	500 μm
chip width	w_0	15 mm	pyrex thickness	h_p	500 μm
channel length	L_c	26 mm	chamber height	h	200 μm
channel width	w_c	400 μm	chamber width	w	2 mm

Table 4.1: The geometrical parameters of the fabricated microfluidic silicon-pyrex chip.

Typically, the large polyamide particles are more strongly affected by the acoustic radiation forces than by the forces due to acoustic streaming of the surrounding water.

In contrast, since the acoustic radiation force scales with the volume of the particle, the small polystyrene particles will follow the motion of the water, if relatively strong acoustic streaming is present. However, there is no simple relation between the two forces, and for an arbitrary frequency and geometry one can be strong whereas the other is not, and vice versa. Therefore, in order to determine whether particle motion is caused by acoustic radiation forces or acoustic streaming it is necessary to utilize the dependance of the acoustic radiation forces on the compressibility of the particle.

The polymer particles will move towards the pressure nodes since their compressibility is smaller than that of water. The opposite is true for the lipid particles in milk: their compressibility is larger than that of water, and consequently they will move towards pressure antinodes. Like the small polystyrene particles, the lipid particles we used were small enough to typically follow the net acoustic streaming flow of the water. Thus, if similar motion is recorded with two types of tracers with different compressibilities compared to the medium, the acoustic radiation forces can be ruled out as cause of the motion. As an alternative or complementary technique to micro-PIV measurements, fluorescein can be used to investigate acoustic streaming. A summary of the acoustic behavior of the different particles used in this study, and some other bodies that are common in microfluidic applications, is given in Table 4.2.

The speed of sound c in water has a significant dependence on temperature T given by the large derivative $\partial c/\partial T \simeq 4\ \mathrm{m\,s^{-1}K^{-1}}$. All tracer fluids were therefore kept at room temperature, so that the temperature was not changed when the microchip was flushed during tracer particle exchange. The microchips used in this study are comparable in size and mode of actuation to those used for ultrasonic agitation in a study by Bengtsson and Laurell [61]. They performed sensitive temperature measurements on the reactor outlet, where no temperature increase caused by the acoustic power could be detected. In our study, the piezo-actuator was run at a moderate power-level and only for the short intervals during recordings (typically less than one second). Therefore, it can be ruled out that heating from the piezo-actuator would have any measurable impact on the measurements.

tracer type	force	direction
beads (1 μm)	weak	nodes
beads (5 μm)	strong	nodes
red blood cells	strong	nodes
milk particles	weak	anti-nodes
large micelles	strong	anti-nodes
fluorescein	none	-

Table 4.2: The susceptibility to acoustic radiation forces for the particles used in this study, as well as for some other particles common to microfluidic applications.

One important factor, which needs to be accounted for when applying micro-PIV on systems affected by acoustic forces, is that the local seeding density will be distorted during actuation. This is normally not a problem when measuring on particle motion caused solely

by acoustic streaming, as this motion generally will be of a circulating nature. On the other hand, in the case of particle motion induced by acoustic radiation forces, it will typically lead to total expulsion of particles from certain regions into others. If PIV-vector statistics is applied, only the first few image-pairs recorded after piezo-actuation has been initiated can be used, and in this study, images from a number of consecutively recorded sets have been used for averaging. Moreover, in the case of scanning, or mapping, techniques the expulsion of particles is especially problematic, as the seeding conditions in the device, or chamber, need to be restored for each measurement position. Also, the conditions may change during these lengthy recordings, leading to results that are difficult to interpret.

The acoustic resonances in low attenuation piezo-actuated microfluidic devices are formed over the whole devices, and they are also depending on the geometry of the whole device. As a consequence, there will typically be amplitude fluctuations over the devices, due to unwanted artifacts, or deliberate designs. Therefore, when investigating acoustic resonances, and the influence caused by different modifications to the sample, it is important to study the effects globally. If the acoustic effects are only measured in a part of the device, this kind of information will not be yielded, independently on how detailed the flow is mapped within that region. Therefore, we suggest full-image micro-PIV for the investigation of acoustic resonances in microfluidic devices.

In this study, emphasis has been put on how to present the measured data in such a way that still images and PIV-vector plots give the best illustration of the transient particle motion caused by the acoustic forces. To achieve this, we have chosen to superimpose the PIV-vector plots of the initial transient velocities on top of the pictures of the steady-state patterns of the particles obtained after a few seconds of actuation. After longer actuation times, secondary patterns will form, so images taken at this point can give a false impression of the particle motion. This method of combining the transient PIV-vector plots and steady-state pictures has proven useful when comparing numerical simulations with micro-PIV measurements, especially for measuring amplitude fluctuations across the structures, and when discriminating between different numerical models. This will be demonstrated in Sec. 4.3.4.

4.3.3 Numerical simulations

In the experiments, the acoustic pressure field, which is superimposed on the ambient constant pressure, is driven by a harmonically oscillating piezo-actuator, i.e., the time-dependence can be described as $\cos(\omega t)$. In this work, we focus on the acoustic resonances where the response of the bead solution is particularly strong. As the attenuation of the acoustic waves is relatively small, we can approximate the actual frequency-broadened acoustic resonances of the driven system by the infinitely sharp eigenmodes of the isolated dissipationless chip.

The pressure eigenmodes $p_n(x, y, z)\cos(\omega_n t)$, labelled by an integer index n, and the angular eigenfrequencies or resonance frequencies ω_n are found as solutions to the Helmholtz eigenvalue equation $\nabla^2 p_n = -(\omega_n^2/c_i^2)\, p_n$, where the index i is referring to the three material domains of silicon, water and glass in the chip. The boundary conditions at the outer edges of the system are given by the soft-wall condition $p_n = 0$ except at the bottom plane,

where a hard-wall condition $\mathbf{n} \cdot \boldsymbol{\nabla} p_n = 0$ is chosen to mimic the piezo-actuator which fixes the velocity of the wall. At the internal interfaces between the different material regions the boundary conditions are continuity of the pressure p_n as well as of the wall-velocity. The latter is ensured by continuity of the field $(1/\rho_i)\boldsymbol{\nabla} p_n$. A list of the acoustic material parameters, i.e., sound velocities c_i and densities ρ_i, is given in Table 4.3.

material	speed of sound	density
water	$c_w = 1483$ m/s	$\rho_w =$ 998 kg/m^3
silicon	$c_s = 8490$ m/s	$\rho_s =$ 2331 kg/m^3
pyrex	$c_p = 5640$ m/s	$\rho_p =$ 2230 kg/m^3

Table 4.3: The acoustic material parameters of the microsystem at 20 °C: sound velocities c_i and densities ρ_i from the CRC Handbook of Chemistry and Physics.

The Helmholtz equation was solved numerically using the COMSOL finite element method software. However, the large aspect ratio of the flat device made it impossible to simulate the actual device in 3D due to limited computer memory. We therefore investigated the possibility of making 2D simulations. The rationale for doing this is that the total height of the chip is only 1 mm. Given a weighted average speed of sound in the silicon-glass chip of 6900 m/s, the wavelength of a wave at the highest used frequency $f = 2.5$ MHz is 3 mm and thus three times the chip height. Similarly, at the same frequency the wavelength in water is 0.6 mm or three times the chamber height. Consequently, there is not room enough for even half a standing wave in the vertical direction neither in the water filled chamber nor in the silicon-glass chip.

The first step towards a more rigorous justification for doing 2D simulations was to make a smaller 3D version of the system geometry. While keeping all the correct height measures as well as the chamber width as listed in Table 4.1, we shrunk the planar dimensions of the surrounding chip to $L_0 = 8$ mm, $w_0 = 6$ mm and $L_c = 6.8$ mm. With this reduced geometry we could carry out the full 3D simulations, and the results thereof confirmed that the variations in the vertical z-direction of the 3D eigenmodes were modest, see the xz-plane plots of Figs. 4.2(a) and (b). A 2D simulation was then carried out for the horizontal xy center-plane of the chamber, i.e., a 2D water-filled area surrounded by a 2D silicon region. Comparing the 50 lowest 3D and 2D eigenmodes gave the following results: (1) in the horizontal xy center-plane of the chamber the 3D eigenmodes agreed with the 2D eigenmodes, see Figs. 4.2(c–f); (2) due to the lack of the z-dependence in the Laplacian of the 2D Helmholtz equation, the 2D eigenfrequencies were systematically smaller than the 3D eigenfrequencies, see Fig. 4.2(g). It has thus been justified to simulate the experimentally observed resonances by 2D eigenmodes in the horizontal xy center-plane of the chamber. This we denote the *2D chip model*.

Due to the small acoustic impedance ratio $(\rho_w c_w)/(\rho_s c_s) = 0.08$ between silicon and water, the simulations could be simplified even further. As demonstrated in Figs. 4.3(c) and (d), it suffices to find the eigenmodes of the chamber itself using hard-wall boundary conditions along its edges, except at the very ends of the inlet channels where soft-wall boundary conditions are employed to mimic in- and outlets. This we will refer to as the

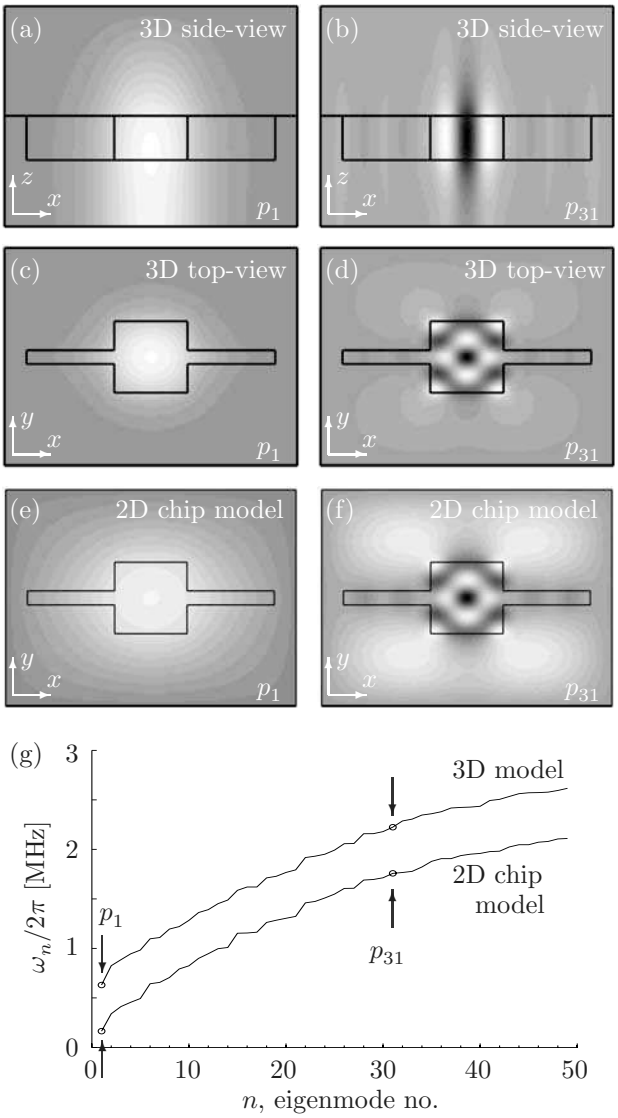

Figure 4.2: Numerical simulations of the pressure eigenmodes $p_n(x, y, z)$ shown in gray-scale plots. (a) and (b) 3D model: side-view (xz-plane) of p_1 and p_{31}, respectively. (c) and (d) 3D model: top-view (xy-plane) of p_1 and p_{31}, respectively. (e) and (f) 2D chip model: top-view (xy-plane) of p_1 and p_{31}, respectively. (g) The eigenfrequencies $\omega_n/2\pi$ versus mode number n for the 3D model and the 2D chip model.

2D chamber model.

4.3.4 Results and discussion

We have measured the flow response to the acoustic actuation in the frequency range from 0.5 to 2.5 MHz paying special attention to the strong responses corresponding to acoustic

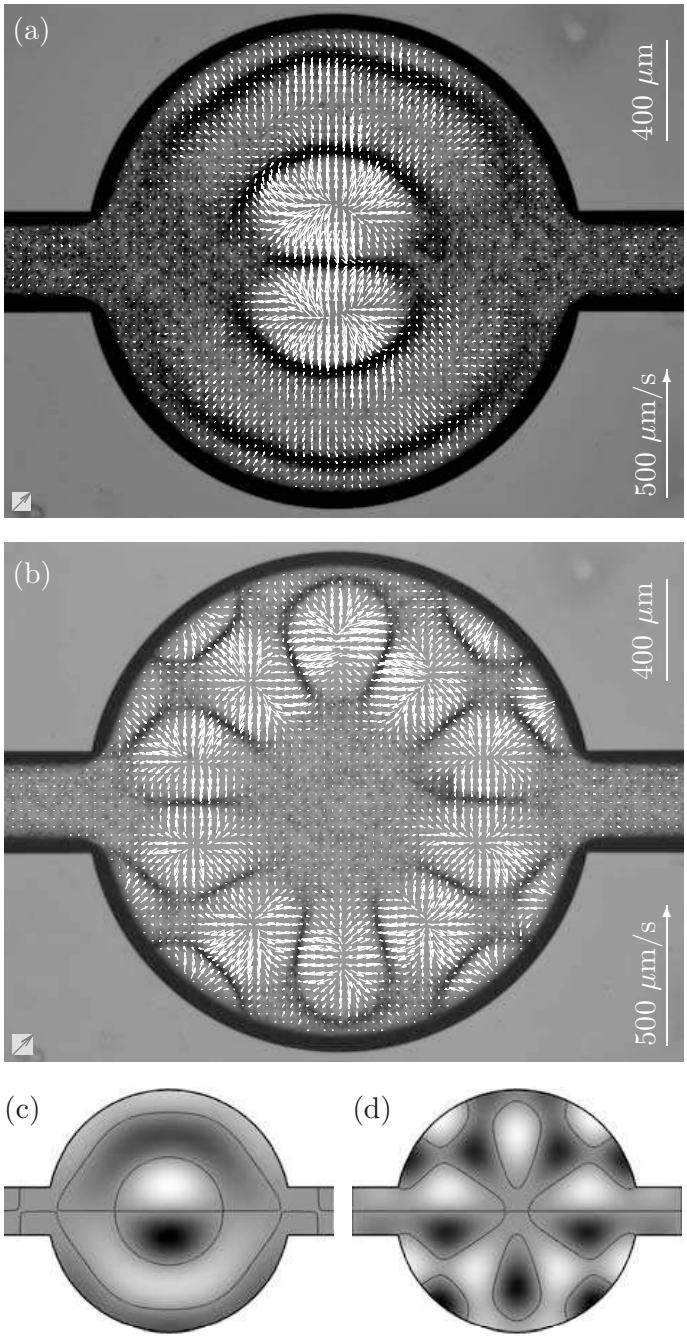

Figure 4.3: Acoustic radiation force. (a) Experiments on 5 μm beads at the 1.936 MHz acoustic resonance. The white PIV-vectors indicate the initial bead velocities pointing away from pressure anti-nodes immediately after the piezo-actuation is applied. The picture underneath the PIV-vector plot shows the particles (black) gathered at the pressure nodal lines 3 seconds later. (b) As in panel (a) but now at 2.417 MHz. (c) and (d) Gray-scale plots of numerical simulations in the 2D chamber model of the corresponding acoustic pressure eigenmodes. Nodal lines are shown in black.

resonances. More than 30 of such resonances have been detected, but we present only a few, which we find to be representative for the method and the problems associated with acoustics in microfluidics.

The most important results are the full-image micro-PIV analyses. For these, two types of experimental results are presented. One type are the PIV-vector plots (white arrows) of the motion of the tracer particles, in most cases corresponding to the transient motion immediately after the onset of the acoustic piezo-actuation. The other type are micrographs of the microfluidic chamber with the steady-state particle patterns (often visible as narrow black bands) obtained after a few seconds of actuation. These two types of images are superimposed to illustrate the relation between the initial motion of the tracer beads and their final steady-state positions.

The full-image micro-PIV analysis illustrations are also accompanied by the results of our numerical simulations in the form of gray-scale plots of the pressure eigenmodes $p_n(x, y, z)$. The pressure antinodes appear as white (positive amplitude) and black (negative amplitude) regions. The pressure nodal lines are shown as thin black lines in the gray (small amplitude) regions.

Additionally, we show a close up measurement of a streaming vortex, and provide a more in-depth comparison between the measured velocities and the calculated body force.

Acoustic radiation force

We first show results for the acoustic resonances at 1.936 and 2.417 MHz in the circular chamber containing large 5 μm tracer particles.

In Figs. 4.3(a) and (b) are shown the measured transient PIV-vector plots superimposed on the micrographs of the chamber with the static steady-state particle patterns. The fact that the particles accumulate in static patterns indicates that the dominant force on the tracer particles is the acoustic radiation force, an observation also expected from the relatively large size of the tracer particles. The matching numerically calculated acoustic eigenmodes of the 2D chamber model are shown in panels (c) and (d). It is noteworthy that even for the complicated resonance pattern of panels (b) and (d), the observed transient particle motion towards the steady-state positions, and the static steady-state patterns themselves, are in good agreement with the numerically calculated pressure nodal lines. This demonstrates that even the simple 2D chamber model can predict what kind of fluidic behavior will be observed in the device. It also demonstrates that full-image micro-PIV analysis in combination with images of transient particle motion is effective in visualizing in-plane acoustic phenomena in micrometer-scale devices.

Acoustic streaming

To illustrate the difference between the acoustic radiation force and acoustic streaming, we now turn to the acoustic resonance at 2.17 MHz in the square chamber containing large 5 μm beads and small 1 μm beads as shown in Figs. 4.4(a) and (b), respectively.

When micro-PIV is applied to investigate acoustic effects in microfluidic chambers, the simultaneous presence of both acoustic radiation forces and acoustic streaming needs

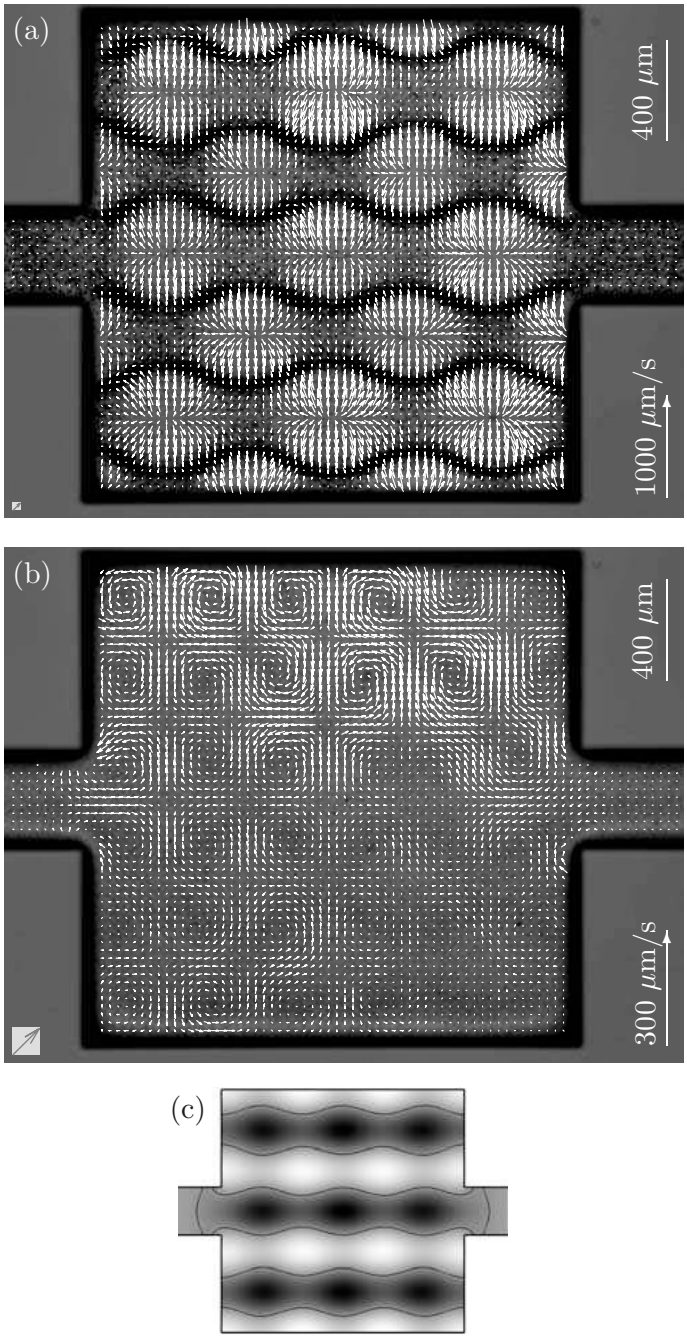

Figure 4.4: Acoustic streaming and radiation forces at the 2.17 MHz acoustic resonance. (a) Experiments on 5 μm beads similar to Fig. 4.3(a) showing that the acoustic radiation force dominates for large particles. (b) Experiments on 1 μm beads. Acoustic streaming dominates and the small beads act as tracers for the motion of the liquid. The resulting vortex structure in the flow-field prevents particle accumulation at the pressure nodes. (c) Gray-scale plot of numerical simulation in the 2D chamber model of the corresponding acoustic pressure eigenmode. Nodal lines are shown in black.

to be taken into account. For the large beads in Fig. 4.4(a) the acoustic radiation force dominates exactly as in Figs. 4.3(a) and (b), which results in particle accumulation at the pressure nodal lines. However, as shown in Fig. 4.4(b) reduction of the particle volume by a factor of 125 leads to a qualitative change in the response. The motion of the smaller particles is dominated by the acoustic streaming of the water, and it manifests itself as a 6×6 pattern of vortices. The same 6×6 pattern was found by full-image micro-PIV when diluted milk was used as tracer solution, and also by optical inspection with a fluorescein solution in the chamber (data not shown). All three experimental results strongly support the interpretation that the 6×6 vortex pattern is caused by acoustic streaming.

In Fig. 4.4(b) is also seen a pronounced inhomogeneity in the strength of the vortices across the microfluidic chamber. This effect cannot be ascribed to the geometry of the chamber, but is probably due to either a geometric top-bottom asymmetry in the entire chip (similar to the left-right asymmetry discussed in Sec. 4.3.4 – Effects of geometric asymmetries), or to an inhomogeneous coupling between the piezo-actuator and the silicon chip. If the frequency is shifted slightly in the vicinity of 2.17 MHz, the same vortex pattern will still be visible, but the strength distribution between the vortices will be altered. When investigating acoustic phenomena the advantage of full-image micro-PIV compared to partial-image micro-PIV is thus evident: partial-image micro-PIV employed locally in a part of the chamber would not have shown the symmetrical 6×6 vortex pattern, nor would it supply us with information of the inhomogeneity in strength for the same. Moreover, since the same inhomogeneity is not seen in the acoustic radiation force vector plot, this example shows that there is no direct relation between the strength of the acoustic streaming and the acoustic radiation force.

Finally, we note that our measurements show that the acoustic radiation force on the large particles leads to a much larger particle velocity than the acoustic streaming velocities of the smaller particles.

Turning to the numerical simulation in the 2D chamber model of the corresponding pressure eigenmode, shown in Fig. 4.4(c), we find good agreement with the experimental results. The calculated pressure nodal lines correspond well to the static steady-state particle patterns obtained with the large tracer particles dominated by the acoustic radiation force. Moreover, the calculated 3×3 antinode pattern is also consistent with the observed period-doubled 6×6 vortex pattern of the small tracer particles dominated by acoustic streaming. The spatial period-doubling arises from the non-zero time-average of the non-linear term in the Navier–Stokes equation governing the attenuated acoustic flows leading to acoustic streaming [62].

Effects of geometric asymmetries

For the results presented so far the simple 2D chamber model proved sufficient to interpret the experimental observations. However, as explained already in Sec. 4.3.3 the pressure eigenmodes are not confined to the chamber region but fill the entire chip. The acoustic resonances even propagate in all media (air and piezo-actuator) in contact with the chip. In the following we show one example of asymmetric resonance patterns that can only be explained by employing the more complete 2D chip model or by introducing asymmetries

in the 2D chamber model.

In Figs. 4.5(a) and (b) we consider the square chamber containing the large 5 μm beads at two nearby resonance frequencies, 2.06 and 2.08 MHz. As before, the acoustic radiation force dominates and the beads accumulate at the pressure nodal lines. Note that the two patterns are similar, but that the first has a higher amplitude on the left side, while the second has a higher amplitude on the right side. Both resonance patterns are similar to the acoustic pressure eigenmode shown in Fig. 4.5(c), which is found by numerical simulation using the 2D chamber model. However, since the chamber itself is left-right symmetric, the calculated eigenmode is also left-right symmetric, so to explain the observed asymmetry we have to break the left-right symmetry in the theoretical model. We investigate two ways of doing this: first, in the 2D chip model by placing a symmetric chamber asymmetrically on the chip, and second, in the 2D chamber model by letting the inlet channel have a different length than the outlet channel.

In Figs. 4.6(a–d) is shown the result of a numerical simulation in the 2D chip model where the left-right symmetry has been broken by displacing the chamber 1 mm left of the symmetry center of the chip. This displacement corresponds to the geometry of the actual chip used in the experiment. Panels (a) and (b) show the entire chip while panels (c) and (d) are the corresponding closeups of the chamber region. With this left-right asymmetric geometry, we do find asymmetric solutions at nearby frequencies that resemble the measured patterns: Figs. 4.6(c) and (d) correspond to Figs. 4.5(a) and (b), respectively. In the left-right symmetric case the left-right acoustic resonance is two-fold degenerate, i.e., two different resonances have the same frequency. When the symmetry is broken the two resonances are affected differently: one gets a slightly higher eigenfrequency and the other a slightly lower, i.e., a splitting of the two-fold degenerate eigenfrequency into two non-degenerate nearly identical eigenfrequencies. The two closely spaced eigenmodes of the asymmetric 2D chamber model shown in Figs. 4.6(e) and (f) also resemble the measured patterns in Figs. 4.5(a) and (b). The calculated frequency splitting is 28 kHz, which is in fair agreement with the measured 20 kHz.

Unquestionably, advanced models, like the chip model, are necessary for more complete theoretical investigations of how different factors contribute to the breaking of the symmetry of the simple chamber model. Experimentally this effect could be studied by measuring on a range of devices, with strictly controlled geometries of both structures and substrates. We have only investigated two devices, and special concern was not taken as to the uniformity of the substrate. It is therefore not possible in the present study to determine whether the observed symmetry breaking was due to geometric asymmetries in the chip, in the chip-actuator coupling, or in other parts of the system (such as air-bubbles trapped at the fluidic inlet and outlet).

Validation of method

Fig. 4.7 shows a micro-PIV vector plot of streaming motion in the center of the square chamber at 2.17 MHz, recorded with a 20× microscope objective. With this kind of recording, detailed information of a section of the device can be obtained, but it will not supply any information about the amplitude fluctuations over the device, nor does it reveal

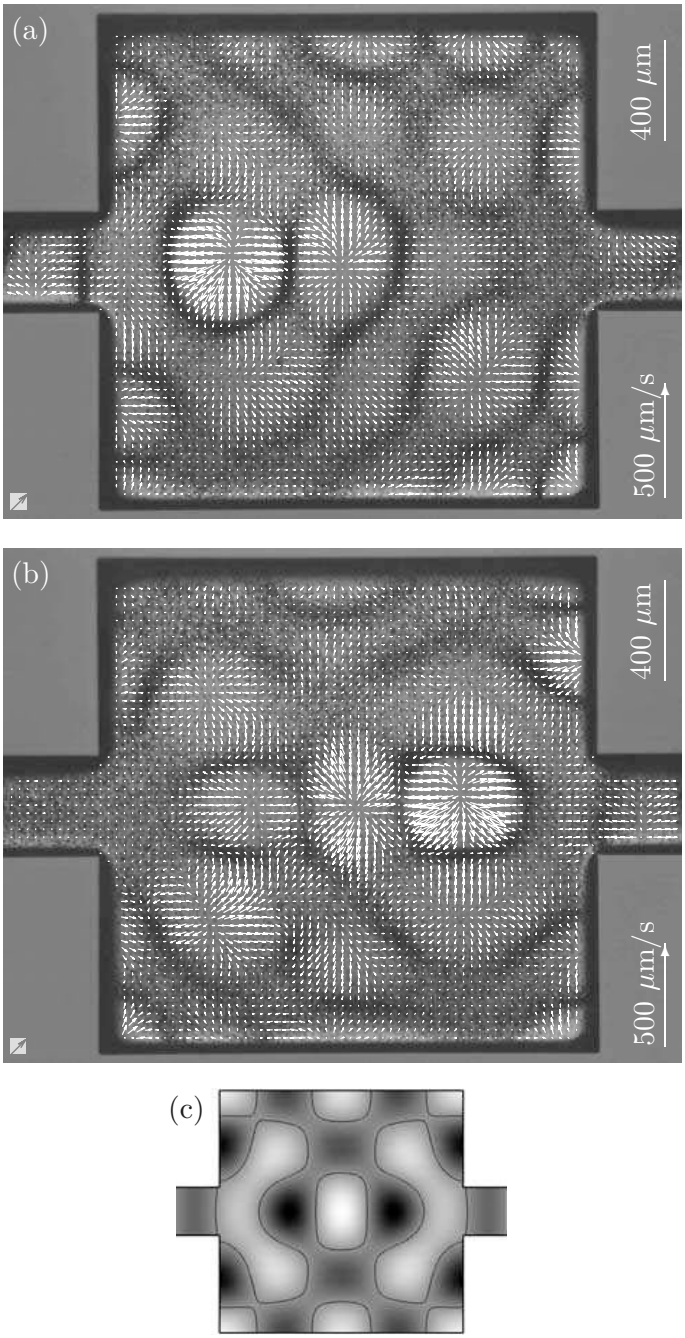

Figure 4.5: Splitting of a two-fold degenerate acoustic resonance due to geometrical asymmetry. (a) Acoustic radiation force as in Fig. 4.4(a) on 5 μm beads at the 2.06 MHz resonance. (b) The closely related 2.08 MHz resonance for the same system. (c) Gray-scale plot of numerical simulation in the left-right symmetric 2D chamber model of the corresponding two-fold degenerate, un-split, acoustic pressure eigenmode. Nodal lines are shown in black.

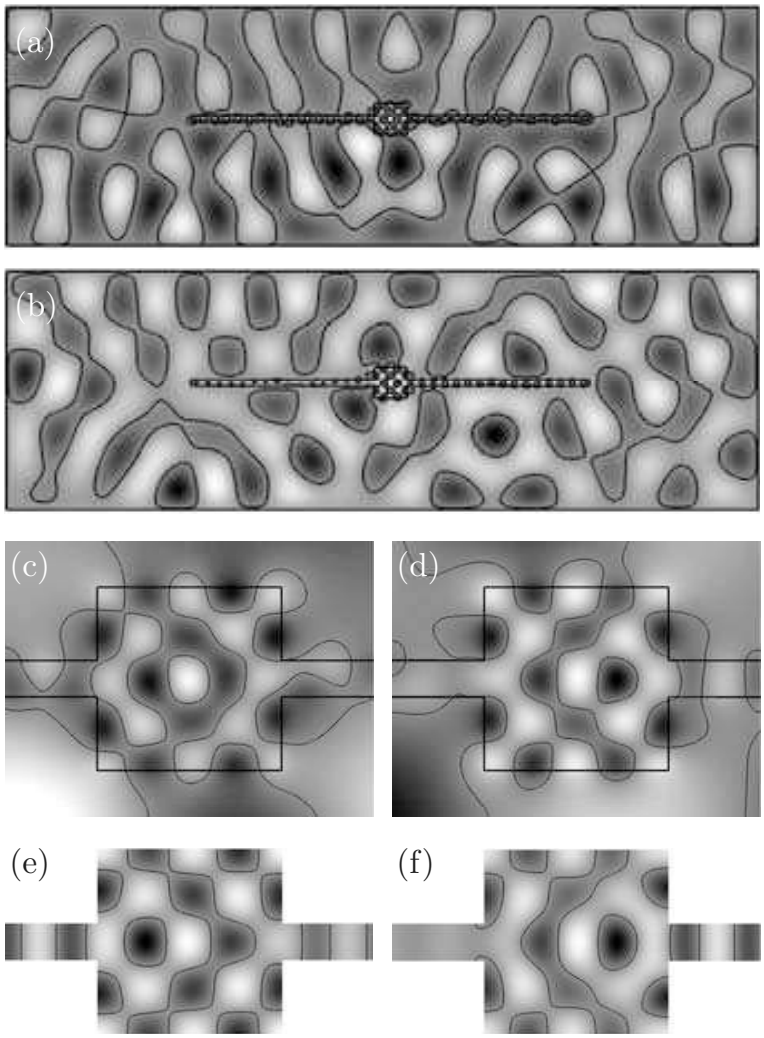

Figure 4.6: (a) and (b): Gray-scale plots of numerical simulations in the 2D chip model of two closely spaced acoustic pressure eigenmodes. The chamber is displaced 1 mm to the left of the symmetry center of the chip thereby breaking the left-right symmetry and splitting the two-fold eigenmode degeneracy. The difference in eigenfrequency is only 1 kHz. (c) and (d): Closeups of the chamber region showing the asymmetric eigenmodes similar to the experimentally observed resonances seen in Fig. 4.5. (e) and (f): Gray-scale plots of numerically simulated pressure eigenmodes in the asymmetric 2D chamber model, where the left lead is 1 mm shorter than the right lead. The difference in eigenfrequency is 28 kHz, which is close to the observed difference of 20 kHz in Figs. 4.5(a) and (b).

the 6×6 vortex pattern as seen in Fig. 4.4(b). Clearly, more detailed measurements of specific features are valuable, but for studies of resonances in low attenuation microfluidic devices, full-image recordings are of most importance.

Using the general expression for the energy U of a compressible particle in an acoustic

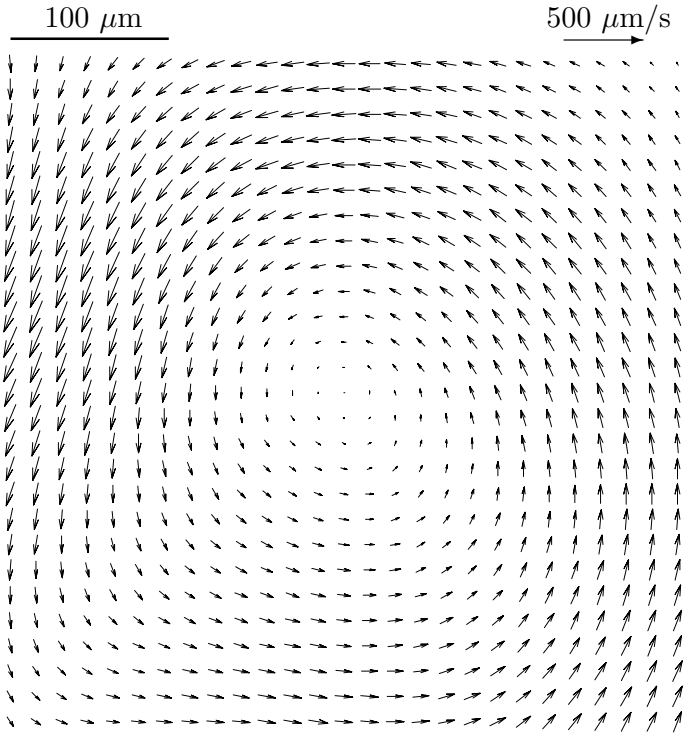

Figure 4.7: Micro-PIV velocity vector plot of streaming motion in the center of the square chamber at 2.17 MHz. Images were recorded with a 20× objective and a 0.63× Tv-adapter, and milk was used as tracer particles.

field [38], we can estimate the acoustic radiation force as the negative energy gradient, $\mathbf{F}_{ac} = -\boldsymbol{\nabla} U = \tau p_2 \boldsymbol{\nabla} p_2$, where τ is a constant parameter for each kind of particle, and p_2 is the time-averaged second-order pressure field. As τ is an unknown positive constant for red blood cell-like particles, the amplitude becomes a fitting parameter. Assuming that the particles move in a quasi-stationary steady state, we can obtain an expression for the velocity field by employing Stokes' drag law,

$$\mathbf{v} = \frac{\tau}{6\pi\eta a}\, p_2 \boldsymbol{\nabla} p_2. \tag{4.6}$$

Using this expression we can directly compare calculated and measured velocity patterns as seen in Fig. 4.8, where the calculated velocity pattern is compared with a scalar map of the velocity in y-direction, extruded from the measurement presented in Fig. 4.4(a). A comparison between the two is also seen in Fig. 4.9, where two vertical cross-sectional views, each located 330 μm away from the center of the chamber, are compared with the theoretical estimate. Both micro-PIV velocity plots show a good agreement with the calculated one, and the fluctuations in amplitude over the device can be seen by comparing the two micro-PIV velocity plots with each other.

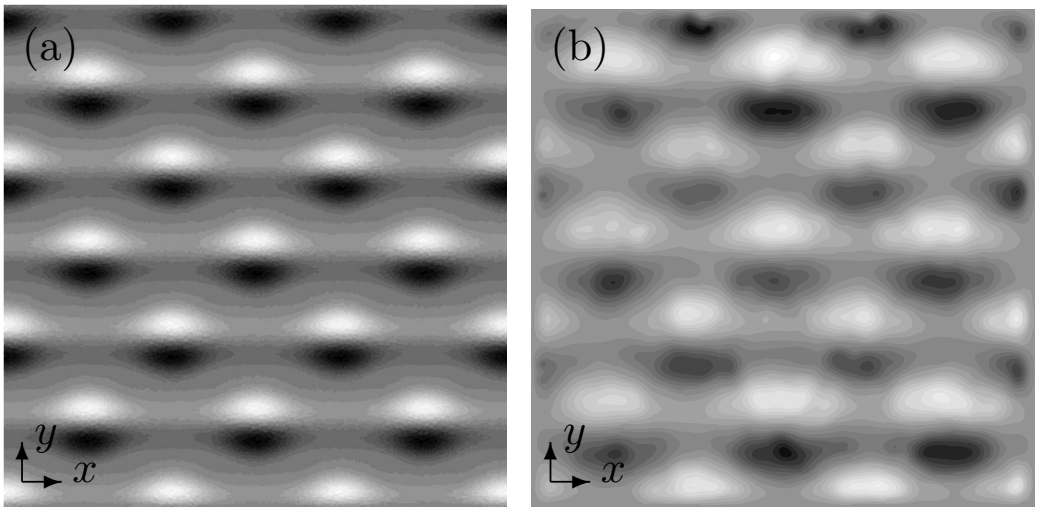

Figure 4.8: (a) The velocity in the y-direction calculated by Eq. (4.6) as $p_2 \nabla p_2$ using COMSOL Multiphysics. (b) Scalar map of the velocity in y-direction, measured with micro-PIV.

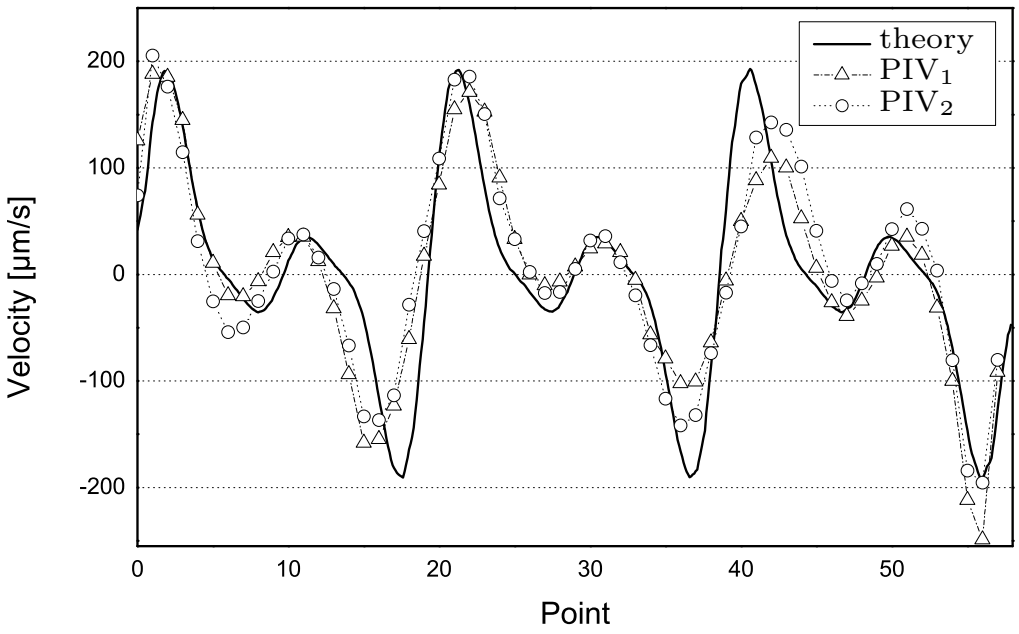

Figure 4.9: Vertical cross-sectional plots of the measured velocity in the y-direction (PIV_1) 330 μm left and (PIV_2) 330 μm right of the center of the chamber. The full line (theory) is the velocity in the y-direction calculated by Eq. (4.6) as $p_2 \nabla p_2$ using COMSOL Multiphysics, and with an amplitude fitted to match the velocity measurements.

4.3.5 Conclusion

Using full-image micro-PIV we have made direct observations of the acoustic resonances in piezo-actuated, flat microfluidic chambers containing various tracer particles.

Depending on the size of the tracer particles either the acoustic radiation force or acoustic streaming of the solvent dominates their motion. Large particles are dominated by the acoustic radiation force that pushes them to the static pressure nodal lines, while small particles are dominated by acoustic streaming and end up forming steady-state vortex patterns. However, for an arbitrary frequency and geometry one of the forces can be strong whereas the other is not, and it is therefore always necessary to apply more than one tracer solution in order to determine which forces are present.

The observed acoustic resonances correspond to the pressure eigenmodes found by numerical simulation of 2D models of the system. The symmetric patterns can be explained by using the simple 2D chamber model, while asymmetric patterns can be explained by using the more complete 2D chip model taking into account the geometric asymmetries of the surrounding chip, or in special cases, by an asymmetric 2D chamber model.

We have demonstrated that full-image micro-PIV is a useful tool for complete characterization of the in-plane acoustically induced motion in piezo-actuated microfluidic chambers.

Acknowledgement

SMH was supported through Copenhagen Graduate School of Nanoscience and Nanotechnology, in a collaboration between Dantec Dynamics A/S, and MIC, Technical University of Denmark.

end of paper

Chapter 5

Micro-PIV investigations of acoustically actuated microdevices

During the course of this PhD study, several acoustically actuated microdevices have been investigated. In this chapter, a selection of the examined devices is presented. The most thorough study is provided in Sec. 5.1, in which the investigation scheme described in Chap. 4 is applied for the examination of an acoustic separator. This section is essentially structured as a paper, because the text originates from my draft that later formed the publication *Acoustic resonances in straight micro-channels: Beyond the 1D-approximation* [17]. Section 5.2 features additional examples of acoustically actuated microdevices subjected to micro-PIV investigation. These examples are intended to further emphasize the complexity of these devices, as well as the difficulties involved in investigating them.

5.1 Investigation of an acoustic separator

In this section, we investigate an acoustic separator through micro-PIV analysis in stop-flow mode and numerical simulations, and a strong agreement between the two is found. Moreover, we demonstrate that it is not sufficient only to characterize devices in flow-through mode, since in these systems much different resonant patterns can result in similarly looking band formations (measurements in flow-through mode are also discussed in Sec. 5.2.1). Furthermore, we conclude that extended 1D approximations of the acoustic radiation force are inadvisable, and instead, a 2D model is preferred. The results presented here provide valuable insight into the nature and functionality of acoustic microdevices, and should be useful in the interpretation and understanding of the same.

5.1.1 Introduction

Acoustic actuation poses an attractive option for the performance of various relevant microfluidic tasks. Successful demonstrations of acoustic forces used for enrichment [41, 42], mixing [43, 44], cell handling [48, 49], medium exchange [63], separation [50, 51, 52, 64],

sorting [65] and others, have been provided.

However, the evaluation of these devices is mostly limited to quantifying and commenting on the net effect of the acoustic actuation in these systems as a whole, rather than investigating more locally how the desired effects are actually achieved. Moreover, numerical modeling of acoustic formation in the microfluidic designs has not been successfully reported, and, instead, the description of a sphere in a 1D standing wave [36, 37, 38] is typically supplied and described as extending uniformly for the whole length of a channel of constant width [41, 42, 48, 50, 51, 52].

In this work, we apply the method of investigation described in Chap. 4 for the examination of a previously well documented microchip based acoustic separator device [50]. We chose to work with this device as it has a non-complex design, which makes it attractive for both the experimental micro-PIV investigation and the numerical simulations. The device operates in continuous mode and has its function in that it can separate suspended particles from their medium. Moreover, the acoustic separator has seen a large number of successors [51, 63, 65, 66], intended for various microfluidic scenarios and functionalities, which makes it a suitable representative for a whole range of devices actuated and fabricated in a similar manner [67]. The results presented herein are foremost representative for these devices, but anticipate that similar behavior is to be expected and that the same conclusions are valid for other actuation variants and chip designs as well.

The current investigation has shown that the acoustic resonances are indeed of more complex nature than what is described by an extended 1D approximation. The experimental results were also found to agree with numerical 2D simulations. A discussion on this acoustic separator, and similar devices, is provided.

5.1.2 Materials and methods

The investigated acoustic separator was defined in a silicon substrate by the use of UV-lithography and chemical wet etching. After etching, the channel was sealed by a glass lid through anodic bonding, and silicone tubings were glued to the backside of the chip, for easy attachment of fluidic connections. A more detailed description of the fabrication process can be found in Nilsson *et al.* [50]. A sketch of the microchannel and the surrounding silicon substrate is seen in Fig. 5.1.

The device was actuated by a piezo ceramic (Pz26, Ferroperm Piezoceramics), pressed to the backside of the chip and acoustically coupled via an ultrasonic gel (Aquasonic Clear, Parker Laboratories) in between for good acoustic energy transmission. The transducer was biased by a signal generator (33250A, Agilent), the effective power measured by a digital power meter (Model 5000-EX, Bird Electronic Corp.) and the amplitude monitored by an oscilloscope (TDS 210, Tektronix Inc.). The micro-PIV equipment was set up and operated in the same way as described in Chap. 4. The 2D chip model, and 2D chamber model simulations using COMSOL Multiphysics finite element software, were also performed in an analogous manner.

For the separation efficiency measurements, the flow rate was controlled by a syringe pump (WPI SP210iwz, World Precision Instruments), and injection valves (Rheodyne 7000, Cotati) with a fixed loop volume were used to take samples. On the other hand,

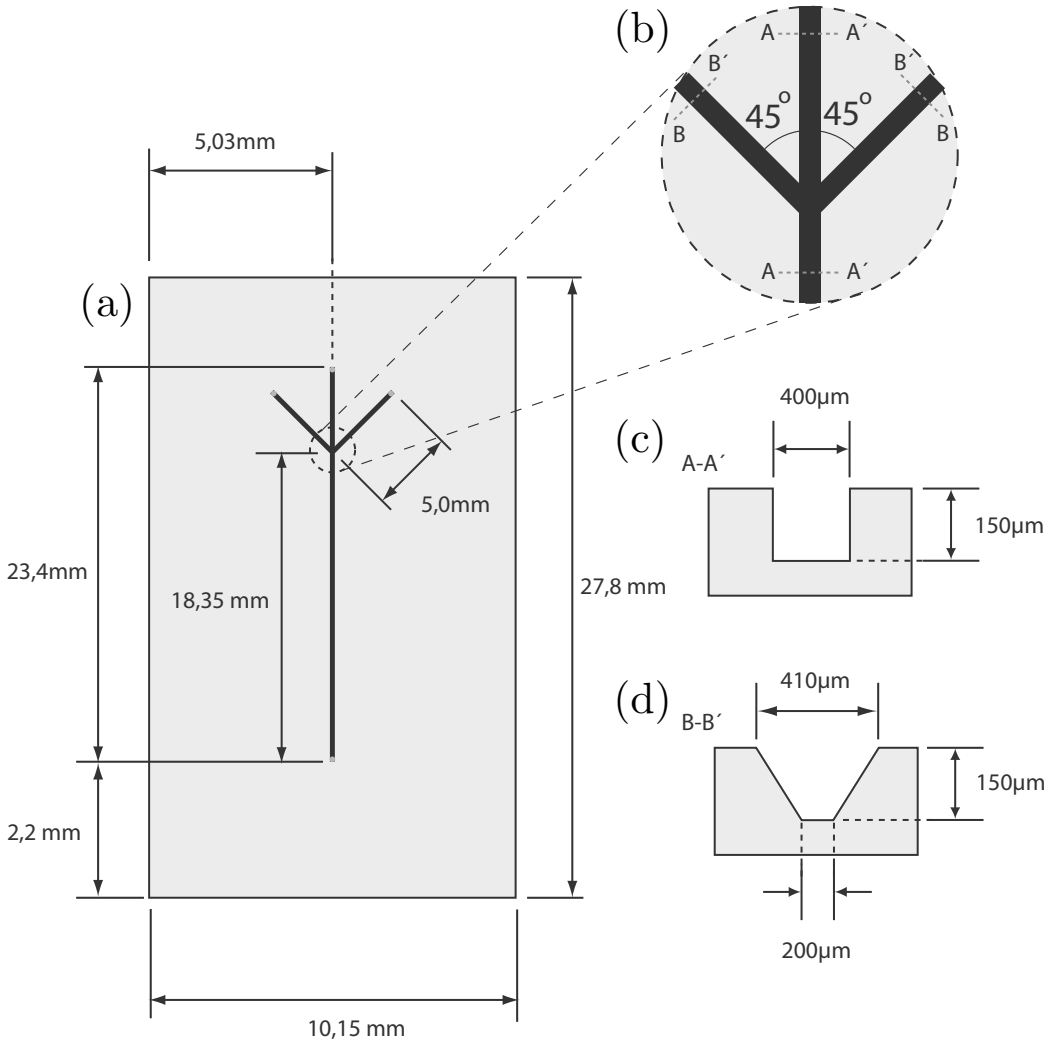

Figure 5.1: Sketch with dimensions of the separation chip used in the experiments. (a) Top view of the micro-channel and the surrounding silicon substrate. (b) Close up in junction region. (c) Cross-sectional view of the main channel. (d) Cross-sectional view of the side channels.

during the micro-PIV measurements, the same injection valves were used to stop the flow so that only particle motions created by acoustic effects were measured. As tracers 5 μm polyamide micro-beads (Danish Phantom design) and 1 μm fluorescent polystyrene micro-beads (Duke Scientific) were used. The larger particles were also used in the separation efficiency measurements, where the number of particles passing through the middle and the side outlets, respectively, was counted using a Coulter counter (Multisizer 3, Beckman Coulter Inc.).

5.1.3 Results and discussion

1D approximation and 2D simulations

The most dominant acoustic effect for larger particles positioned inside an acoustic standing wave field is the acoustic radiation force [36, 37, 38]. For a one-dimensional standing planar acoustic wave, the force $\mathbf{F}_r$ on a sphere at the distance x from a pressure node can be described as [37],

$$\mathbf{F_r} = -\left(\frac{\pi p_0^2 V_p \beta_m}{2\lambda}\right) \phi(\beta,\rho)\ \sin(4\pi x), \tag{5.1}$$

$$\phi(\beta,\rho) = \frac{5\rho_p - 2\rho_m}{2\rho_p + \rho_m} - \frac{\beta_p}{\beta_m}, \tag{5.2}$$

where λ is the ultrasonic wavelength, p_0 is the pressure amplitude and V_p the volume of the sphere. The factor ϕ defines in which direction the particles will move, either towards or away from the pressure nodes, depending on the relation between the densities and compressibilities of the particle (ρ_p, β_p) and the medium (ρ_m, β_m).

This formula for a 1D wave is often used in the literature to describe the effect of the acoustic radiation force in microfluidic channels [41, 42, 48, 50, 57, 58, 63, 64, 65, 66, 68, 69]. Typically, the focusing effect is described as a confined extension of the 1D case along the length of the channel of frequency matching width. Acoustic effects are often not ascribed to the parts of the system where there is no frequency matching. The acoustic separator examined in this work described by the extended 1D model, with a channel width of 400 μm and a sound velocity in water of 1483 m/s (20°C), yields $\lambda =$ 800 μm equivalent to an ideal frequency $f \sim$1.85 MHz for half a wave length over the width of the channel. Due to various loss mechanisms, frequency-broadening of the acoustic resonance will occur, but the model only suggests resonant solutions with half a wavelength separation in between.

An improved description of an acoustically actuated microfluidic system can be obtained by finding eigenmode solutions p_n to the Helmholtz eigenvalue equation (see Sec. 4.3.3). If the Helmholtz eigenvalue equation is solved for the idealized 2D chamber model of the acoustic separator, the result is much different to that suggested by an extended 1D model. Instead of a single solution for one specific frequency, the 2D chamber model suggests several solutions within a rather wide frequency span. More specifically, instead of a uniform pressure amplitude along the length of the channel, the solutions display an increasing number of "pinching regions" along the channel (see Fig. 5.2). Starting at 1.85 MHz, where we have one full ($n = 1$) pinching region, solutions were identified for all integer values n, up to $n = 32$ for 2.25 MHz. The frequency shift between the solutions were in the range of 1.5–15 kHz, with a tendency of larger separations for higher frequencies.

These solutions can be understood by considering that the acoustic eigenmodes in the channel system are dominated by, primarily, a transverse wavelength λ_t and a longitudinal wavelength λ_l contributing to the forming standing wave pattern. As the Helmholtz eigenvalue equation is modeled with a hard wall boundary condition, the resonant wavelengths

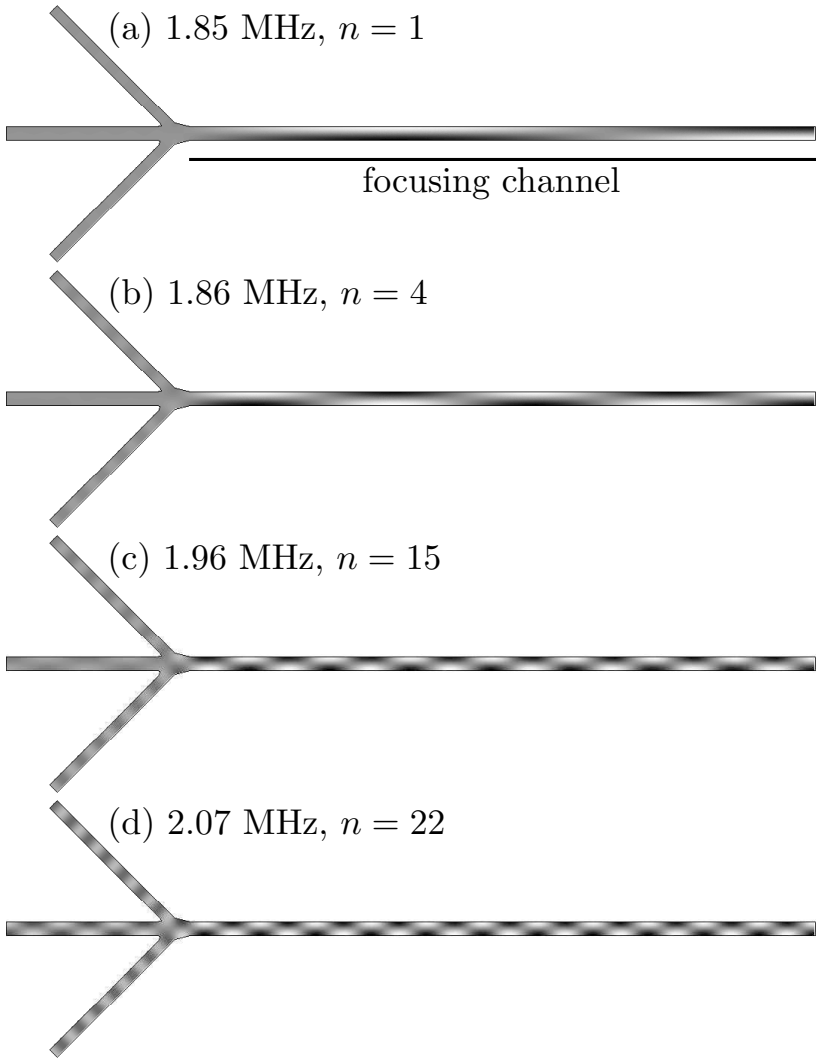

Figure 5.2: Gray-scale plots of the pressure eigenmodes p_n for the chamber model at (a) 1.85 MHz, (b) 1.86 MHz, (c) 1.96 MHz and (d) 2.07 MHz. The integer value n is the number of pinching regions in the focusing channel.

will be fractions of the channel dimensions. The resonance frequencies f can be estimated by

$$f = c_w \sqrt{\lambda_t^{-2} + \lambda_l^{-2}} \tag{5.3}$$

where c_w is the sound velocity in water. We consider solutions for which there is half a standing wave over the width of the channel, thus $\lambda_t = 2w$ with $w = 400$ μm. Similarly, we have $\lambda_l = 2L/n$, where L =18.3 mm is the length of the focusing channel. Since $w \ll L$,

f will be dominated by λ_t, and hence, a very small shift in frequency will result in a change of the number of pinching regions n. From this relation we can also conclude that if a microdevice is operated at a fixed frequency, even a small change in the temperature dependent sound velocity will cause a change in the number of pinching regions.

Device operated in flow-through mode

As a first investigation of the device, the chip was screened in flow-through mode, with continuous piezo actuation. The frequency of the AC voltage generator was scanned in the interval between 1.8 MHz and 2.2 MHz, while the separation effect was monitored. In the whole of this frequency span, a focusing effect of varying intensity was observed. In Fig. 5.3 stitched image frames recorded at three local maxima at a flow rate of 0.1 mL/min are shown. Of these three, the strongest focusing effect was seen at 1.86 MHz, even though the transmitted power was set to a lower value for this frequency than for the other two. The presence of several local maxima is in agreement with the results of the 2D chamber model simulations. On the other hand, the strong coupling at 1.86 MHz could be interpreted as a support for the extended 1D model, where the local maxima could stem from the mounted piezo's frequency dependence, or from the chip favoring coupling of certain frequencies. It is clear that more elaborate measurements are required in order to determine how well the different models agree with real devices.

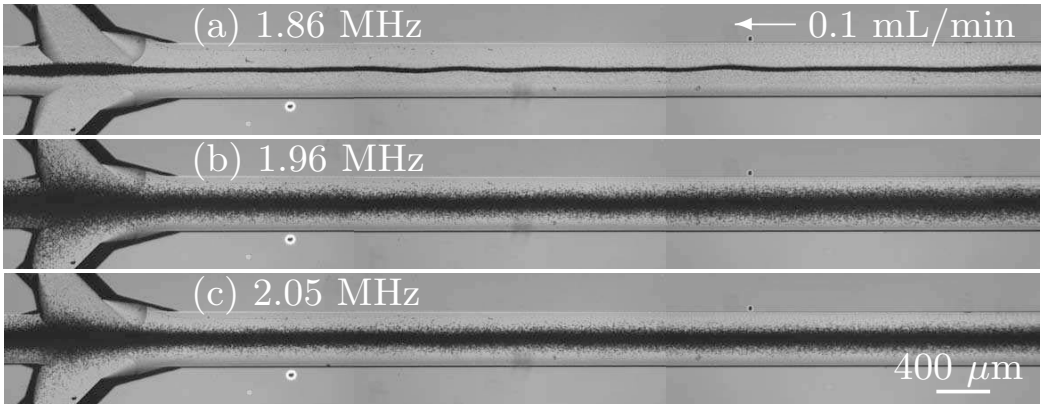

Figure 5.3: The separation device in operation at frequencies of (a) 1.86 MHz (b) 1.96 MHz and (c) 2.05 MHz. For comparison the same flow rate 0.1 mL/min was used in all panels (a)–(c). The transmitted power was set to 0.5 W in (b) and (c), and to 0.2 W in (a), where a relatively much stronger focusing effect was found. Note that only the last 6 mm of the 18.35 mm long focusing channel are shown.

Separation efficiency

The separation efficiency S was quantified at the three previously identified local acoustic maxima. S is defined as $S = P_{\text{center}}/P_{\text{tot}}$, where the number of particles collected from the center outlet P_{center} is divided by the total number of particles collected from all three

outlets $P_{\text{tot}} = P_{\text{center}} + P_{\text{waste}}$. The transmitted power was set to 0.5 W for frequencies 1.96 MHz and 2.05 MHz, and to 0.2 W for 1.86 MHz. For each frequency, six samples were collected at three different flow rates. A more efficient separation was achieved for the frequency of 1.86 MHz than for the other two, see Fig. 5.4. However, by adjusting the acoustic power and the flow rate, it was possible (at least apparent to visual inspection) to achieve close to complete separation at all frequencies.

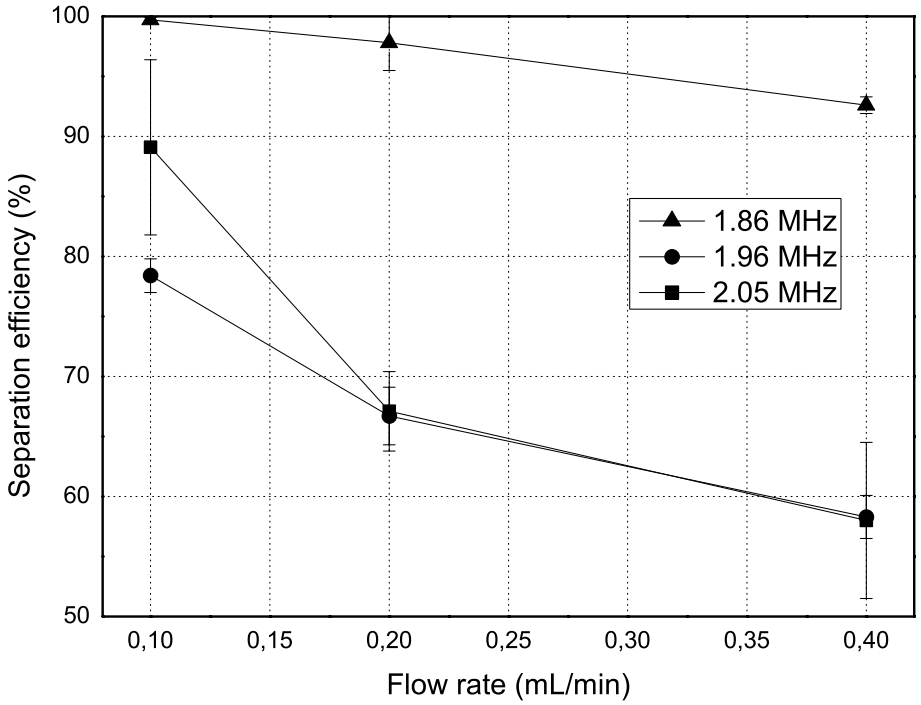

Figure 5.4: Separation efficiency ($S = P_{\text{center}}/P_{\text{tot}}$) versus flow rate at three different frequencies.

The difference in separation efficiency between 1.96 MHz and 2.05 MHz at the flow rate of 0.1 mL/min could be ascribed to a local focusing asymmetry within the channel junction. For higher flow velocities, the particles are not sufficiently long within this part of the channel system to be notably affected by these forces. This assumption is in agreement with the micro-PIV measurements of the acoustic radiation force presented below (top of Fig. 5.5).

Measuring the acoustic radiation force with micro-PIV

When the microfluidic device is operated in flow-through mode, it is not possible to determine what the actual focusing patterns look like, since the continuous flow mode yields an image of the integrated acoustic effect along the full length of the separation channel. Therefore, in order to get a better understanding of the function of the device, more qualitative measurements are required, such as stop-flow micro-PIV measurements. Furthermore, the identification of acoustic resonant patterns is facilitated if a larger section

of the device can be examined. Of course, there is a tradeoff between low and high magnification, as a low magnification has its drawbacks in both reduced in-plane, and in-depth, resolution. Here, images were recorded at three partially overlapping positions, each with a total magnification of 3.15×, starting from the channel junction covering a distance approximately 6 mm upwards in the channel. In Fig. 5.5 the micro-PIV results of measurements performed with no external flow applied, but with the same frequencies and transmitted powers as were used in the flow-through measurements, are shown. The larger 5 μm particles were used, and thus, the velocity vectors are primarily showing motion of the particles caused by the acoustic radiation force.

Notably, the results are clearly favoring the 2D chamber model solutions compared to the extended 1D model. First of all, the velocity vectors are not all pointing directly towards the middle, and, thus, it is not solely a case of varying intensity along the length of the channel. Instead, the focusing is performed in certain pinching regions, as suggested by the chamber model. Secondly, the number of pinching regions is increasing with the frequency, which was also predicted by the chamber model (see Fig. 5.2).

From the measurements we can see that even though the 2D chamber model gives valuable and valid information about what the principal focusing pattern will look like, it is far from an exact representation of the actual resonant pattern formed in the system. This is because the acoustic resonances are not confined to the microfludic channels only, but are rather formed over the entire chip. An improved understanding of what the actual resonances may look like, can be given by a 2D chip model (see Sec. 4.3.3). Two such solutions, solved for the measured dimensions of the whole device (Fig. 5.1), are shown in Fig. 5.6. These solutions are examples of global resonances that can explain the displacements and intensity irregularities of the patterns seen in the separation channel. However, it is important not to over-interpret the results of the chip model. In the actual situation there are several effects that are not taken into account by the model, such as irregular coupling from the resonator, discrepancies between the measured and actual dimensions of the device, overlapping of resonances, degenerations and 3D effects. In order to obtain a quantitative agreement, a full 3D simulation is required, including exact knowledge of the previously mentioned effects. Therefore, it is futile to search for an exact match between the measured displacements and the resonant patterns given by the 2D chip model. Nonetheless, the chip model has a value in the understanding of the formation of the acoustic resonances, although the principal solutions given by the simpler chamber model can be of larger practical value in a process where a device is designed or characterized. In contrast, an extended 1D model has little practical value, and is often misleading.

Acoustic streaming results

So far, we have mainly focused on the acoustic radiation force, which is the acoustic effect utilized by the separation device. However, at the length scale of microfluidic devices, the acoustic radiation force is not the only acoustic effect which comes into play - acoustic streaming is also present [39, 40]. Since the acoustic radiation force scales with the volume of the particle, the streaming motion can generally be extracted by applying tracer particles

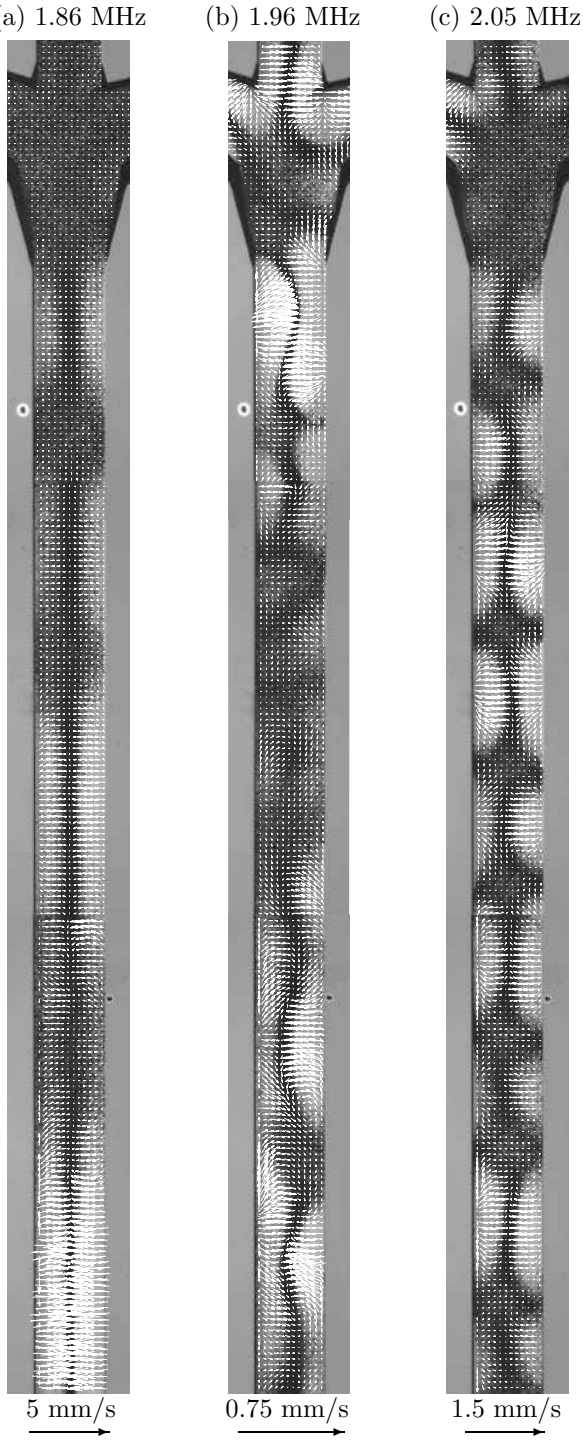

Figure 5.5: Velocity vectors for particle displacements in zero flow caused by the acoustic radiation force superimposed on images of transient particle motion. (a) 1.86 MHz, 0.4 s (b) 1.96 MHz, 2 s and (c) 2.05 MHz, 1 s. The number of pinching regions increases with the frequency. Reference vectors are shown at the bottom of each panel.

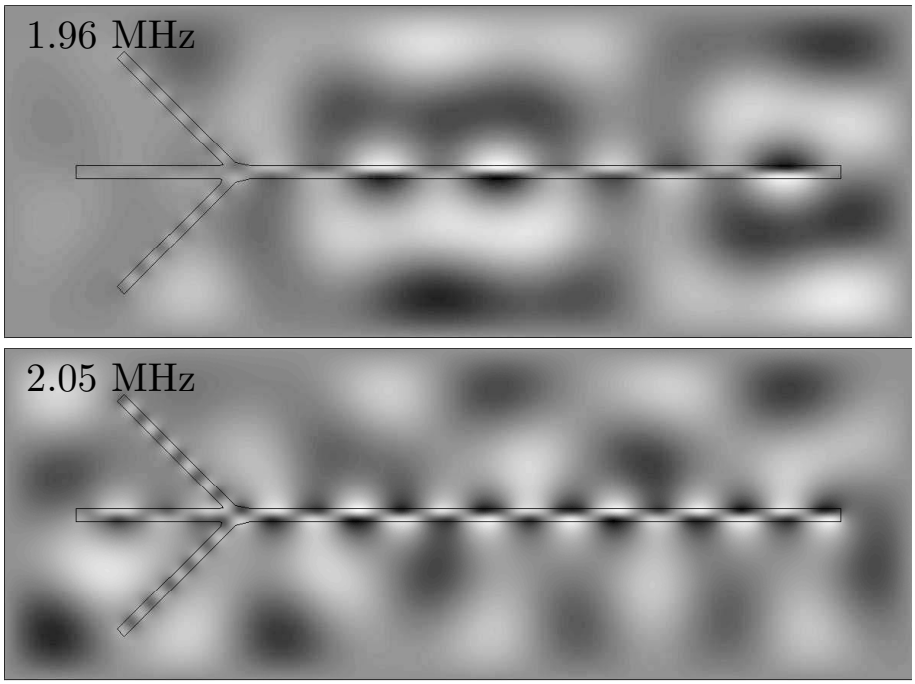

Figure 5.6: Chip model simulations shown for two frequencies, supplying an illustration of what the pressure patterns forming over the whole chip may look like. In comparison with the chamber model, the patterns inside the channels are more irregular, which is in agreement with the experimental observations. Note that the model underestimates the number of pinching points in respect to the frequency in the measurements (and in the chamber model).

of smaller size. In this study, we used 1 μm green fluorescent polystyrene spheres. Apart from the different particles, the streaming measurements were performed under similar conditions as for the micro-PIV measurements of the acoustic radiation force. The results are seen in Fig. 5.7.

As is evident, the streaming in the system is fairly weak compared to the much stronger acoustic radiation forces, and thus, it has minor influence on the functionality of this particular device. The streaming should, however, not be neglected, and for many micro-devices utilizing acoustic radiation forces, unwanted streaming could clearly pose a limitation to the function and efficiency of the same. Also worth noticing is that there is no direct relation between the acoustic radiation force and the streaming, where in one part of the channel one can be strong whereas the other is not (comparing Fig. 5.5 and Fig. 5.7). All in all, it is our recommendation that micro-devices designed to utilize the acoustic radiation force also should be examined for the presence of streaming, especially in the case where the acoustic radiation force magnitude is low and particle translation also is governed by shearing effects, which commonly is the case for particle sizes of 1 μm or smaller.

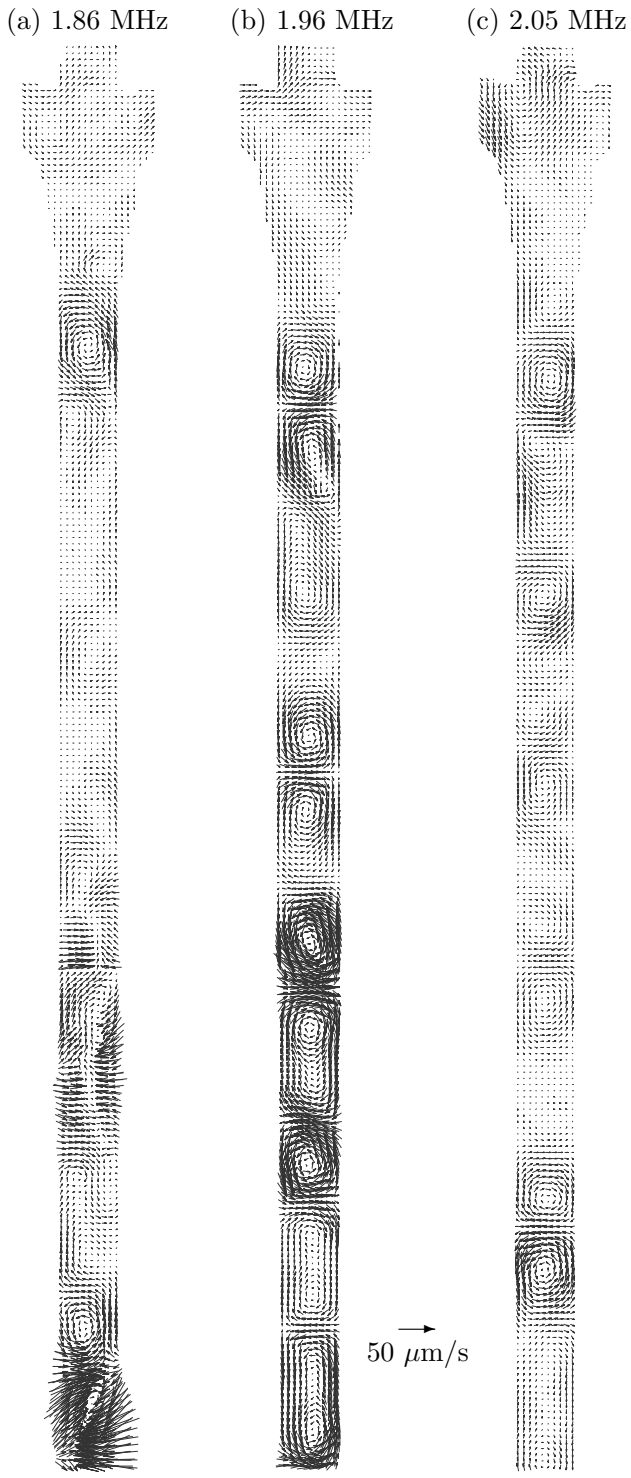

Figure 5.7: Velocity vectors of fluid motion caused by acoustic streaming. 1 μm tracer particles were used for recordings at (a) 1.86 MHz (b) 1.96 MHz and (c) 2.05 MHz. Reference vector is shown for 50 μm/s.

5.1.4 Conclusion

The function of the here investigated chip is not critically depending upon the exactness of the applied forming acoustic resonances. When operated in flow-through mode, the more refined effects are not directly apparent, which is most likely the reason why they have been over-looked, and not investigated, in previous studies. However, for several proposed micro-devices utilizing acoustic forces (especially for higher order of functionality than binary-separation or mixing) the local effects are of great importance to the outcome, and, thus, the overall success of the device. If the local effects are not understood and controlled, these devices have little chance of making it beyond the proof of principle stage in the research lab. Therefore, the author suggests that the extended 1D visualizations of acoustic coupling in microfluidic devices should be avoided, since they provide a misleading description of the phenomena in these devices. Instead, at least a simple 2D model should be considered and provided. Furthermore, our results have shown the importance of performing qualitative spatial measurements (such as those provided by the micro-PIV method) of the forming acoustic patterns, since the actual outcome of the acoustic actuation is difficult to predict. This is especially important for devices where the effect is intended to be confined to a much smaller spatial region than what is the case in the acoustic separator device examined here.

5.2 Additional examples of acoustically actuated microdevices

In this section, other examples of acoustically actuated microdevices subjected to micro-PIV investigations during the course of the PhD study are provided. Each example is intended to illustrate some important aspect of acoustically actuated microdevices, as well as the difficulties involved when performing investigations on the same.

5.2.1 Flow-through measurements in straight channels

The first micro-PIV measurements of acoustic forces that were attempted were performed in a straight channel with rectangular footprint (width $\sim$400 μm, height $\sim$140 μm) in flow-through mode. These structures, that had already been utilized in a previous research project [71], were fabricated similar to the acoustic separator described in Sec. 5.1. The results from this pre-study, both with regards to the revealed acoustic effects as well as the previously unconsidered constraints to the experimental conditions, heavily influenced the designs of the devices investigated in Chap. 4. Most of these topics are covered in Chap. 4 and in Sec. 5.1, and will therefore not be repeated again. Instead, these particular measurements are recalled to provide a further description of flow-through measurements.

As previously discussed in Chap. 4, the expulsion of tracers from certain regions into others is a clear limitation when micro-PIV is applied for the investigation of acoustic forces. Especially so in microdevices where the actuator is operating continuously. For example, the particles can be subject to acoustic forces upstream of the investigation region, disrupting the homogeneous particle distribution. The only way to circumvent this

problem is by decreasing the effect of the acoustic actuation or by increasing the velocity of the externally applied flow, so that the particle distribution does not become heavily disrupted. Thereafter, by subtracting the results from consecutive micro-PIV recordings from the same investigation region, with and without acoustic actuation applied, the acoustic effects can be separated from the motion of the particles caused by the externally applied pressure driven flow. However, considering the previously noted requirement that the motion of the particles caused by the acoustic effects has to be substantially smaller than the motion caused by the externally applied flow, extreme flow stability is required in order to succeed with this approach. This is typically not readily achieved in a practical situation.

One alternative is to utilize the fact that the externally applied pressure driven flow in a micro-channel is one-directional and typically of laminar nature. As a consequence, for the measured particle displacement perpendicular to the flow direction, the particle motion induced by acoustic effects will dominate. An illustration of this is seen in Fig. 5.8, where (a) shows the total in plane velocity, whereas (b) shows the u-velocity component only. This measurement reveals that the strength of the acoustic focusing effect is not

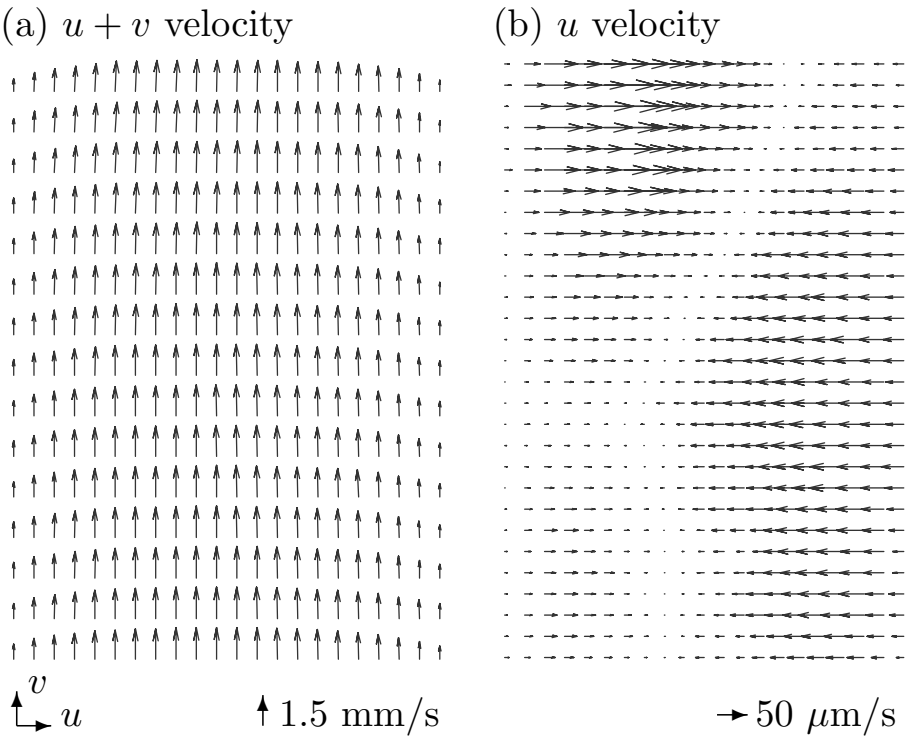

Figure 5.8: Velocity vector maps showing the flow in a straight microchannel with rectangular footprint recorded with a 20× magnification objective. (a) shows both the u and the v-velocity components. (b) shows the u-velocity component (v suppressed). In (a), only every second row of vectors are displayed.

homogenous along the channel. However, the investigation of the acoustic separator (see Sec. 5.1) demonstrated that the acoustic focusing effects are not one-directional (as proposed by an extended 1D-model), and therefore, this kind of vector suppression approach only partly describes the forming acoustic resonances. Therefore, even if flow-through measurements are desirable, it is the author's opinion that for investigating acoustic effects in microdevices the stop-flow approach is the preferred method of the alternatives that have been presented to date.

5.2.2 Investigation of spatial confinement

In a collaboration with researchers from Royal Institute of Technology, micro-PIV was applied to quantify the degree of spatial confinement in two variants of acoustically actuated microfluidic devices. A more detailed description of this study, here only described in brief, is found in Manneberg *et al.* [70] (see Appendix D). The first of the investigated micro-chips (denoted as the *step chip*) consisted of a channel divided into three sections of different widths. The second device (denoted as the *split chip*) was more complex and comprised by several channels where different particles could be combined and separated. A sketch of the devices is seen in Fig. 5.9. The spatial confinement was achieved by using a set of transducers, each frequency matched to a specific segment of the channel of a certain width. This approach to obtain spatial confinement by utilizing channels of different widths has been demonstrated previously, for instance by the author himself [71, 72].

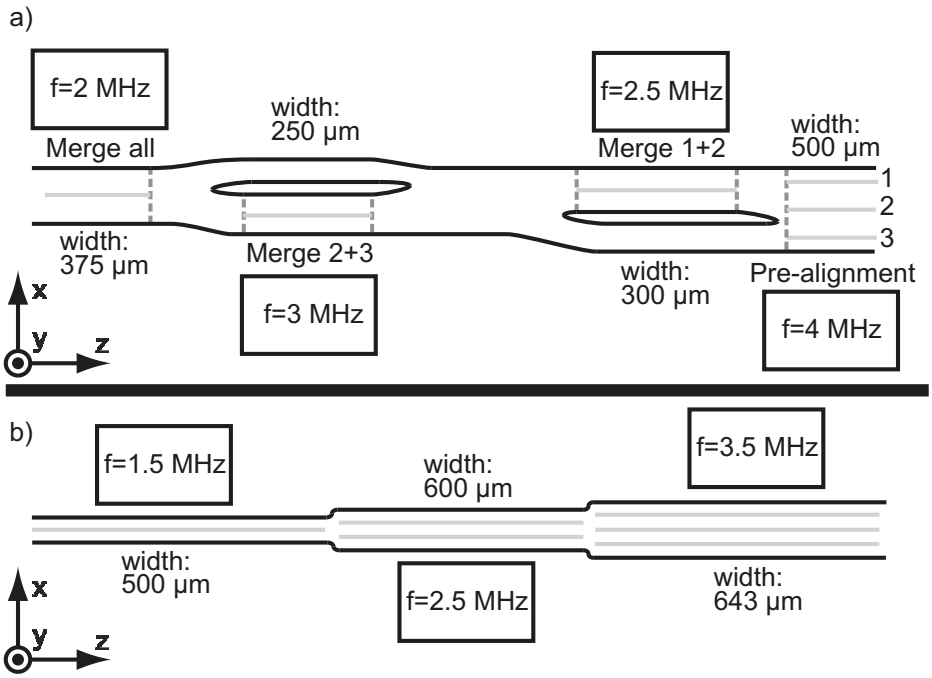

Figure 5.9: Footprints of the two micro-chips used in the investigation. Spatial confinement is achieved by utilizing selective frequency matching to channel segments of different widths [70].

When the microchips were run in flow-through mode, the acoustic focusing appeared to be well confined to the designated regions, much like what was seen in flow-through mode for the acoustic separator in Sec. 5.1. This observation was partly confirmed by stop-flow measurements (performed analogously to [16]) which are presented in Fig. 5.10.

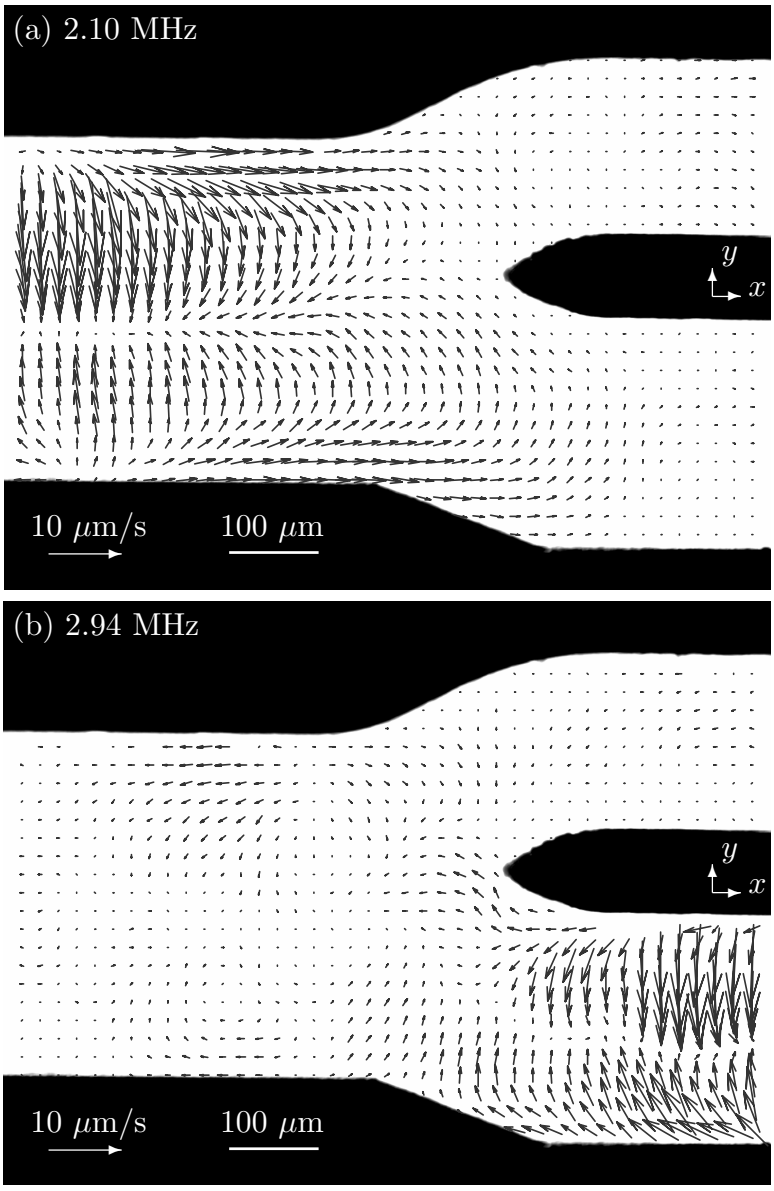

Figure 5.10: Stop-flow measurements in the split chip for one of the investigated sites. (a) Transducer 1 operating at 2.10 MHz. (b) Transducer 2 operating at 2.94 MHz. The acoustic resonances are effectively confined to the designated regions. The velocity vectors are calculated using 64×64 pixels interrogation areas with a 50% overlap.

The investigated "site" shown in this figure corresponds to the first channel junction to the left side of Fig. 5.9(a).

In Fig. 5.10(a) it is clearly seen that the transducer operating at 2.10 MHz primarily gives rise to focusing in the left channel of width 375 μm, whereas the second transducer operating at 2.94 MHz, which is seen in Fig. 5.10(b), is frequency matched to the bottom channel to the right with a width of 250 μm. When both transducers were applied simultaneously, the resulting particle motion was corresponding to the sum of the two [70]. Apart from measurements at different sites, the forming acoustic patterns were also examined along the length of the channels. The observed acoustic effects were pronouncedly inhomogeneous, and strong focusing could be seen in non-designated regions. However, the here investigated devices were not suitable for numerical analysis (the footprints were too extensive and too complex), and in order to understand the formation of these patterns, comparisons with investigations of less complicated systems, like the acoustic separator (see Sec. 5.1), are required.

5.2.3 Acoustic streaming at corners

One pronounced acoustic effect, often observed in acoustically actuated microdevices, is the presence of strong acoustic streaming in the proximity of sharp corners. The governing physics behind this phenomenon has not been investigated by the author (and to the author's knowledge not in any other study), and will therefore not be subject to further discussion here. However, in order to understand this phenomenon, and eventually to utilize it in microfluidic devices, experimental observations of this effect are valuable. In Fig. 5.11, one such example of acoustic streaming at a sharp corner is provided. The figure shows the same split chip, for which measurements were presented in the previous section, but performed at the next junction to the right (see Fig. 5.9(a)). The device is actuated by a transducer operating at 2.94 MHz, and acoustic focusing is achieved in the frequency matched channel to the bottom left in Fig. 5.11(a). However, even though relatively large 5 μm particles are used as tracers, the highest velocity is recorded for acoustic streaming in the proximity of the right end of the divider between the two channels. The closeup in Fig. 5.11(b), shows two rolls of opposed circular motion, where the fastest flow of the fluid is extending from the sharp point of the wedge. Undoubtedly, if understood and controlled properly, this is a potentially powerful tool for performing mixing, or other relevant tasks in microfluidic systems. Vice versa, it is important to know how to avoid, or suppress, this effect when it is not desired.

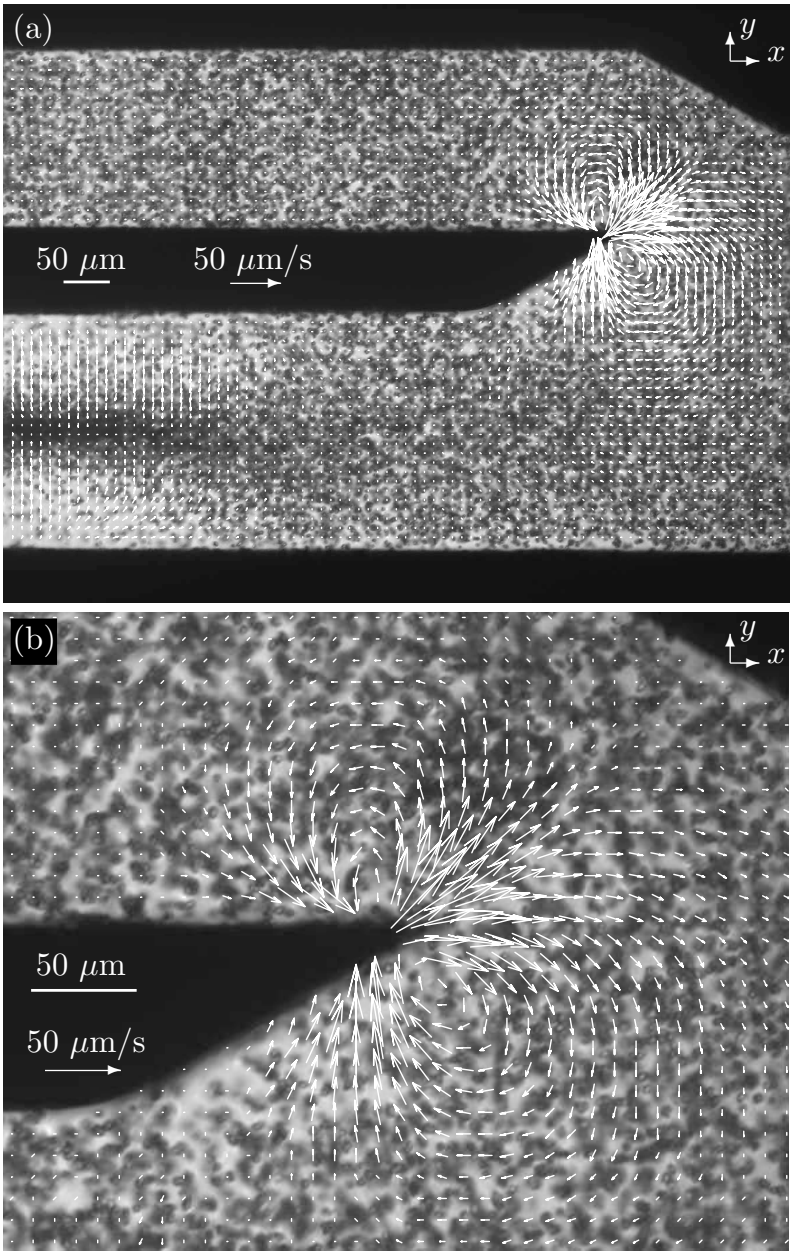

Figure 5.11: Velocity vectors calculated from particle motions in the split chip. The images are recorded at the second channel junction to the left in Fig. 5.9(a). The transducer is frequency matched to the bottom left channel in (a), but the highest velocity is recorded from acoustic streaming. (b) shows a closeup of the streaming pattern in the proximity of the wedge. The interrogation area used was 32×32 pixels with a 50% overlap. The velocity vectors are superimposed on top of the forming particle pattern after 8 seconds of actuation.

5.2.4 Acoustic streaming in circle chip

A number of acoustic test devices of various footprints were manufactured in the same batch process as the acoustic devices examined in Chap. 4. Here, one of these devices, consisting of a row of partly overlapping circles (400 μm in diameter), is presented. As for all devices in this batch, the depth of the *circle chip* was 200 μm throughout. When examined while in operation, the chip displays several interesting behaviors. One example is shown in Figs. 5.12 and 5.13, where the motion of 1 μm particles is measured at three different depths of the device. The transducer was frequency matched to the diameter of the circles (operating at 2.013 MHz) and the images were recorded in fluorescent mode using a 20$\times$ magnification objective (NA = 0.4). The presence of strong acoustic streaming in the proximity of wedges and corners was demonstrated in Sec. 5.2.3. The same effect could be seen at the wedges in the circle chip, for instance, in the middle, and to the right side of Fig. 5.13(b). However, the most interesting result displayed in Fig. 5.13 is the pronounced 3D nature of the flow, which becomes apparent when the direction of the velocity vectors in (a)–(c) are compared. In the top and the bottom of the channel, the flow direction is away from the central horizontal line. In contrast, the flow is directed towards the same in the middle of the channel. This flow behavior can be explained by the presence of four streaming rolls as shown in Fig. 5.12.

In this thesis, the focus has been primarily on the in-plane acoustic effects. The present example clearly shows that even if the 3D effects caused by acoustic streaming in many cases can be disregarded (in the case with microdevices utilizing the acoustic radiation force and large particles), they should not be neglected. In fact, when subject to screening for the presence of acoustic streaming, most microdevices examined in this study exhibit 3D streaming behavior for several frequencies. More in depth studies of 3D effects are of clear interest for the overall understanding of acoustic devices.

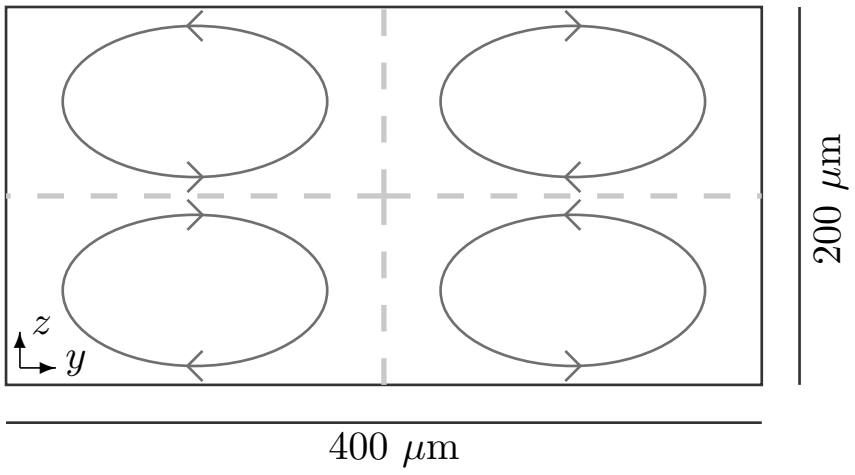

Figure 5.12: Sketch of the circle chip as seen from the side. The 2D measurements at different depths in Fig. 5.13 indicate the presence of four streaming rolls in the vertical direction of the channel.

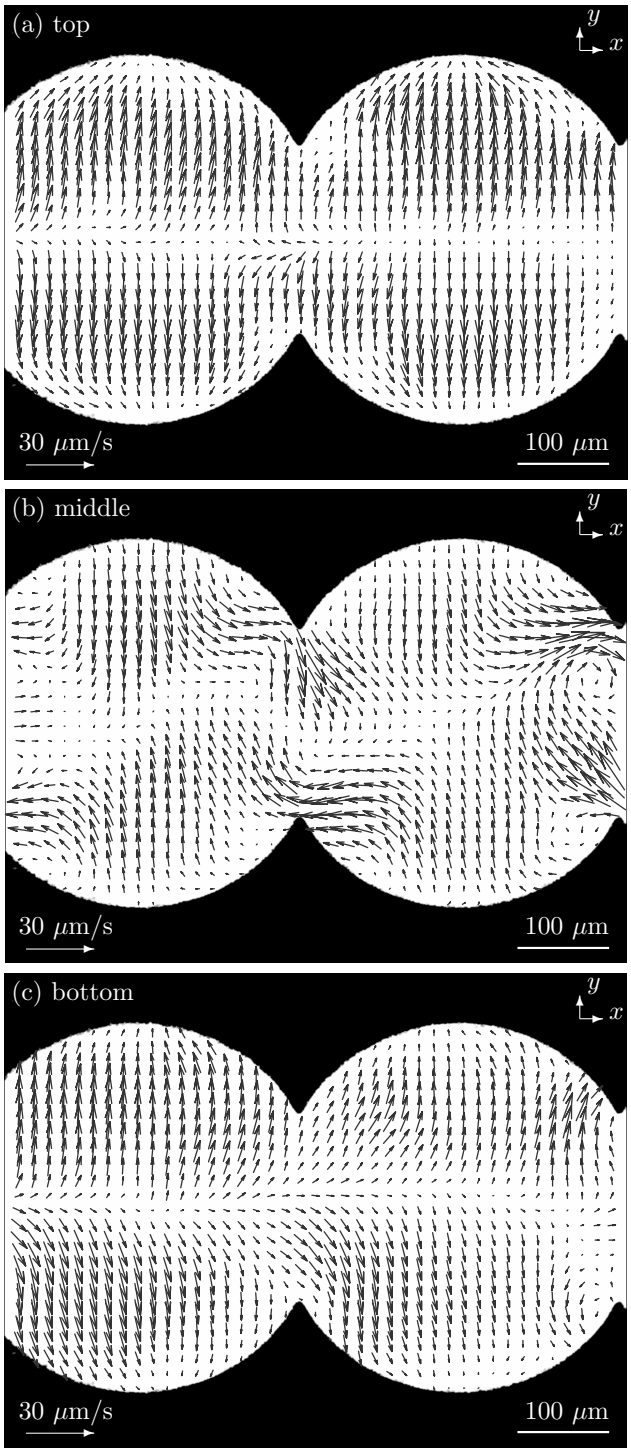

Figure 5.13: Circle chip acoustically actuated at 2.013 MHz. The motion of 1 μm particles is measured at (a) the top, (b) the middle and (c) the bottom of the microchip. The opposing directions of the velocity vectors at the different measurement depths clearly indicates the presence of 3D streaming motion.

Chapter 6

Stereoscopic micro-PIV

6.1 Introduction

The third major part of the PhD study was devoted to the development of a viewing configuration for stereoscopic micro-PIV, using mm-sized mirrors. The final outcome of this study was the paper [18], which is presented in Sec. 6.4. A short introduction to stereoscopic PIV is provided in Sec. 6.2. The paper [18] is also making several references to the Scheimpflug principle [73], and therefore, a presentation of this principle has been included in Sec. 6.3. A description of some of the underlaying work, including several illustrations, is found in Chap. 7. Supplementary material on fabrication is provided in Appendices C and E.

6.2 Stereoscopic PIV

With the stereoscopic PIV method it is possible to calculate a 3D velocity vector field from two 2D velocity fields of the same flow field, where the two 2D velocity fields are recorded at different angles. In order to perform the 3D evaluation a numerical model is required, which describes how objects in the measurement region are mapped onto the images recorded by the cameras. In principle, this mapping can be calculated if the physical conditions (such as the viewing angles, the distances between the cameras and the measurement region, magnification of lenses, etc) are known. However, such an approach is not practical, and in an experimental situation the calibration is performed by recording images of a calibration target inserted in the measurement region. The calibration target is marked with dots (typically positioned in a grid pattern) for mapping of the object coordinates (X and Y). The model parameters are obtained by comparing the known marker positions in the measurement region with their recorded positions (x and y) of their respective image on each camera. In this study, a so called direct linear transformed (DLT) has been used [87], where the perspective projection (for each view) is expressed by:

$$\begin{bmatrix} w_o x \\ w_o y \\ w_o \end{bmatrix} = \begin{bmatrix} a_{11} & a_{12} & a_{13} \\ a_{21} & a_{22} & a_{23} \\ a_{31} & a_{32} & a_{33} \end{bmatrix} \cdot \begin{bmatrix} w_i X \\ w_i Y \\ w_i \end{bmatrix} \tag{6.1}$$

where w_i and w_o are constants. The perspective projection maps a rectangle (the image recorded by the CCD) onto a general four-sided polygon. The mapping is then used to combine the two 2D velocity vector fields recorded from the separate angles, for instance by matching the nearest neighboring vectors. The velocity components for each vector in 3D (U, V and W) are found by solving

$$u_1 = U + V + W \tag{6.2a}$$
$$v_1 = U + V + W \tag{6.2b}$$
$$u_2 = U + V + W \tag{6.2c}$$
$$v_2 = U + V + W, \tag{6.2d}$$

where u_1, v_1, u_2 and v_2 are the known velocity components of the two 2D velocity vectors, respectively. The calibration implementation which has been used in this study is documented in the software manual for the program Flowmanager (Dantec Dynamics). Some more information on the calibration can also be found in Sec. 6.4.2.

6.3 The Scheimpflug principle

In the following description we consider a system consisting of a recording media (a CCD), an optical lens and a flat target. For each object, we imagine a straight line drawn through each object, thus, an image plane (CCD), a lens plane and an object plane (target) are introduced. In a camera, the lens plane and the image plane are normally positioned parallel to each other. If we view a flat target positioned in the object plane at an angle with respect to the normal of the object plane, only the central part of the target will be recorded in focus. This is a problem in stereoscopic PIV, because in order for the method to work the two views have to overlap (the same particles recorded by both cameras). The problem is circumvented by introducing a Scheimpflug correction [73], in practice by tilting the image plane with respect to the lens plane (see Fig. 6.1). The Scheimpflug condition is satisfied if,

$$\tan\alpha = \frac{F}{d - F} \tan\theta. \tag{6.3}$$

F is the focal length of the objective, θ is the displacement of the lens with respect to the normal of the object plane (given by the figure) and d is the distance between the center of the lens and the center of the calibration target. In Fig. 6.1, θ_1 and α_1 are drawn equal to θ_2 and α_2, although this is not a requirement of the method. The 2D description of the Scheimpflug principle is fully translatable into a 3D description.

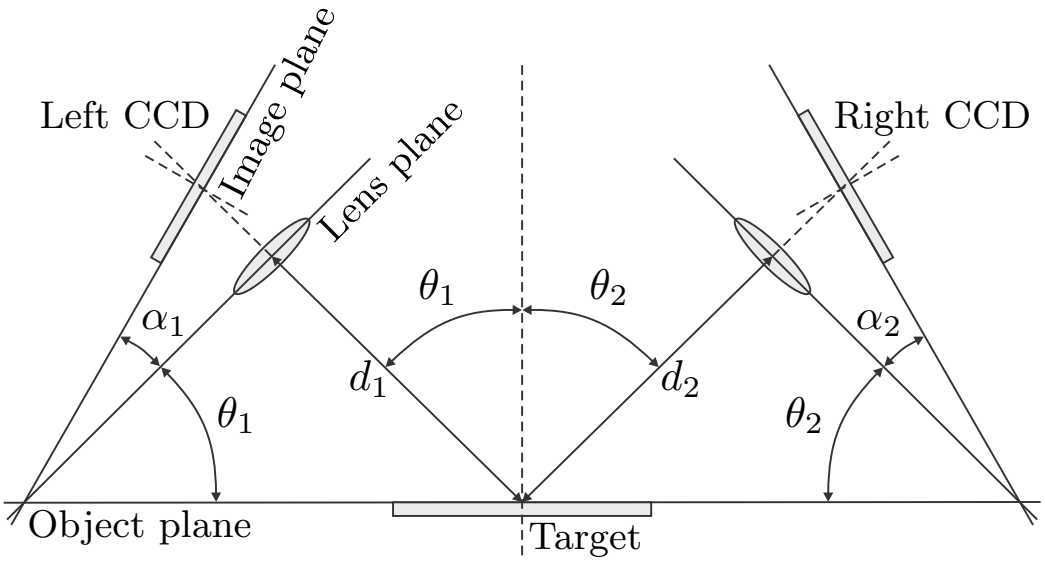

Figure 6.1: A demonstration of the Scheimpflug principle, here drawn for two cameras (mirrored at the normal of the object plane) as it is utilized in standard stereo-PIV. The same principle is, however, relevant in stereoscopic micro-PIV. The Scheimpflug criterion is fulfilled when all three planes (image, lens and object) intersect in a common point (line in 3D space), as drawn in the figure.

6.4 S. M. Hagsäter *et al.*, Exp. Fluids, 2008, 45, 1015–1021

beginning of paper

A compact viewing configuration for stereoscopic micro-PIV utilizing mm-sized mirrors

S. M. Hagsäter[1], C. H. Westergaard[2], H. Bruus[1], and J. P. Kutter[1]
[1] *Department of Micro- and Nanotechnology, DTU Nanotech Bldg. 345 east, Technical University of Denmark, DK-2800 Kgs. Lyngby, Denmark*
[2] *Vestas Wind Systems A/S, Frederiksborgvej 399, 4000 Roskilde, Denmark*

When applying PIV to micrometer-resolution systems, the out-of-plane velocity component has shown to be much more difficult to obtain than the two in-plane velocity components. In this work we present a novel stereoscopic viewing configuration, for stereoscopic micro-PIV, utilizing mm-sized mirrors introduced in front of the microscope objective lens. Attractive applications, where the advantage of the mirror viewing configuration system could be utilized, include (on-chip) miniaturization and the potential to introduce more than two simultaneous viewing angles. Here, a first validation of our system is presented including stereoscopic micro-PIV measurements in a micro-fabricated test device.

6.4.1 Introduction

In microfluidic systems the limited optical access poses restrictions to flow velocity measurements. With the micro-PIV technique [8] the two in-plane velocity components can readily be obtained due to the combination of volumetric illumination and focal suppression [9]. However, in many microfluidic scenarios the objective is to quantify a flow of three-dimensional nature, and it is therefore desirable to measure all three velocity components.

In standard PIV, stereoscopic methods have been used for many years by aiming two individual cameras onto the same planar light sheet either with lateral displacement (object plane, lens plane and image plane remain parallel; no distortion is introduced) or angular displacement (the image plane must be tilted according to the Scheimpflug condition [73] in order to maintain focus in the object plane; perspective distortion is introduced) [75, 76]. Angular displacement is the most widely used, since one gains better focusing with normal optics at large viewing angles. The viewing angle between the cameras is best at $2\times45°$, because with a right angle the measurement resolution will be the same in all directions. Due to practical limitations, smaller angles are often used, but nevertheless these angles are still relatively large. An alternative solution utilizing lateral displacement was presented by [77]. In their system, a set of mirrors was used to create stereoscopic views, and a single camera was used to record image frames.

Scaling the standard stereo PIV setup down to accommodate microfluidic applications poses the challenges of utilizing volumetric illumination (just as in ordinary micro-PIV), and finding physical room for large aperture light collecting lenses sufficiently close to the microfluidic device, while maintaining a sufficiently large angle between the views. An apparent straightforward solution would be to utilize a stereo microscope. These can be found in two different types: the common main objective type (CMO), which utilizes lateral displacement, and the Greenough type, which basically utilizes angular displacement (the optics are adapted for microscopy eye-viewing purpose, so there is no Scheimpflug correction). The main benefits with the Greenough configuration are the high numerical aperture and the high optical resolution. The main advantages with the more popular CMO configuration are that there is no perspective distortion and that infinity optics are used. The main drawbacks with the CMO configuration are the need for a large front lens and the limited optical magnification readily available.

However, the main limitation of stereoscopic micro-PIV realizations using standard stereo microscopes is in particular the angle between the views, since these microscopes are adapted to the human requirement of a convergence angle of around 10° to 12°. This poses a limitation with respect to the resolution of the out-of-plane velocity components. Successful applications of stereo micro-PIV using stereo microscopes can be found in [78], [79] and [80]. An alternative method is demonstrated by [81]. Here, by using the translation method in an ordinary microscope, the 3D flow velocities are obtained by recombining two view angles from a "fly-over" performed in a cartographic manner.

There are also examples of other non-stereoscopic particle-based velocimetry techniques, with which it is feasible to derive the out-of-plane flow components in microfluidic systems. Some recent publications include: deconvolution microscopy [82], holographic

methods [83], optically sliced methods [84], and continuity based techniques [85]. However, the working principles and validation of these methods will not be subject to further discussion in this manuscript.

In the stereoscopic micro-PIV realization presented in this paper, the single optical path of an upright research microscope is utilized. The two respective inclined views are achieved by placing a set of mm-sized mirrors (coated glass prisms) between the sample to be investigated and the microscope objective front lens. One advantage of this setup is the high level of adaptability that it provides. For instance, the angle between the views can be made larger than what is typically given by a stereo microscope lens, which is a limiting factor for the accuracy of the stereoscopic micro-PIV method.

An additional benefit is the potential to include the splitter mirror system directly in contact with or as a part of the microfluidic system [86]. This would allow routine inspections to be performed at defined positions, using a standard microscope. Such a system would greatly benefit from miniaturized mirror sets, allowing for higher magnification objectives to be used. Alternatively to the previous solution, the splitter system could be integrated with the front lens of the microscope objective. Such a configuration would allow free in-plane translational movement of the substrate, thus, readily allowing multiple points of inspection. Other benefits would be the simpler handling, including no requirement for pre-alignment of the mirrors, less clutter of workspace and the ability to perform faster calibrations. Finally, by expanding the same principal design, a mirror system allowing more than two views is feasible. Such a system could be utilized in a first realization of tomographic micro-PIV.

The potential of a viewing configuration utilizing mm-sized mirrors is demonstrated in two experimental setups. First, by an in-air example where the displacement of immobilized micro-particles is measured. And, secondly, through an investigation of the flow over a step in a microfluidic channel.

6.4.2 Materials and methods

Experimental setup

The central component of the experimental setup used in this study is the mirroring system, placed between the front lens of the microscope objective and the sample. It consists of three custom-made glass prisms with reflecting coatings that are aligned with respect to each other, as shown in Fig. 6.2. With this arrangement, two separate views from different angles will be obtained. To facilitate the alignment of the mirrors a special holder was designed (see Fig. 6.3), in which the central prism is held in place above a 6×6 mm square hole in the 2 mm thick holder substrate. The two side prisms are positioned in the 10 mm wide carved tracks extending horizontally from the central prism. The holder was in turn placed onto a 2 mm thick lever (not shown here), extending from a translational stage, which allowed the mirror system to be fine-positioned between the microscope objective and the sample.

Images were recorded with a HiSense MkII CCD camera (Dantec Dynamics), mounted with a 0.63× TV-adapter on a research microscope (Leica DMLB). The mirror system was

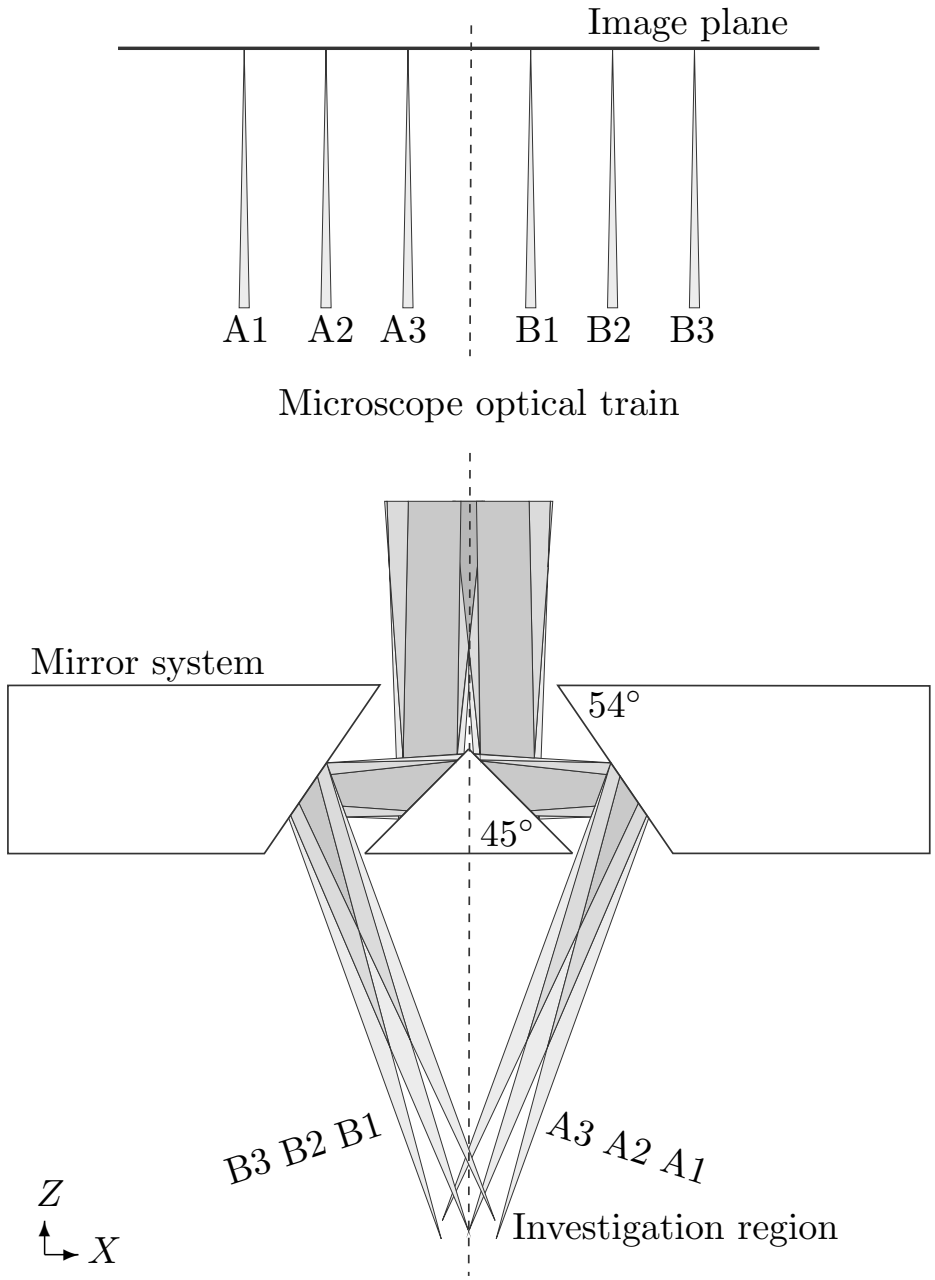

Figure 6.2: Ray-tracing through the mirroring system used in the experiments. The height of the central prism is 1.5 mm providing a top angle of 90°, whereas the side mirrors are designed with a 54° degree angle, as shown in the figure. The ray-bundles A1–A3 and B1–B3 show how the inclined views in the investigation region will be positioned in relation to each other at the image plane (as viewed by the CCD). Note that the ray-paths cross over in the microscope.

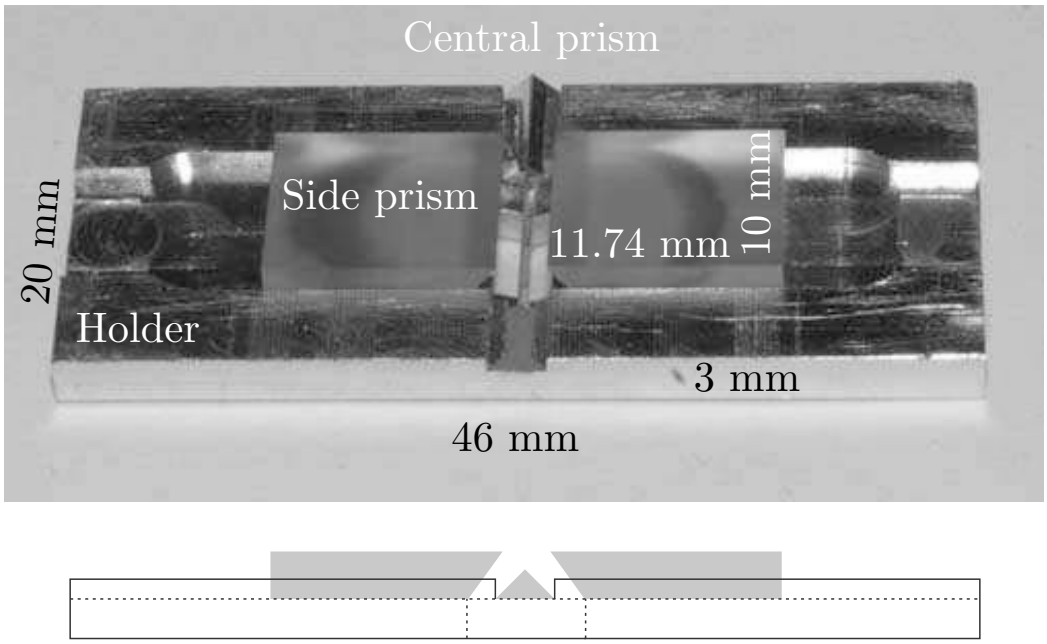

Figure 6.3: Top panel shows a picture of the holder with the prisms inserted. The central prism, 20 mm wide, is fixed in position in the middle of the holder. The side prisms, 10 mm wide, can be moved back and forth along the 10 mm wide and 1 mm deep tracks. There is a square hole (6×6 mm) in the center of the holder, which, in the figure, is covered by the mirrors. Bottom panel shows a sketch of the arrangement as seen from the side.

designed to be used with a 5× magnification objective (N Plan, Leica), with a numerical aperture, NA, of 0.12. With this combination, the total magnification was 3.15×, providing a field of view of 2.1×2.8 mm.

The samples were illuminated from below by two light emitting diodes (Luxeon Star 3W, Lumileds), mounted with plastic focusing lenses (FFLI, Fraen Srl) [15]. The LEDs were controlled by a PIV timing system (Dantec Dynamics) and powered by an in-house built power supply, allowing the light pulses to be synchronized individually with the camera. The diodes were positioned manually with the tip of the lenses ∼25 mm apart, and at a distance ∼35 mm below the level of the microscope's translational stage. When fluorescent signal was recorded, a short pass filter (500 nm, Thorlabs), was positioned between the LEDs and the microfluidic chip, and an I3 filter cube (Leica) was inserted in the filter turret. In the flow measurements, green fluorescent polystyrene particles (5 μm diameter, Duke Scientific), were used to trace the flow. For the in-air measurements, the same 5 μm polystyrene beads were immobilized in epoxy resin, and spread out in a thin layer onto a glass wafer.

The calibration targets were defined through UV-lithography of positive photo-resist spun on top of a 500 μm thick pyrex glass wafer. They consisted of 5×11 dots, 100 μm wide, equally spaced 200 μm center-to-center. An origin was defined by making the centermost

dot larger (150 μm wide), and enclosing it with four smaller dots (75 μm wide). The same type of target was used for both the in-air measurements and the micro-chip flow measurements.

The flow measurements were performed in a microfluidic chip, consisting of a rectangular channel manufactured through welding of glass pieces (channel dimensions 1×14× 48 mm). The ridge (dimensions 0.5×14×10 mm) and the target (height ∼700 μm) were positioned manually into the channel, which afterwards was sealed with a ∼140 μm thick glass lid.

The image acquisitions, image manipulations, 3D-calibrations and calculations were all performed on a PC with Flowmanager software (Dantec Dynamics).

Stereoscopic calibration and the "no Scheimpflug" condition

For the measurements presented in this paper, the stereoscopic calibration was performed in the same way as in a macroscopic PIV system using a calibration target and a translation stage, taking pictures at five different levels of depth. For these initial studies a direct linear transform as explained in [87] was used for the mapping between the investigation region and the image plane (CCD). The implementation is documented in the software manual for the program Flowmanager (Dantec Dynamics). An example of a recorded image frame, showing the calibration target from the two respective views (at $Z = 0$) is shown in Fig. 6.4 (see figure caption for additional information). As shown in the figure, the two views are recorded onto the same image frame.

For the in-air calibrations, the calibration target was traversed step-wise in the vertical direction, from -100 μm to 100 μm. To achieve a correct calibration in water, the calibration target's position inside the microchannel should be adjusted. This is to account for the difference in refractive index between water and air. However, this approach was not feasible using the current test structure, where the calibration target was locked in its position. Instead, the calibration was performed in a similar way as for the in-air calibration, but here the whole microchip (filled with water) was traversed step-wise between Z values of -100 μm to 100 μm. This gives an adequately correct calibration in the X and Y directions, but the Z direction is wrong by the depth magnification in water. This was compensated for in the software by multiplying the actual vertical displacements with the refractive index of water (1.33), corresponding to step-wise displacements of +/-133 μm, as if the target had been moved inside the water filled channel. This was found to be a sufficient enough approach for this first feasibility study of our stereoscopic viewing configuration, but since this calibration method has clear limitations as to its applicability for the investigation of lab-on-a-chip systems, other calibrations methods (such as presented in [88]) are generally recommended. The splitting mirror system was held in a fixed position with respect to the microscope objective, and the target plate was moved with the microscope's focusing translation stage. The central calibration position ($Z = 0$) was chosen so that the middle column of dots on the calibration target was in focus in both views.

When the target is traversed in the vertical direction, the dots' in-plane positions are shifted (in the image plane). For the in-air measurements, a movement of 6.75 μm in Z

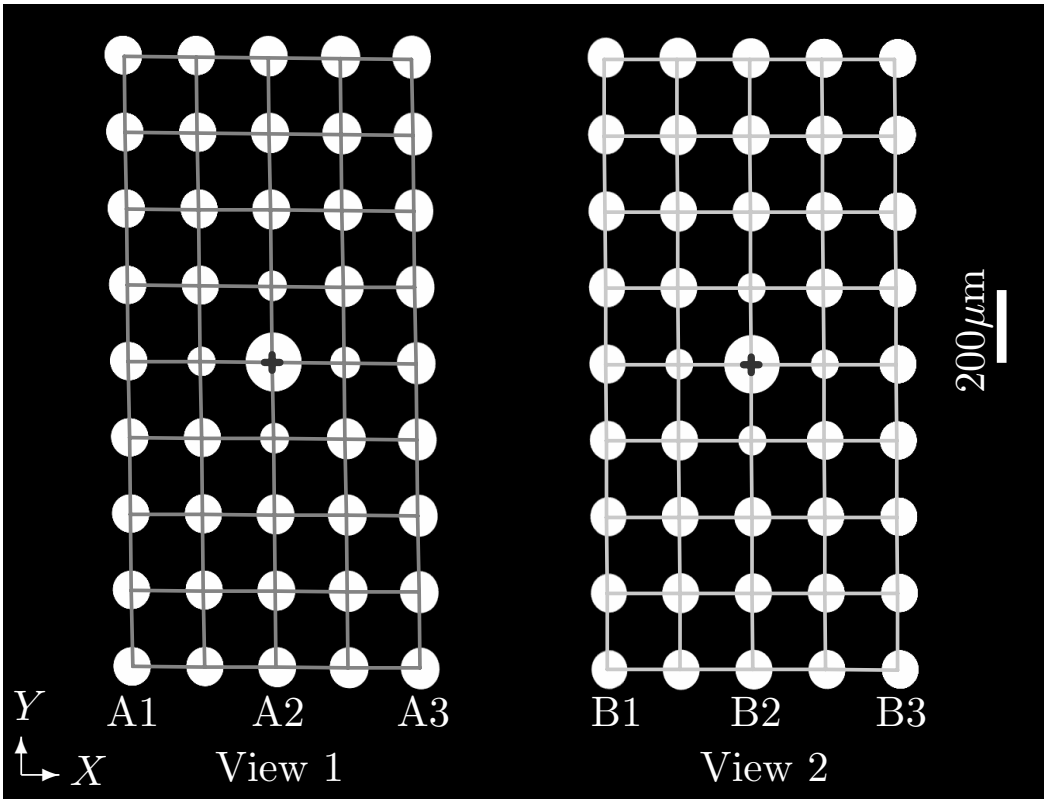

Figure 6.4: Recorded image frame (transformed into a binary image by contrast enhancement) showing the calibration target from the two respective angular views. A1–A3 and B1–B3 correspond to the same notations as in the cross-sectional view in Fig. 6.2. Grid-nets showing the linear transform are superimposed on top of the dots (view 1, dark gray and view 2, bright gray) and the common origin is indicated by the '+'-marks.

was found to result in a one pixel in-plane displacement. Since the in-plane resolution is 2.0 μm per pixel, this corresponds to a depth resolution of roughly 1/3 of the in-plane resolution, or an angle between the views of $\sim$34°. For the measurements in the microchip, the calibration was performed similarly, with a movement of 8.9 μm in Z resulting in a one pixel in-plane displacement. Due to the air-glass-water transition, here the angle between the two views was found to be $\sim$26°, which corresponds to a depth resolution of about 1/4 of the in-plane resolution.

In a classical setup, where two cameras are used for recording stereoscopic views, the Scheimpflug condition [73] can be satisfied by tilting the cameras' image planes (the CCDs) according to the object plane. However, the stereoscopic viewing configuration described here has not yet been accommodated to include multiple CCDs; so far, only a single CCD has been used. Thus, with respect to a flat target, or a common measurement plane, the two focus planes will be tilted according to the viewing angles (see Fig. 6.5). This is a clear limitation of the current setup, but not a drawback of the single optical

path configurations as such, and suggestions on designs that circumvent this limitation are discussed further below.

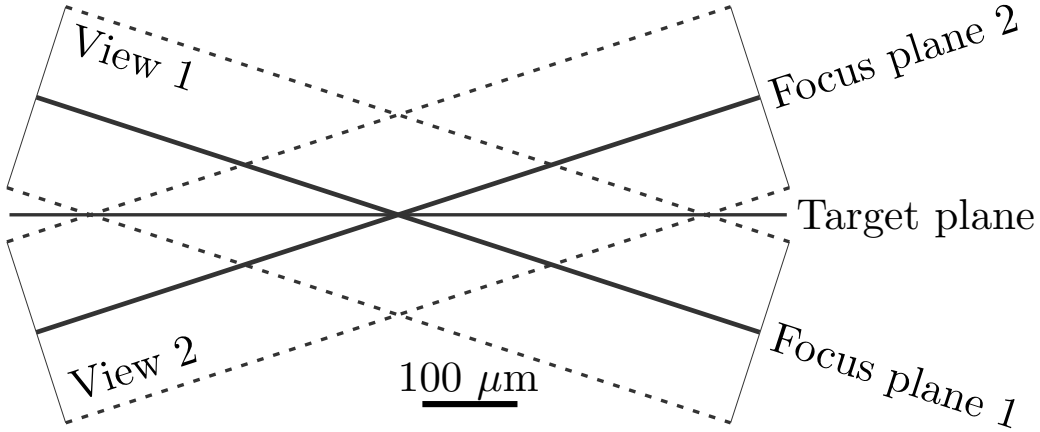

Figure 6.5: A cross-sectional view of how the focus planes are located for the two respective angular views. In the figure, the displacement of the focus planes with respect to the target plane, +/–17°, is given for inspection in air using the current setup. The depth of focus is indicated by the dashed lines, here drawn with a +/–100 μm separation from the focus planes.

6.4.3 Results

Displacement measurements conducted in air

As a first validation of the method, displacement measurements of immobilized particles (conducted in air) were performed. For this experiment, the 5 μm polystyrene beads were mixed with epoxy resin, and thereafter spread out in a thin layer onto a diced pyrex glass wafer of the same thickness as the calibration target. Double-image frames were composed from single frames, where the microscope's translational stage was used to displace the particles (in one of the directions, X, Y or Z) between the two recordings. The results from these displacement measurements are seen in Fig. 6.6. Qualitatively, no displacement in Z is measured for translations in-plane, and, contrariwise, no in-plane displacements are measured for the translation in Z. This is the most important result of this experiment, as it shows that the proposed stereoscopic micro-PIV approach is capable of separating displacements in three dimensions. Due to the fact that all the particles are located within a thin sheet, and given the relatively large depth of focus of the system, homogeneous displacements are measured for a fairly large part of the image field (+/–150 μm in-plane from the intersection). However, for larger distances from the intersection, due to the lack of overlap between the two views, the displacements could not be quantified.

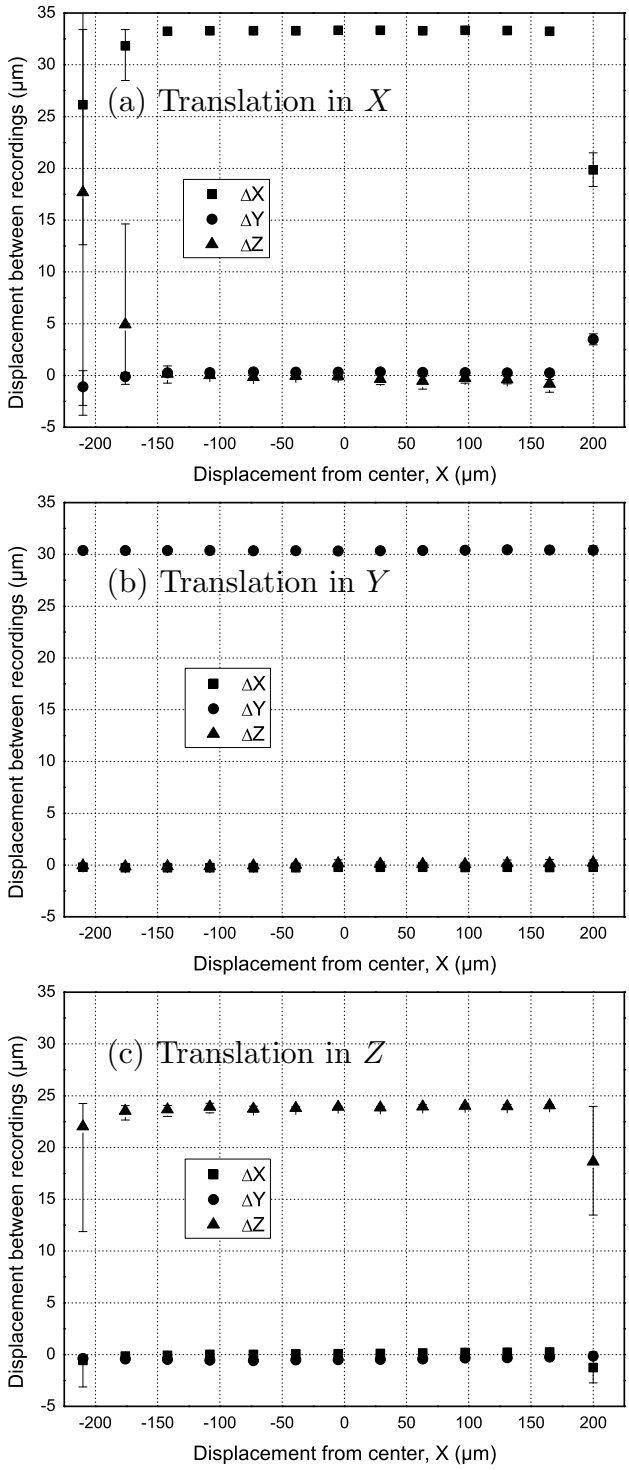

Figure 6.6: The measured displacement of translations (a) ∼33 μm in X, (b) ∼30 μm in Y and (c) ∼24 μm in Z, respectively. The interrogation area used was 64×64 pixels, with a 75×50% overlap. Displayed is the average of the 10 middle vectors for each column, with error bars showing the min and max values within each data set. For larger displacements from the center, due to the no Scheimpflug condition, there is not enough overlap between the two views to produce valid vectors.

Measurement of flow over a micro-step

In the next experiment, the flow over an upwards step in a micro-channel was measured. Here, the addition of volume illumination further restrains the workable measurement region of the current one-CCD system. Nonetheless, we are able to obtain valid 3D velocity data in a common region around the center, where the focus planes for the two views have a large overlap (as was shown in Fig. 6.5). The system was calibrated with the calibration target positioned inside the micro-channel (which was filled with water during the calibration) and thereafter, the stage was traversed (15 mm) in-plane to the position of the step. Measurements were performed in three partly overlapping positions: directly over the step, and approximately +/–1 mm upstream and downstream with respect to the middle position, as shown in Figs. 6.7(a–c). All three measurements were performed in the center of the channel (total width 14 mm) in consecutive order. For measurements in water, with 5 μm particles, the depth of correlation [10] is about 200 μm. Double image frames with a time separation of 30 ms were recorded in fluorescent mode [15] using LED illumination pulses of 2 ms. Velocity vectors were calculated using adaptive correlation with an interrogation area of 64×64 and an overlap of 50%. For each position 100 double images were used for averaging.

The measured velocity V was ∼125 μm/s upstream and ∼300 μm/s downstream of the step. The out of plane velocity W was close to zero, except for just before the step, where the measurement indicated the presence of an upward flow (see Fig. 6.7(b)). Finally, the velocity U, perpendicular to the main flow direction V was close to zero through the investigated region. The measured velocities were validated by comparison with calculated velocities for a 2D-cross sectional model, using COMSOL finite element method software (displayed as lines in Fig. 6.7). This comparison showed a good agreement between the two.

Discussion

With the two experimental test examples, we have demonstrated the capability of the stereoscopic viewing configuration for reliable 3D velocity measurements. In the current realization a magnification of 3.15× was used, corresponding to a total field of view of two times 2.1×1.4 mm. In practice, however, because the current realization does not fulfill the Scheimpflug condition, the measurements were limited to be performed in the vicinity of the common optical axis only. Nonetheless, this should not be interpreted as a general limitation of the single optical axis stereo viewing principle as such. By adjusting the angles and the position of the mirrors it is possible to create a larger separation between the views in the image plane, which in turn would allow the views to be captured by individual CCDs. Alternatively, the two views could be separated perpendicularly to the microscope's principal axis by fitting additional splitting mirrors in the optical train, after the tube lens (more complex solutions including glass materials or lenses could also be imagined). However, these further developments towards a more complete system are beyond the scope of this study, where the main focus has been on the components placed in between the sample of investigation and the microscope's objective.

Another line of investigation for the future would be to shrink the mirror setup to

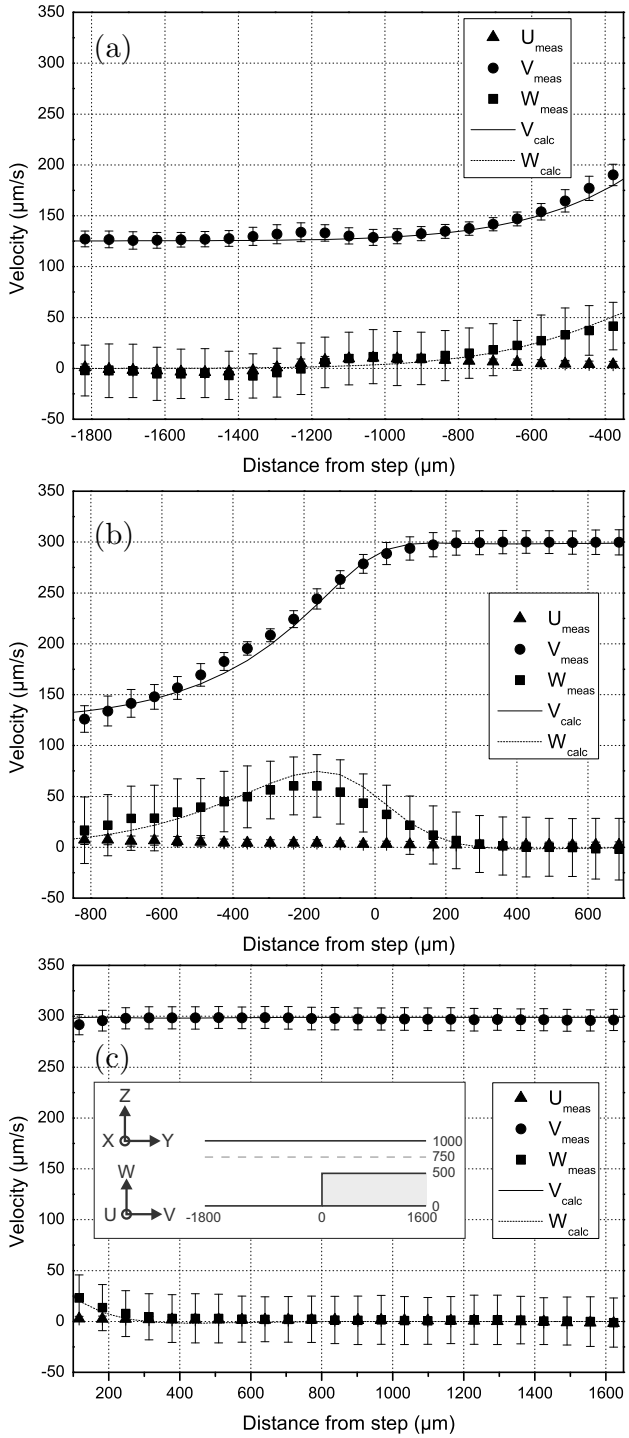

Figure 6.7: Measured (dots) and calculated (lines) velocities of the flow (a) upstream, (b) above, and (c) downstream of a step in a micro-channel. The error-bars are showing the standard-deviation, which, as expected from the angle between the views being smaller than 45°, is larger for the in-depth velocity component W than for the in-plane velocity components U and V. The calculated velocities are displayed for a height of 750 μm from the model's bottom boundary wall. This depth was chosen to fit with the measured velocity V.

fit to higher magnification systems. With the current realization, it should be possible to make a model to fit to, at least, a 10× magnification, though it would require some modifications with respect to the alignment and handling of the system. Naturally, the increased resolution by itself would be an improvement, but the true objective would be to investigate how to incorporate stereoscopic viewing ability during the fabrication or packaging of micro-devices, utilizing the same stereoscopic viewing principle as proposed in this manuscript. This would allow routine inspection to be performed at defined positions, using a standard microscope. An alternative for future studies would be to inquire into an integration of the splitter system directly with the front lens of the microscope objective. Such a configuration would facilitate handling, and would be practical for multiple points of inspection, or scanning, experiments. A final suggestion for future applications would be to expand the same principal design to include more than two views. Such a system could then be utilized as a first realization of tomographic micro-PIV.

It should also be mentioned that there are other ways in which our system could be improved, more related to the implementation of the stereoscopic micro-PIV method. For instance, one way to increase the accuracy is by introducing a pre-processing procedure to remove invalid particles, i.e., particles that are only appearing (in focus) in one of the views [80]. Furthermore, the calibration procedure used in this study is not practical for most microfluidic applications, but there are examples of other calibration procedures, which we propose to implement [88].

6.4.4 Conclusions

We have successfully demonstrated the functionality of the optical setup and shown that reliable result can be obtained. The current system still has a number of shortcomings, where first and foremost the system does not fulfill the Scheimpflug condition. However, we have several suggestions on how to engineer a solution to this limitation. Other potential improvements include mirrors designed to be used with higher magnification objectives, further increase of the angle between the views and realizations with stereoscopic viewing incorporated on-chip.

Acknowledgement

SMH was supported through Copenhagen Graduate School for Nanoscience and Nanotechnology, in a collaboration between Dantec Dynamics A/S and DTU Nanotech, the Department of Micro- and Nanotechnology.

end of paper

Chapter 7

Additional material on stereoscopic micro-PIV

This chapter features additional material on the stereoscopic micro-PIV realization, that was presented in Chap. 6. This includes relevant information about the design process of the mirror system. Several illustrations showing the materials and equipments that were used in this study are also supplied, since the manuscript format of the previous chapter did not allow to go into more detail. Finally, the suggestions for improvements and further developments mentioned in Sec. 6.4.3 and Sec. 6.4.4 are repeated and expanded.

7.1 Initial studies

The stereoscopic viewing project was initialized by a study exploring the possibility to incorporate slanted mirrors in microdevices. The idea was to investigate if such configurations could be used to obtain side views of the flow inside microdevices, in addition to the top views. Such recordings would be of interest for devices where the most dominant, or interesting, features of the flow are in the top/bottom direction. Several initial experiments were performed, similar to the one presented here. In this particular example, a thin glass capillary with a rectangular cross-section, 30 μm$\times$300 μm (VitroCom), was used (see Fig. 7.1). The capillary was put in close proximity to a mirror (i.e., a diced polished silicon wafer), which was positioned at a 45° angle as shown in the insert in Fig. 7.1. The capillary and the mirror were thereafter placed under the microscope. As we can see in the figure, with this setup it is possible to record images of the capillary as seen from both the top (a) and the side (b). However, with this configuration it is not possible to get both of the views in focus at the same time, since the optical path is longer for the side view (as seen in the insert in Fig. 7.1). There are different configurations (not shown here) through which it is possible to control the optical path lengths, and, thus, allowing simultaneous recording with a 90° angle between the views. However, such solutions require several mirrors, which makes them difficult to incorporate on-chip. Further efforts in this direction were therefore abandoned. Instead, the idea of developing a stereoscopic viewing configuration emerged, where the experience that had been gained from constructing and

working with small mirror systems could be utilized.

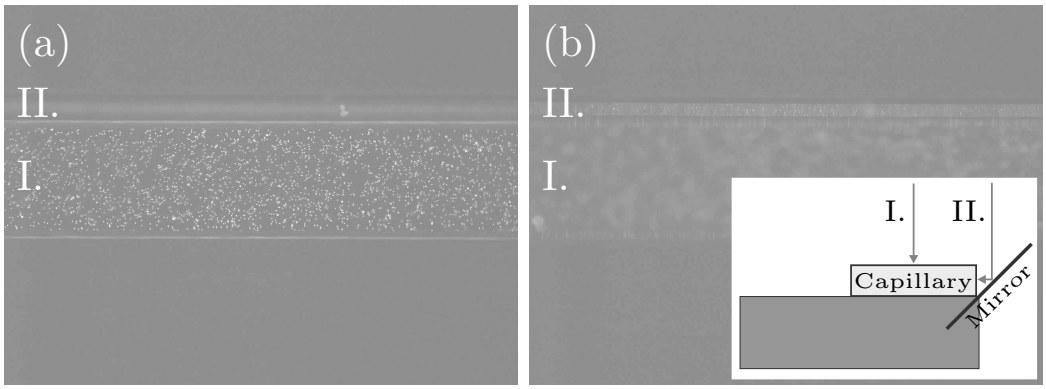

Figure 7.1: Recorded image frames of fluorescent particles inside a thin glass capillary. Due to the arrangement with the mirror it is possible to record both a top view and a side view of the capillary simultaneously. However, since the optical path length is longer for the side view than for the top view (see the arrows in the infold), it is not possible to have both of the views in focus at the same time. (a) Top view in focus. (b) Side view in focus.

7.2 First stereoscopic viewing configuration

7.2.1 Design

The first mirror prototypes were built using diced silicon wafers, glued onto blocks and rods sawn out from polymethyl methacrylate (PMMA) substrate, which were used as support. It was not trivial to assemble these components with high precision, especially cutting out the thin triangle-shaped rod used as support for the central mirror. From a design perspective, the mirrors made from silicon substrate were also unsuitable, since the thickness of the wafers prevented making the top of the central mirror sharp. The truncated angle is limiting the usable field of view of the setup. In addition, silicon is a fairly poor reflector and in the visible spectrum only about 50% of the incident light is reflected. All in all, in order to create a workable stereoscopic viewing configuration, it was evident that mirrors composed in some other way were required. Standard mirrors with the desired properties and the small size required by the application were not available from the main manufacturers. However, the author was fortunate to get recommended to a company (Union Optic Inc.) that fabricates custom made optical components at an affordable price. The first set of mirrors that was ordered, is seen in Figs. 7.2(a–c). The dimensions and angles of these first prisms were found using CorelDRAW software as a design tool.

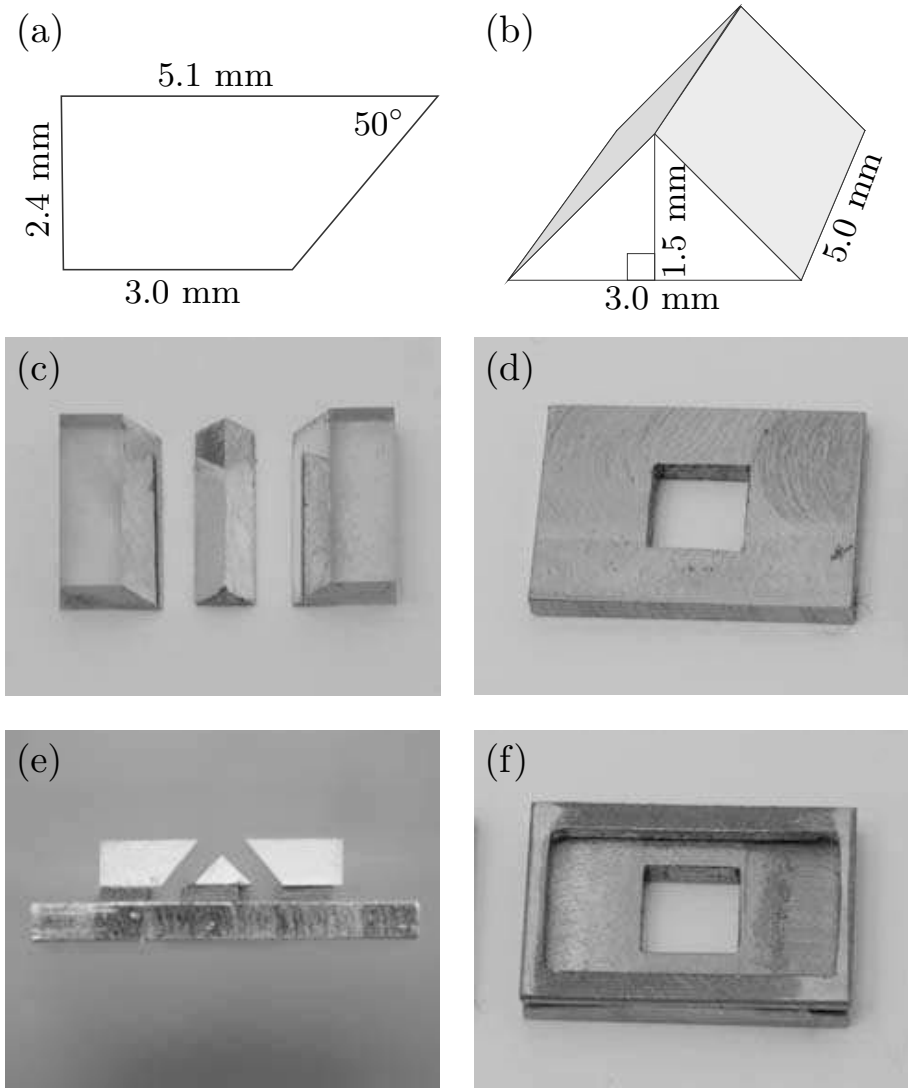

Figure 7.2: The first stereoscopic viewing configuration. (a) Sketch of side prism. (b) Sketch of central prism. (c) Photograph of the prisms. Note that the side mirrors are upside down. (d) The holder for the mirrors. (e) The prisms positioned on the holder as seen from the side. Pieces of magnetic tape (thickness 1 mm) are used to hold the mirrors in place. (f) The holder equipped with a supporting frame.

7.2.2 Experimental setup and results

In this configuration, the prisms were positioned on top of a holder (seen in Fig. 7.2(d)) manufactured in high-grade steel. Pieces of magnetic tape were attached to the bottom of the prisms. With this arrangement, the magnetic force held the prisms in place on the holder, but their positions could still be adjusted. The tape is visible in the side view in

Fig. 7.2(e). The holder was placed in an elevated position, a few mm above the sample that was to be investigated (i.e., a microfluidic device), with the help of PMMA blocks. With this setup it was possible to record high quality images, as displayed in Fig. 7.3. In the figure, a stereoscopic view of three rings, laser ablated in a polymer substrate, is shown.

However, very small displacements of the mirrors had a large impact on the functioning of the setup, and the alignment of the mirrors was both delicate and time consuming. Therefore, another approach was tested, where the magnetic tape was abandoned and the holder was supplied with a frame (see Fig. 7.2(f)). This configuration did make it easier to control the distance between the prisms. However, the desired angles between the mirrors (ideally they should be placed parallel to each other) were still difficult to obtain. Another practical challenge of the first setup was the way in which the holder was positioned with the PMMA blocks placed directly on the microdivice. Finally, a technical problem arose in that the mirror coating did not stick very well to the glass-prisms, and after some time of usage it started to come off. In the following Sec. 7.3 the solutions to these problems are presented.

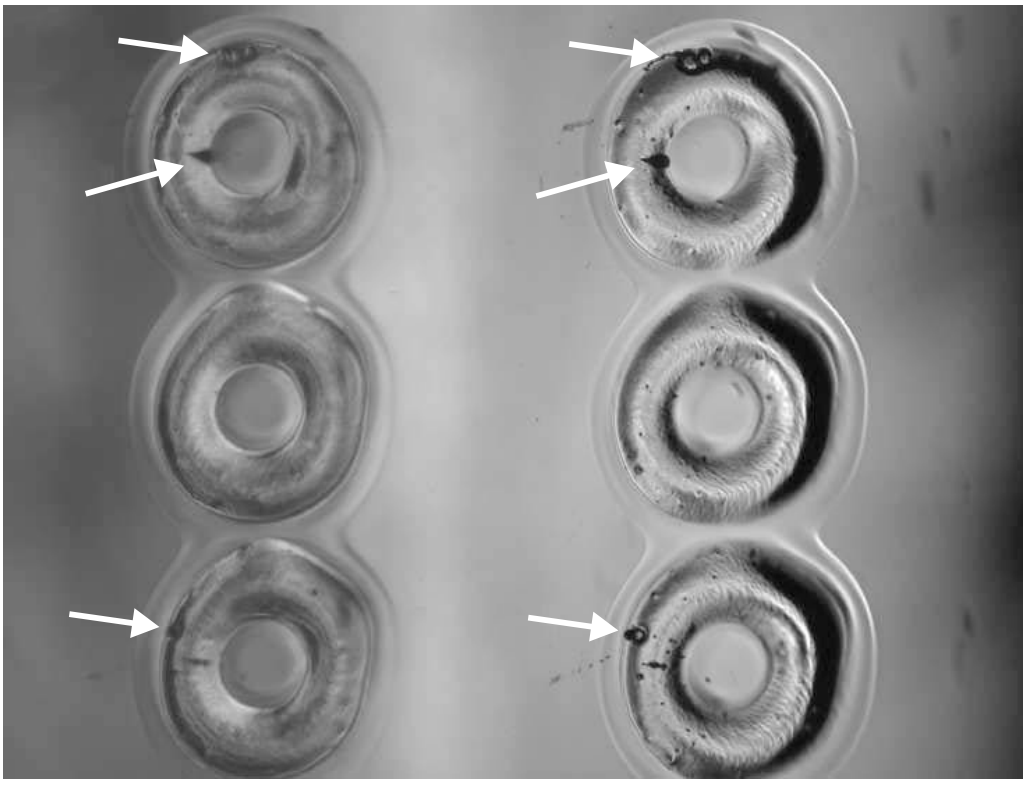

Figure 7.3: Image frame showing stereoscopic views of three rings patterned in a polymer substrate. The arrows are pointing at some common features.

7.3 Second stereoscopic viewing configuration

The stereoscopic viewing configuration and the experimental setup presented in this section are the ones that were used in the measurements presented in Chap. 6. This was the last design that was assembled and evaluated experimentally during the course of this study.

7.3.1 Design – ray-tracing

For a person who is not an optics expert it can be difficult to comprehend the details of the optical pathways and the image formation in a microscope, since the "image" is inverted and displaced in the optical train. This understanding is not achieved more easily after the addition of a mirror system placed in front of the microscope's objective. In order to examine the effects resulting from changing the angles, the positions and the separation between the mirrors, ray-tracing (using Raytrace, IME software) was therefore applied in the design process (see Fig. 7.4). In essence, a full 2D-model of the microscope's optical train and the mirrors of the stereoscopic viewing configuration were assembled in the program. This model made it possible to trace rays from the object plane to the image plane, and vice versa. The first stereoscopic viewing configuration was also used to investigate some of the results obtained from the model experimentally. Some concepts that are important for the (optical) design of the stereoscopic viewing configuration are discussed below.

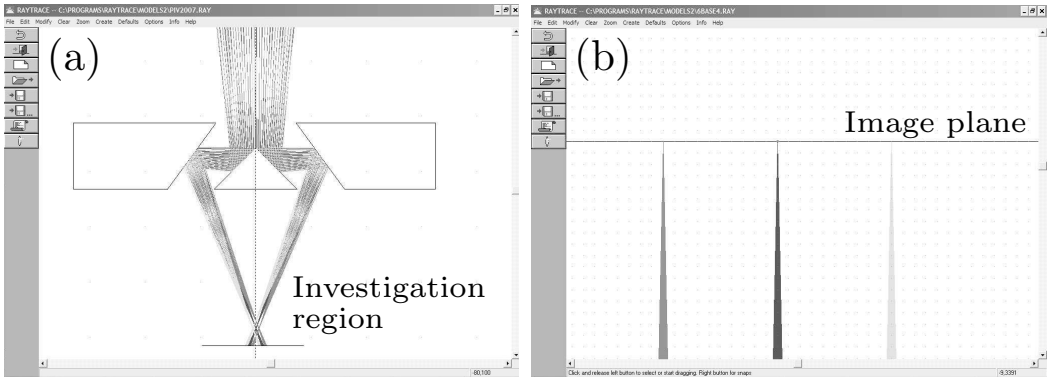

Figure 7.4: 2D ray-tracing through the microscope and the mirror system from the image plane to the investigation region. (a) A closeup showing the mirrors and the investigation region. (b) A closeup at the image plane, showing the origin of three ray-bundles.

Free working distance of the microscope's objective

The free working distance of the microscope's objective (the distance between the tip of the objective and the sample) needs to be substantially large, so that there is enough room to introduce the mirror system. Remember that the light path is bent inside the mirror system, so with the mirrors inserted the microscope's objective will need to be closer

than normal to the sample. This can be a problem with the method, especially for high magnification objectives, which typically are placed very close to the sample. However, for the 5× microscope objective used in this study the free working distance was 14 mm, and it was not a limiting factor of the current realization.

Overlap between the views in the investigation region

If the top angle of the central prisms is fixed at 90°, the angle of the side mirrors will determine the angle between the views of the stereoscopic viewing configuration. The mirror system has to be adjusted, according to the angle of the side mirrors, so that both views are aligned to observe the same investigation region. This is done by adjusting the height of the whole mirror system in relation to the sample, and by moving the side prisms closer or further away from the central prism. The elevation of the mirrors with respect to the sample increases with smaller angles between the views. Therefore, the free working distance will at some point pose a limitation as to which viewing angles can be engineered. Fortunately, this is not a major problem because a large angle between the views is typically desired.

Separation between the views in the image plane

It is not sufficient that the two views overlap in the investigation region, but the mirror system also has to achieve a separation between the views in the image plane. For a certain angle of the side mirrors, position of the mirror system and distance between the side prisms and the central prisms, there will be a total overlap of the two views in the image plane (as in Fig. 7.4(b)). In Fig. 6.2, a separation of the views has been achieved by moving the mirror system 0.5 mm upward in the Z-direction and the side prisms 0.25 mm closer to the central prism (compared to the system in Fig. 7.4). These changes do not affect the viewing angle, and the overlap between the views in the investigation region is maintained.

7.3.2 Materials

For the second stereoscopic viewing configuration, apart from the changed angle of the side mirrors, other modifications were made to improve the experimental setup. The new prisms and the new holder are seen in Fig. 7.5. The central prism was made longer (20 mm), so that it could be locked in position at the center of the holder. The alignment of the side prisms was made easier by the introduction of grooves of matching width extending perpendicular to the central prism. The side prisms were also enlarged to facilitate their parallelization with respect to the central mirror.

Changes were also made to the setup, which can be seen in Fig. 7.6. The greatest improvement was the introduction of a lever, mounted on a translational stage. Through this arrangement, it was possible to fine position the mirrors between the microscope's objective and the sample under investigation. Finally, the coating formula for the mirroring surfaces was changed by the manufacturer, and the second generation of prisms did not have a problem with decaying mirrors.

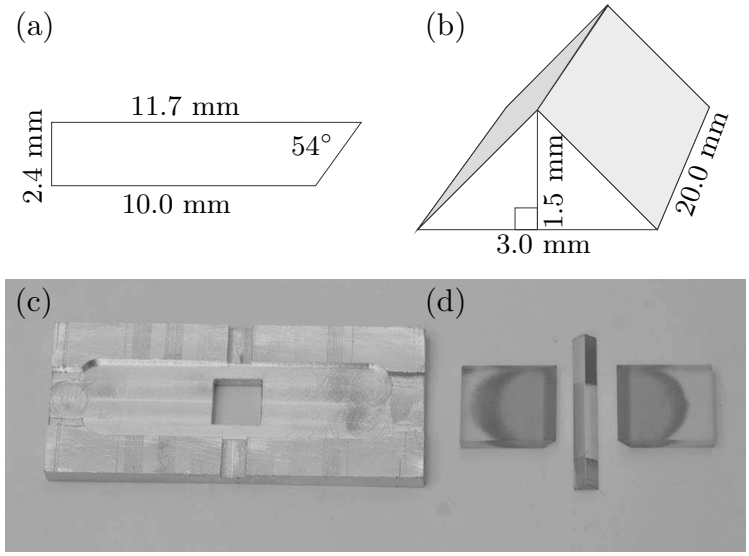

Figure 7.5: The second stereoscopic viewing configuration. (a) Sketch of side prism. (b) Sketch of central prism. Note that the length of the central prism has been increased compared to the previous system. The photograph shows the new holder (c) and the new prisms (d).

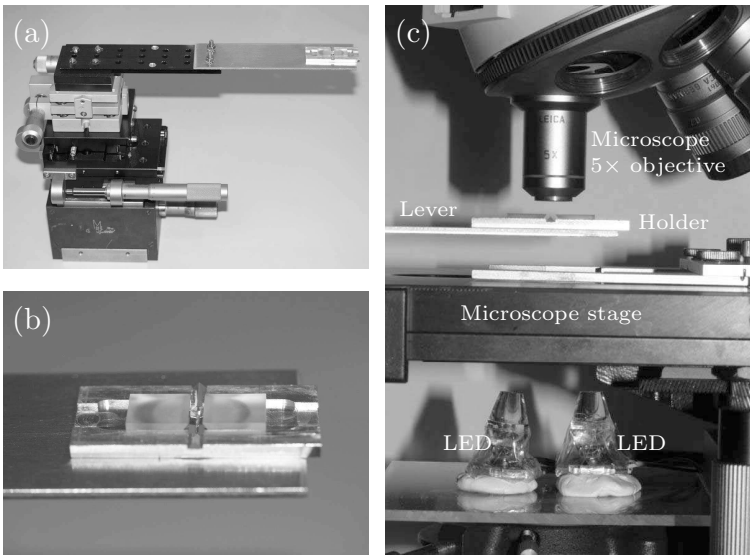

Figure 7.6: (a) The holder with mirrors placed on a lever extending from a translational stage. There is a hole in the lever, which in the figure is covered by the mirror system. (b) A closeup of the holder with mirrors. (c) Lever with holder and mirrors inserted in position between the sample and the microscope's objective. The illumination is from the back with two LEDs, positioned with an angle in between.

7.4 Further development and improvements

The stereoscopic viewing configuration presented in this thesis only exists on a prototype level and there are several possible improvements to the setup, which would facilitate the handling. In general, it would be useful if the whole system could be built upon some rigid framework, allowing high precision positioning of all the separate components. This is mainly an engineering task since the working principles have been demonstrated in this work.

7.4.1 Engineering of Scheimpflug correction

Different suggestions on how to engineer a Scheimpflug correction for the stereoscopic viewing configuration were mentioned in Sec. 6.4.3. These solutions are illustrated and explained in Fig. 7.7.

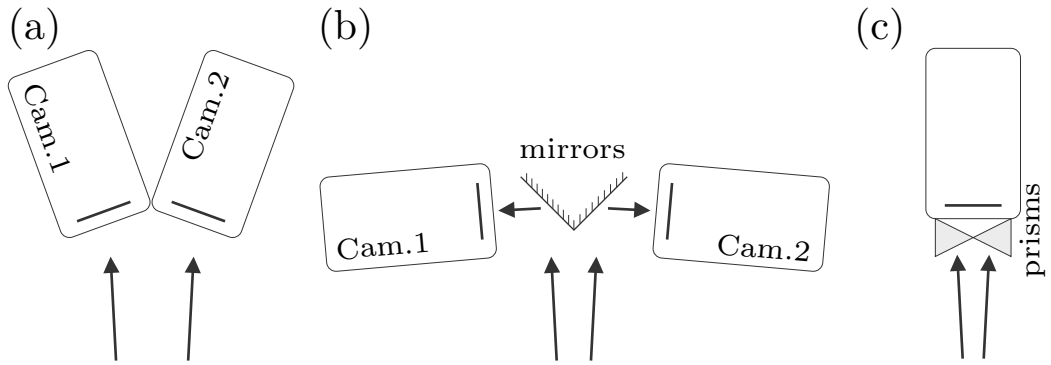

Figure 7.7: Different solutions to engineer a Scheimpflug condition. The arrows are indicating the ray-paths for the two views respectively. (a) The mirror system placed below the microscope's objective are adjusted for larger separation between views, allowing fitting of two cameras. (b) Alternative solution where additional splitting mirrors are introduced, separating the views to the sides. (c) Solution where the focus is adapted by the addition of glass prisms.

7.4.2 Tomographic micro-PIV

One technique that has attracted a lot of interest in the last years is tomographic PIV [89]. With this technique, several simultaneous views (recorded by 3–6 cameras) are utilized to make a 3D reconstruction of the flow field. Research on tomographic PIV has not been a part of this PhD study, and will therefore not be described in more detail. However, the stereoscopic viewing configuration here presented could offer a solution for a realization of tomographic micro-PIV, which has not been demonstrated to date.

One of the difficulties involved in tomographic micro-PIV is to fit several cameras in a very limited space. Moreover, the current stereoscopic micro-PIV realizations using standard stereo-microscopes can not be expanded to allow mounting of more than two cameras. In Sec. 6.4.3 it was mentioned that the stereoscopic viewing configuration described in this thesis could be expanded and used for tomographic micro-PIV. An illustration of a solution designed with four simultaneous views is provided in Fig. 7.8. The mirror system could be manufactured in two or more parts and then be welded together as shown in the figure.

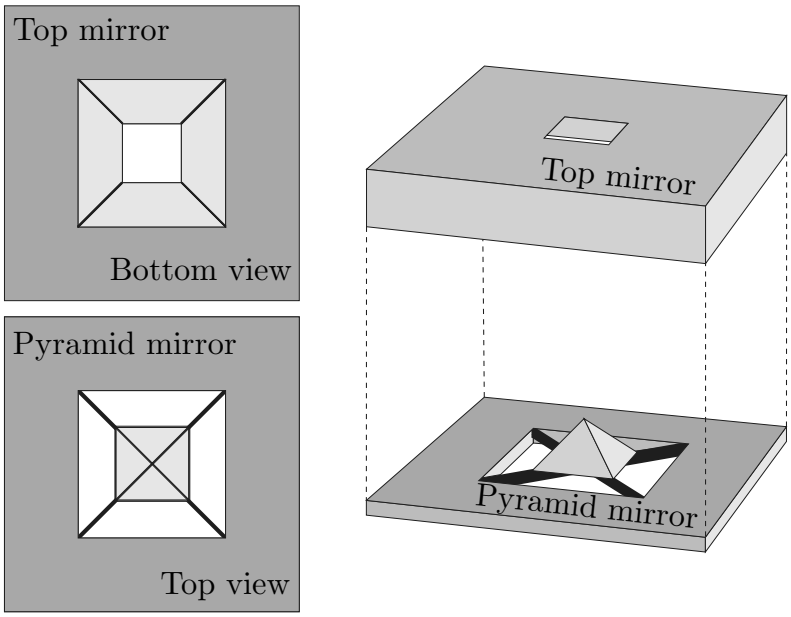

Figure 7.8: Suggested design for a mirror system that could be used for tomographic micro-PIV. Left panel shows the two prisms as seen with the reflecting surfaces placed upwards. Right panel shows how the prisms are put together.

Chapter 8

Outlook and conclusion

Outlook

The PhD study that is presented in this thesis, has included research in three main areas. Suggestions on further improvements, developments and new applications within the respective projects are provided below.

It will always be possible to increase the capacity and the adaptability of LED illumination for microfluidic applications, as long as the development within the semiconductor industry proceeds. With respect to further research projects, there is plenty more to do within the characterization of micro-PIV in scattered mode. Potentially, there could also be some application for which this recording mode is found to be especially useful. On a larger scale, it would be desirable to aim for a more final product (a low cost pulsed LED illumination system, which is easy to apply and handle). However, this is more of a task for a private or a commercial initiative than it is apt for institutional research. Finally, the high repetition rate of LEDs could be utilized for time resolved PIV (TR-PIV) applications.

With respect to investigations of acoustically actuated microdevices, there are several possibilities for further research continuing the work presented in this thesis. First of all, there are numerous examples of acoustically actuated microdevices, with different designs and actuation methods, that would be interesting to make subject to our investigation method. Such investigations would most certainly reveal interesting features of these specific designs, but also contribute to the understanding of acoustically actuated microdevices in general. Furthermore, it would be desirable to perform basic research on the influence and importance of various parameters (both physical and those of the design) to the emerging resonances. The task could be tackled by fabricating test-devices, as those examined in this thesis, and trying to vary only one parameter at a time. This work would be tedious and repetitive, but also rewarding, since such studies are crucial for the future development of acoustically actuated microdevices, and very little along this line has been presented to date. Furthermore, it would be intriguing to see how numerical methods could be utilized in the design of acoustic devices. One example is that of acoustic streaming in the proximity of wedges, where it would be most useful if numerical

methods could expose how to optimally design an acoustic micromixer utilizing this effect. Finally, as a suggestion for a smaller research project, the total effect in flow-through microdevices (such as the acoustic separator) could be mimicked by numerically applying pressure flow profiles onto stop-flow measurement of the acoustic resonant field. These combined velocity fields could thereafter be compared with flow-through measurements.

There are several ways in which the stereoscopic realization presented in this paper can be improved. The primary task would be to engineer a Scheimpflug correction, which is a clear limitation of the current system. Some suggestions on how to achieve this were provided in Chap. 7. Furthermore, the alignment, the operation and the accuracy of the system would gain from the composition of a supporting framework, allowing controlled positioning of the mirrors, the cameras, the sample and the light sources. The most awarding work would probably be to attempt a realization of tomographic micro-PIV, for instance as described in this thesis. Such efforts would benefit from concurrent work on the analysis side.

Conclusion

This thesis has included examples of investigations and development of the micro-PIV technique, as well as micro-PIV applied for other research. The three main parts have been: (1) Micro-PIV with LED illumination, (2) analysis of acoustic resonance phenomena using micro-PIV and (3) stereoscopic micro-PIV using a novel viewing configuration.

Micro-PIV with LED illumination
This work has demonstrated that LEDs are functional and very affordable illumination sources for micro-PIV. Micro-PIV with LED illumination is little described in the literature, and this study has provided the first more thorough description. Several advancements have been made, including the introduction of a novel front-lit LED illumination configuration, which allows micro-PIV with high magnification objectives and facilitates the experimental alignment substantially. Micro-PIV with illumination pulse lengths down to 1 μs has also been demonstrated to be feasible. Finally, the first realization of micro-PIV with LED illumination in fluorescent mode using standard fluorescent tracer particles has been provided.

Investigation of acoustic resonance phenomena
This study has demonstrated that full-image micro-PIV analysis in combination with images of transient particle motion is a suitable way to visualize acoustic effects in microfluidic chambers under piezo-actuation in the MHz range. By applying tracer particles of different sizes and properties, both acoustic radiation forces and acoustic streaming have been measured qualitatively. The experimental results were also compared with, and supported by, numerical solutions. Several acoustically actuated microdevices have been examined in this study. The most thorough project was the investigation of an acoustic separator, where it was found that the forming resonances in the separation channel are more complex than what has previously been described. The observed standing wave pat-

terns could be explained by considering that the acoustic eigenmodes in the channel are dominated by, primarily, a transverse wavelength and a longitudinal wavelength. Other acoustic phenomena which have been brought to attention in this work are the observations of acoustic streaming in the proximity of corners and wedges, and different 3D streaming effects.

Stereoscopic micro-PIV using a novel viewing configuration
A previously not described stereoscopic viewing configuration, utilizing mm-sized mirrors placed below the microscope's objective, has been devised and validated experimentally. The method has shown workable, both in calibration examples and in stereoscopic micro-PIV measurements in a test-device. One advantage with this kind of setup is that a large angle between the views can be engineered, which allows a high out-of-plane resolution. The current prototype still has a number of shortcomings; primarily, the system lacks a Scheimpflug correction.

Final remarks
I hope that this report has managed to explain the different research projects to the reader, and that the presented material would prove useful if he, or she, wishes to continue the development in one of the suggested (or any other) directions.

Appendix A

LED power supply

The power supplies for the LED system were built by Danchip's electronics workshop according to the author's specifications. A photo of one of the boxes is seen in Fig. A.1. A sketch of the electrical circuits, drawn by Danchip coworker Henrik Nielsen is provided in Fig. A.2. This diagram should be useful for anyone wishing to built their own control box.

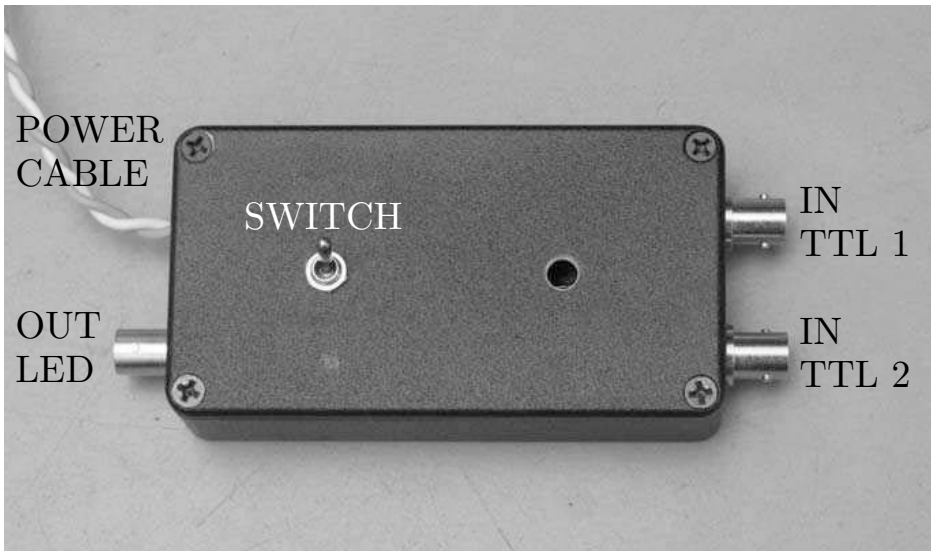

Figure A.1: Photo of the LED power supply. The LED is connected to the output. The box is built with two TTL inputs, for separate connection of cables for trigger pulse 1 and pulse 2, respectively. The switch on top of the box is a control for changing between two different power modes.

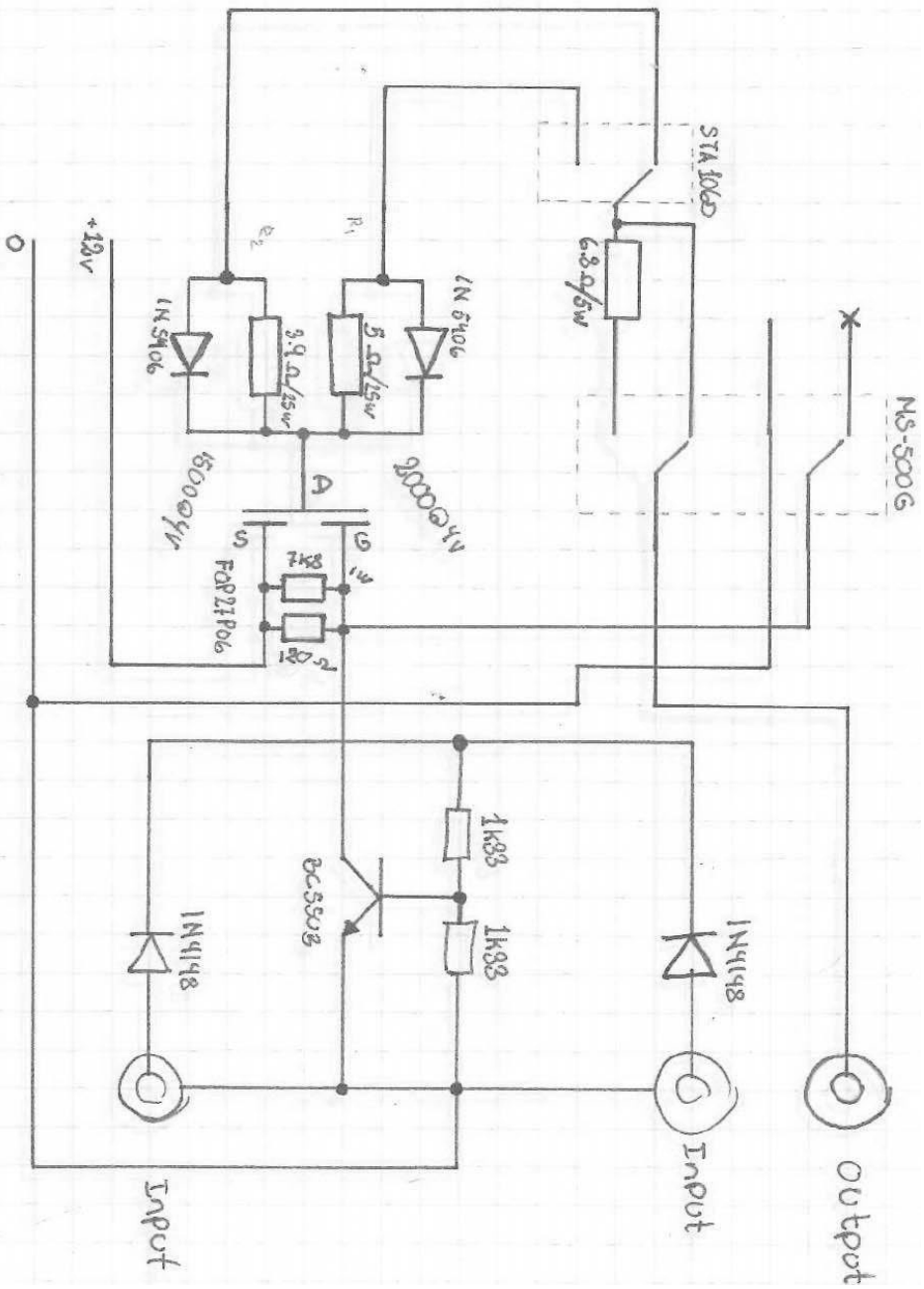

Figure A.2: Electrical circuit diagram of the power supply. Note that this box was designed with a switch for changing between two different power modes. Additionally, the box was built with two TTL inputs to mimic the control of a double cavity laser. Thus, there are ways in which the circuit diagram (and the box) can be simplified.

Appendix B

Extra acoustic figures

As a reference for future studies, this appendix includes additional micro-PIV measurements of the test-chips that were used in Chap. 4. Fewer image pairs than in [16] were used for the composition of these images, so all the figures are not of the uttermost quality. To allow small sized figures, only every second column and row of velocity vectors are displayed.

B.1 Circular chamber – 5 μm tracer particles

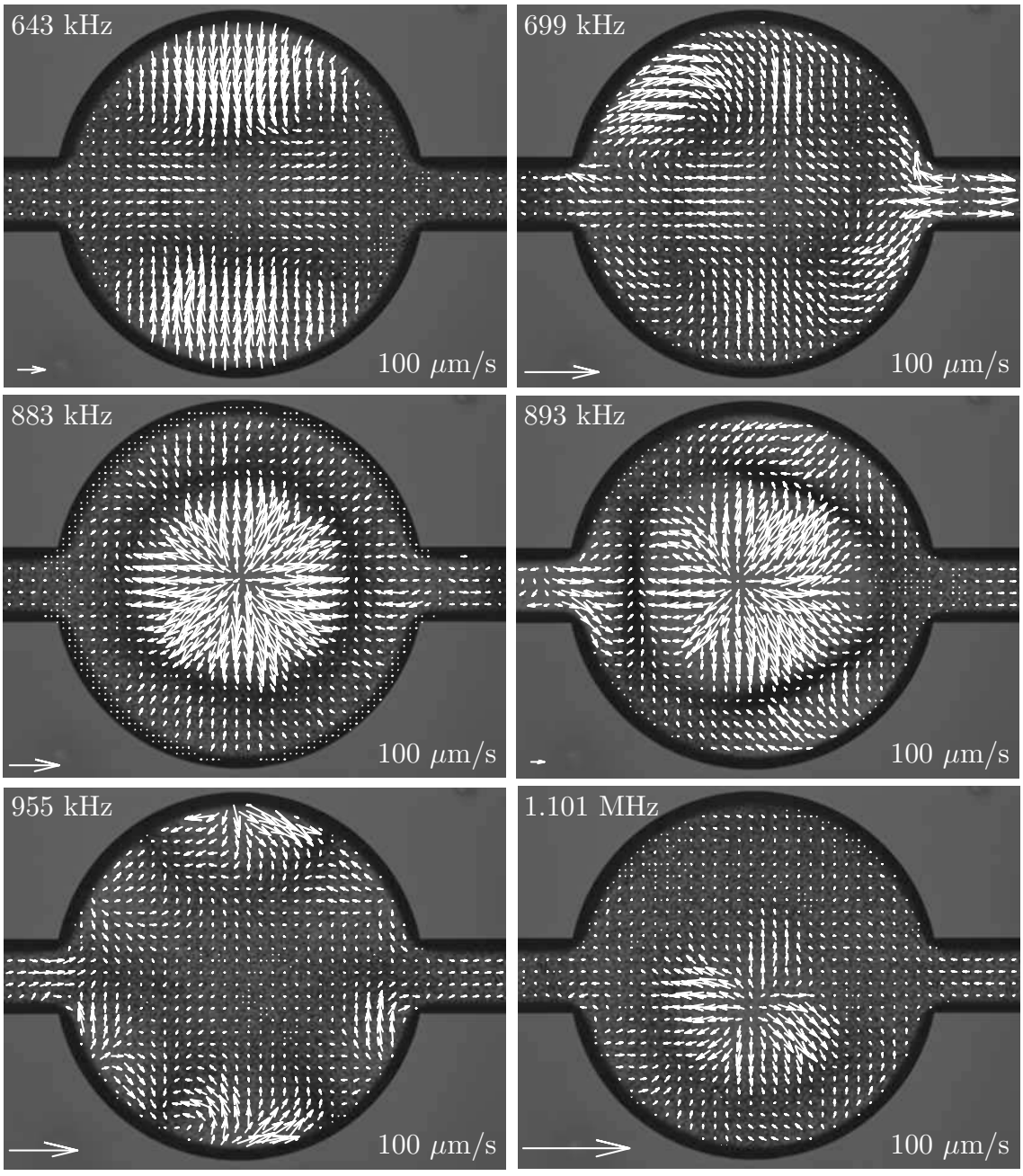

Figure B.1: 643 kHz – 1.101 MHz

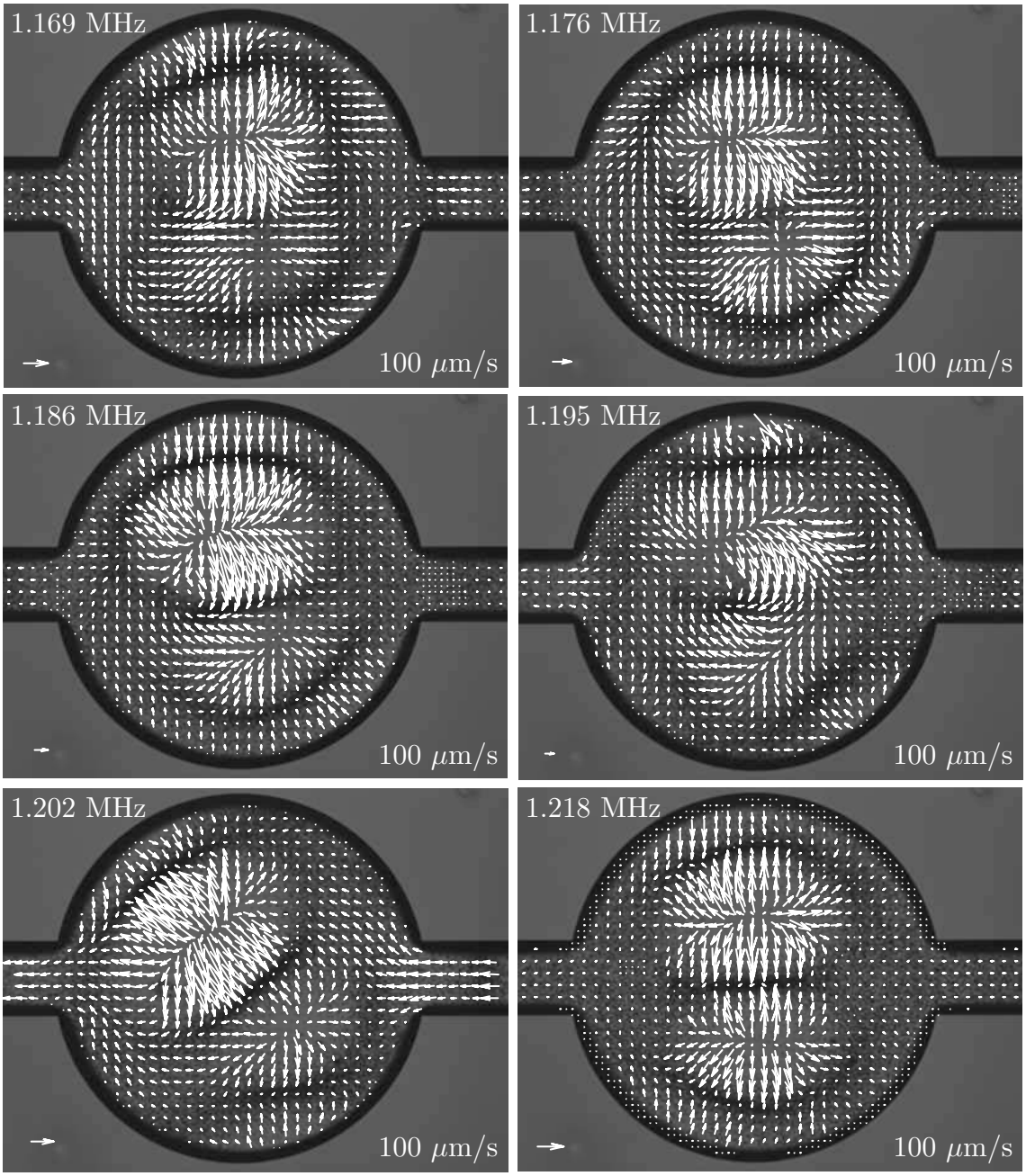

Figure B.2: 1.169 MHz – 1.218 MHz

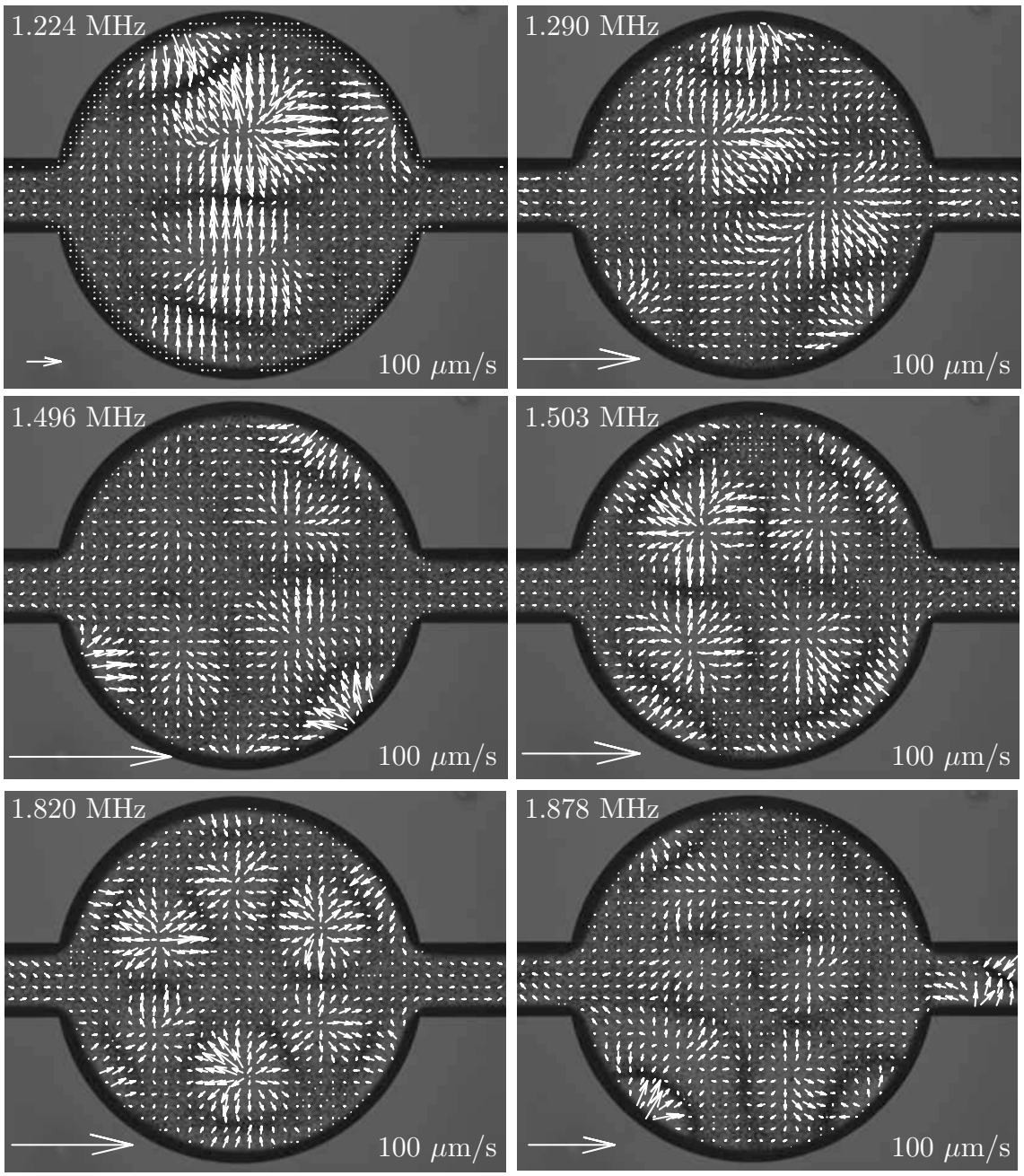

Figure B.3: 1.224 MHz – 1.878 MHz

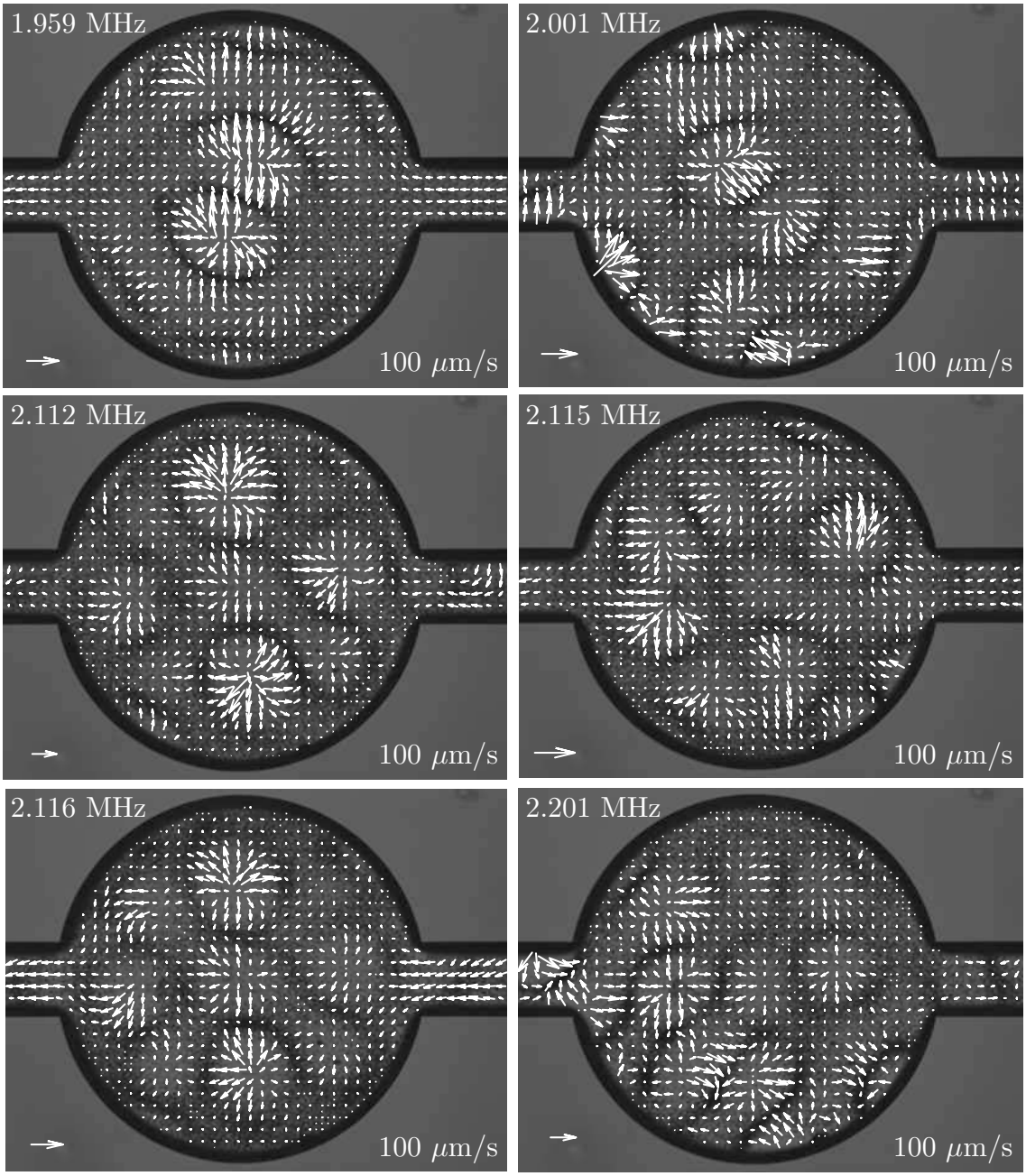

Figure B.4: 1.959 MHz – 2.201 MHz

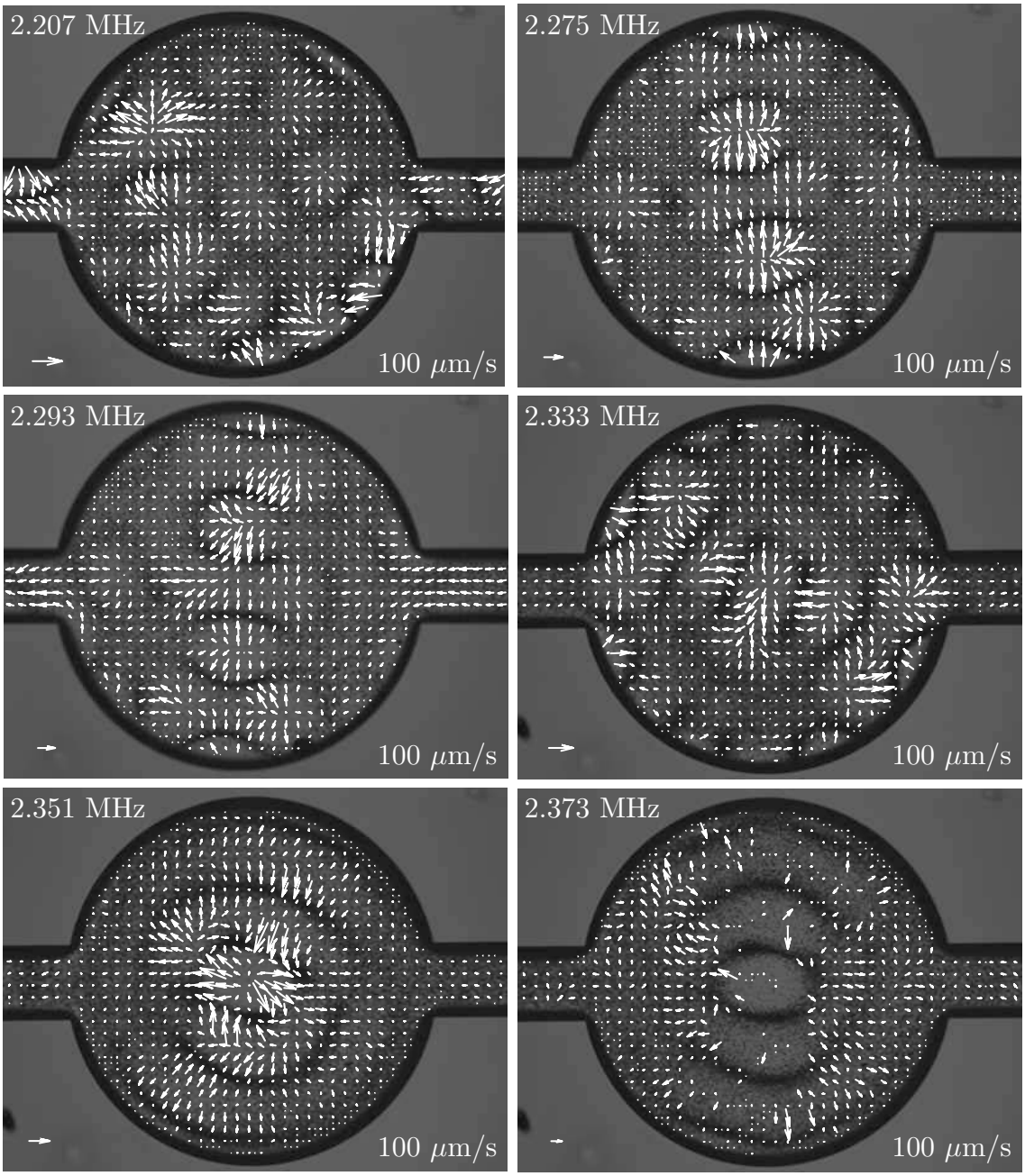

Figure B.5: 2.207 MHz – 2.373 MHz

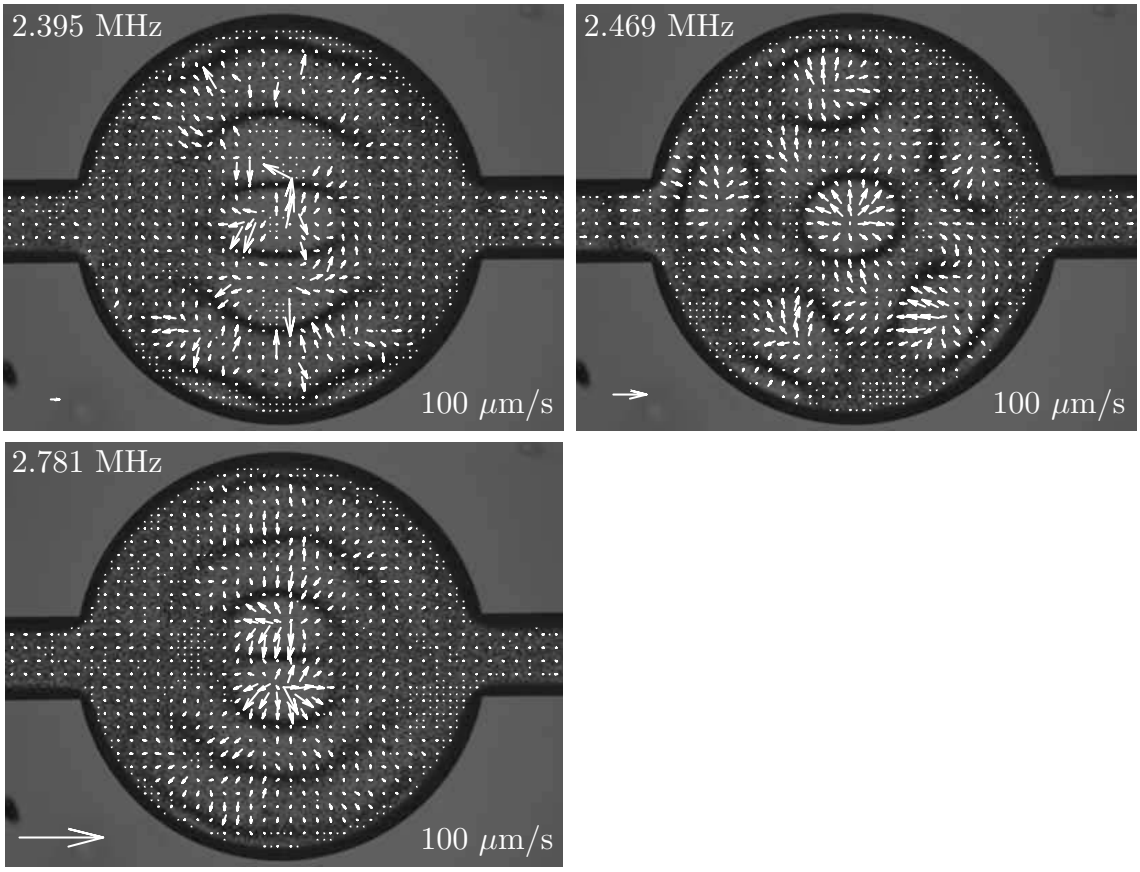

Figure B.6: 2.395 MHz – 2.781 MHz

B.2 Circular chamber – 1 μm tracer particles

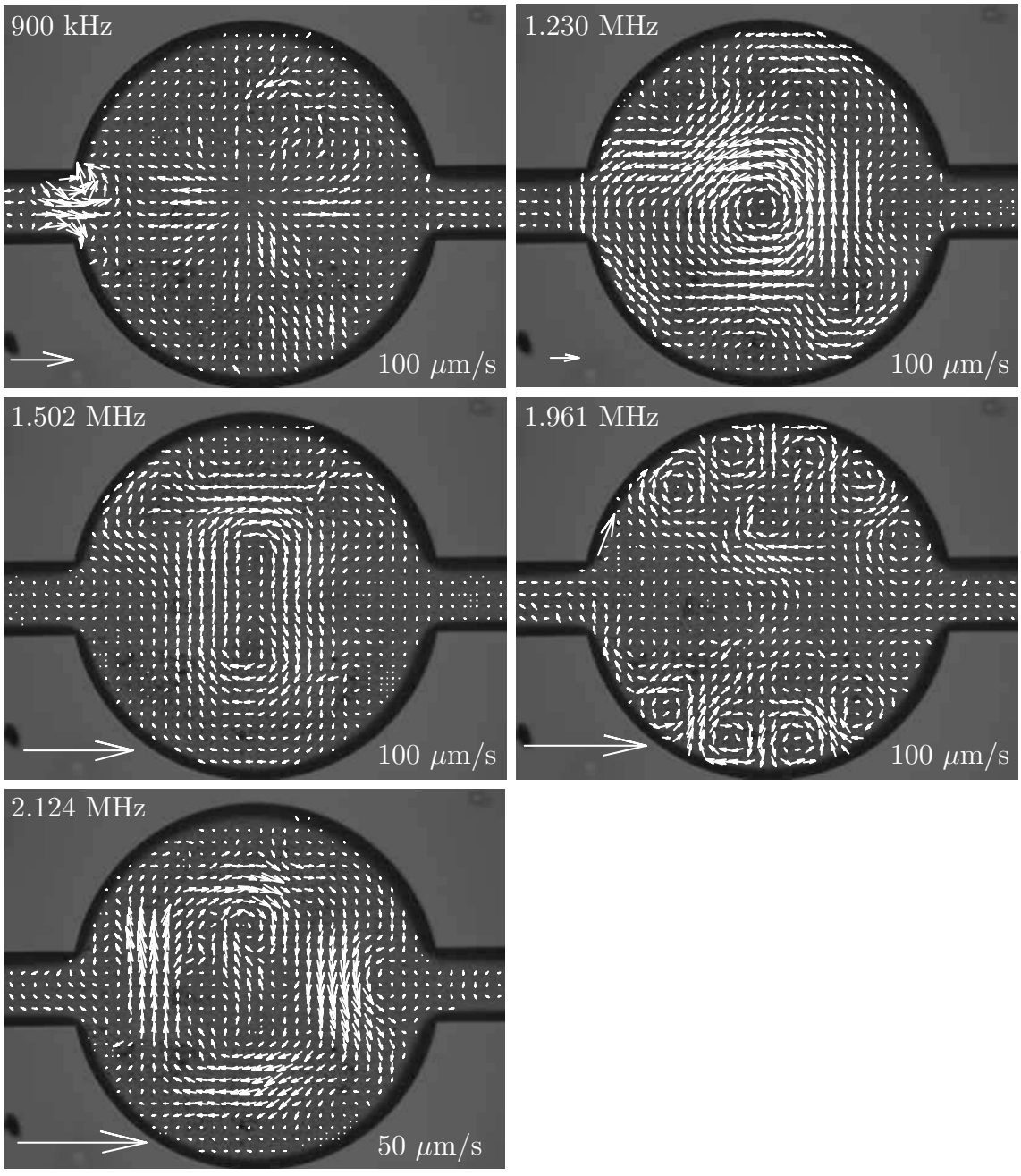

Figure B.7: 900 kHz – 2.124 MHz

B.3 Square chamber – 5 μm tracer particles

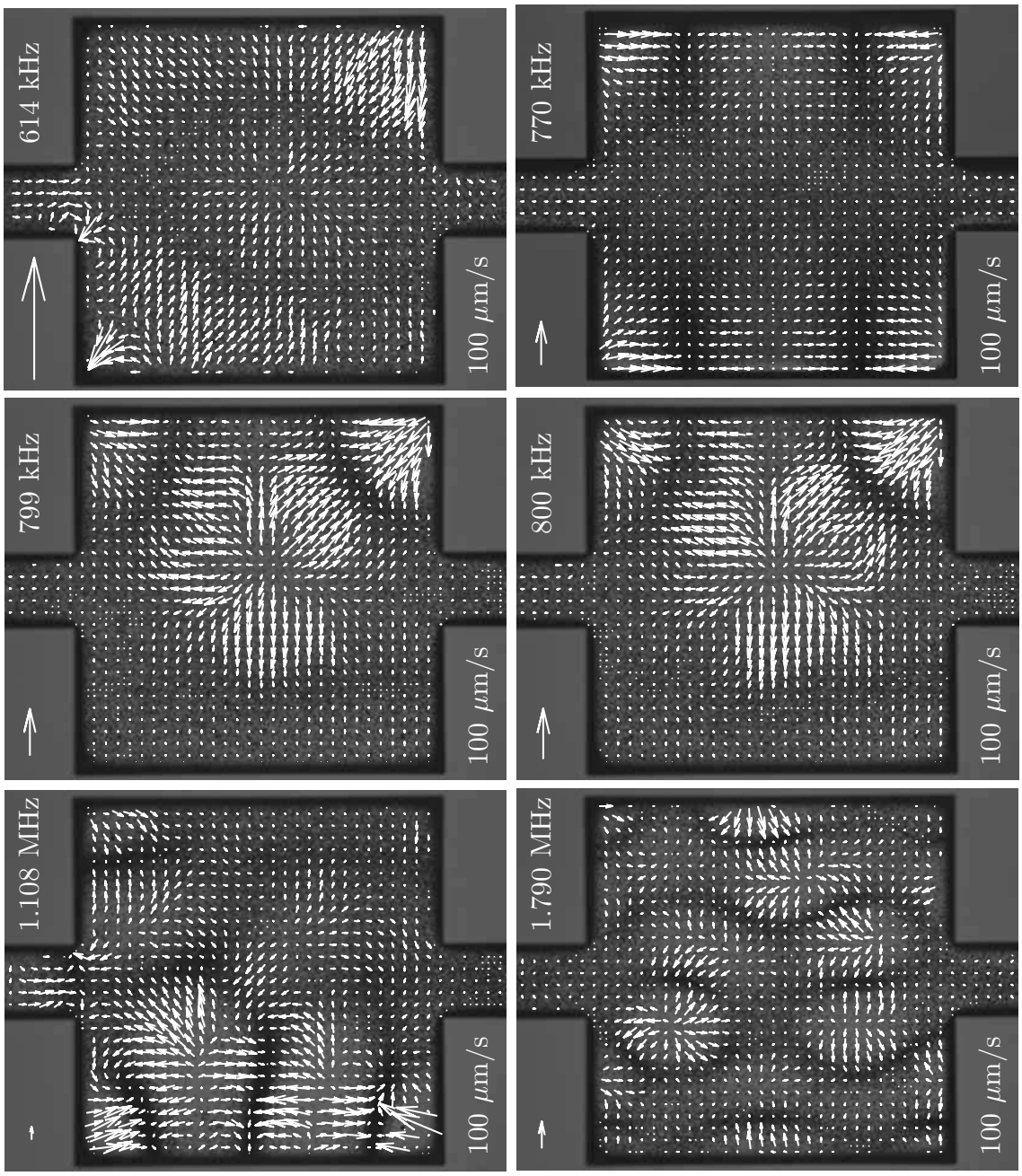

Figure B.8: 614 kHz – 1.790 MHz

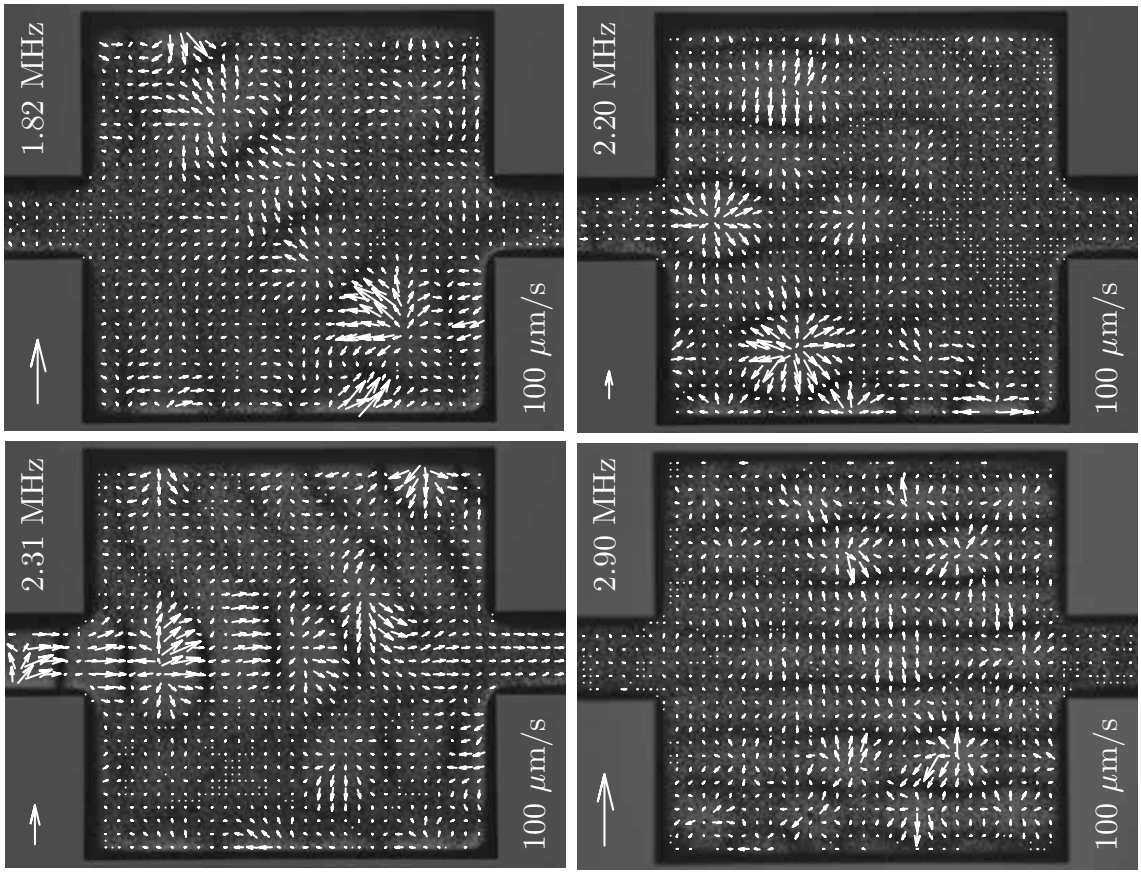

Figure B.9: 1.82 MHz – 2.90 MHz

Appendix C

Cleanroom fabrication processes

In this chapter the cleanroom fabrication processes[1] that were used in the PhD study are presented. In particular, the processes for the acoustic test-devices examined in Chap. 4 and the targets used in Chap. 6 are given.

C.1 Fabrication of acoustic test-devices

The acoustic chips were manufactured using a recipe previously developed by associate professor Klaus Bo Mogensen and others. The more specific recipe, adapted for the fabrication of the acoustic devices, was compiled primarily by lab-technician Fredrik Eriksson together with the author. SEM images of one of the devices are supplied in Fig. C.1.

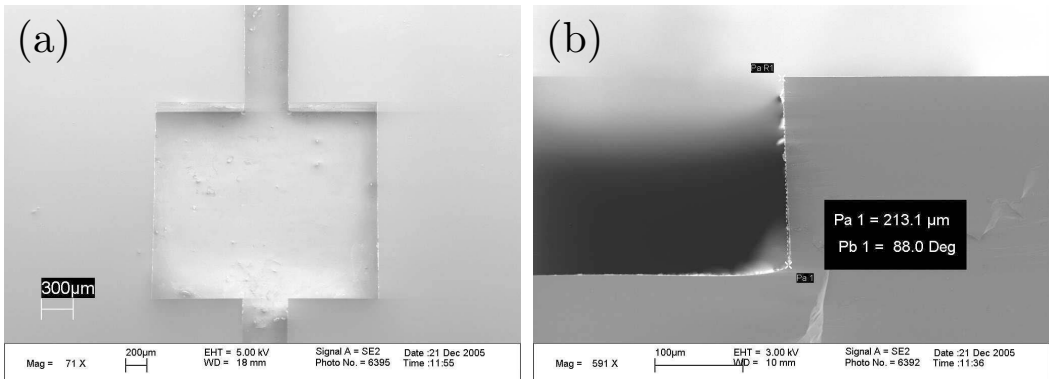

Figure C.1: SEM images of one of the acoustic test-devices with a square footprint. A top view of the whole chamber is shown in (a) and a side view for one of the walls is seen in (b).

[1]NB: the presented processes include instructions and recipes strictly valid only for DTU Danchip's cleanroom facilities

Fabrication process

1. Put a 500 μm thick double side polished silicon wafer for 30 s in HF, dry in the centrifuge.
2. Spin 9 μm (positive) resist. Use Track 2 in the cleanroom.
3. Let the wafer cool down in the air box for at least 1 h.
4. Exposure **back side** mask ∼60 s. (EVC aligner)
5. Develop 4 min in (NaOH), then dry.
6. Etch with ASE (advanced silicon etcher), program "DEEPETCH". Ratio: 7 s passivation and 8 s etching gives vertical sidewalls. Etch about 300 μm in depth. The ASE will etch about 4-5 μm/min.
7. Put the wafers in Piranha solution for 10 min.
8. Repeat step 1–5, but with exposure of **front side** mask. (Use double side alignment program)
9. Spin 9 μm (positive) resist onto a support wafer, but do not hardbake.
10. Press the two wafers together and hardbake. This procedure is required in order to etch holes through the main wafer using the ASE.
11. Etch with ASE. Stop etching when the main wafer is etched through.
12. Put the wafers in acetone over night. The resist will dissolve, and the main wafer can be separated from the support wafer. Discharge support wafer.
13. Put the silicon wafer and a 500 μm pyrex wafer (used as the lid) in Piranha for 10 min in order to make the surfaces hydrophilic. Dry with N_2-gun or spinner.
14. Bond wafers with anodic bonder at ∼1000–1100 V and ∼4 mA. Slowly raise the voltage to 1000 V and let it stay there for about 10 min.
15. Dice out the microchips with the saw.

C.2 Stereo target plates

The following cleanroom process was used to fabricate the targets that were utilized for the stereoscopic calibration in Sec. 6.4.2. A photo of the targets is shown in Fig. C.2.

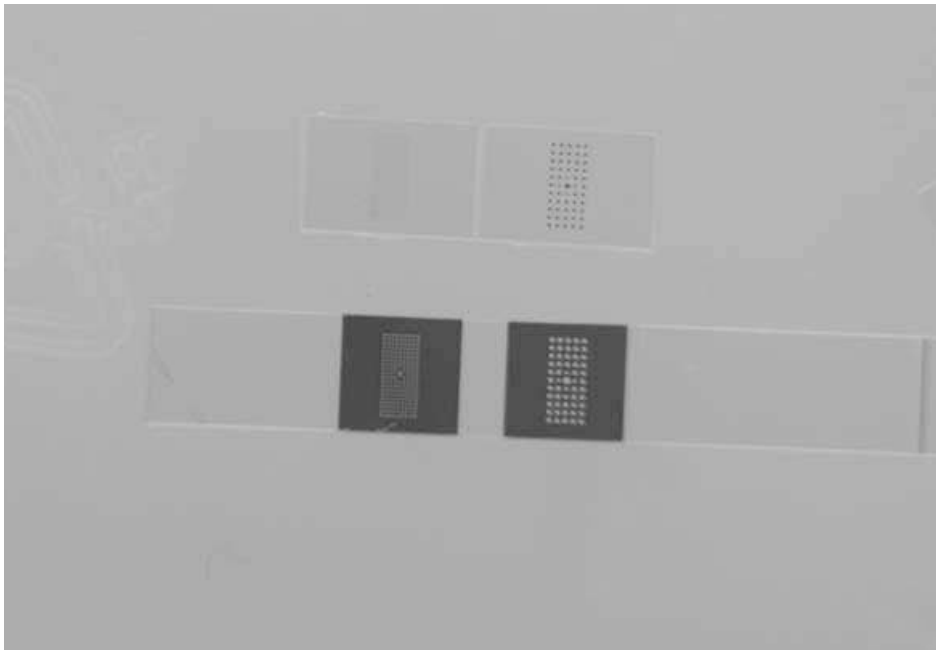

Figure C.2: Example of the targets that were used in the study. Two types of targets were fabricated. (top) Positive (with dots of photo-resist). (bottom) Negative (with holes in the layer of photo-resist).

Fabrication process

1. Clean the 500 μm pyrex wafer in the HMDS oven.
2. Spin 9 μm (positive) resist. Use Track 2 in the cleanroom. No long bake.
3. Let the wafer rest for about one hour.
4. Exposure $\sim$60 s. (EVC aligner)
5. Develop at least 5 min (until resist is gone).
6. Dry wafer in centrifuge.
7. Burn resist for one hour in 238°C oven.
8. Dice out targets with the saw.

Appendix D

Paper published in Ultrasonics

Title
Spatial confinement of ultrasonic force fields in microfluidic channels

Authors
O. Manneberg, S. M. Hagsäter, J. Svennebring, H. M. Hertz, J. P. Kutter, H. Bruus and M. Wiklund

Reference
Ultrasonics, 2008, DOI: 10.1016/j.ultras.2008.06.012.

ARTICLE IN PRESS

Ultrasonics xxx (2008) xxx–xxx

Contents lists available at ScienceDirect

Ultrasonics

journal homepage: www.elsevier.com/locate/ultras

Spatial confinement of ultrasonic force fields in microfluidic channels

Otto Manneberg [a], S. Melker Hagsäter [b], Jessica Svennebring [a], Hans M. Hertz [a], Jörg P. Kutter [b], Henrik Bruus [b], Martin Wiklund [a,*]

[a] Biomedical and X-ray Physics, Royal Institute of Technology, KTH-AlbaNova, SE-106 91 Stockholm, Sweden
[b] Department of Micro- and Nanotechnology, Technical University of Denmark, DTU Nanotech, Building 345 East, DK-2800 Kongens Lyngby, Denmark

ARTICLE INFO

Article history:
Received 21 January 2008
Received in revised form 9 June 2008
Accepted 19 June 2008
Available online xxxx

PACS:
43.25.Gf

Keywords:
Ultrasonic manipulation
Acoustic radiation force
Microfluidic chip
Particle image velocimetry
Spatial confinement
Cell handling

ABSTRACT

We demonstrate and investigate multiple localized ultrasonic manipulation functions in series in microfluidic chips. The manipulation functions are based on spatially separated and confined ultrasonic primary radiation force fields, obtained by local matching of the resonance condition of the microfluidic channel. The channel segments are remotely actuated by the use of frequency-specific external transducers with refracting wedges placed on top of the chips. The force field in each channel segment is characterized by the use of micrometer-resolution particle image velocimetry (micro-PIV). The confinement of the ultrasonic fields during single- or dual-segment actuation, as well as the cross-talk between two adjacent fields, is characterized and quantified. Our results show that the field confinement typically scales with the acoustic wavelength, and that the cross-talk is insignificant between adjacent fields. The goal is to define design strategies for implementing several spatially separated ultrasonic manipulation functions in series for use in advanced particle or cell handling and processing applications. One such proof-of-concept application is demonstrated, where flow-through-mode operation of a chip with flow splitting elements is used for two-dimensional pre-alignment and addressable merging of particle tracks.

1. Introduction

Ultrasonic standing wave (USW) manipulation technology in microfluidic chips has recently emerged as a powerful tool for, e.g., continuous alignment, separation, trapping and aggregation of micrometer-sized particles or cells [1,2]. We have previously shown that it is possible to generate independent standing wave fields in different directions inside a microfluidic channel, where each field is addressed by a specific external transducer [3]. However, a remaining problem is that USW manipulation technology has poor spatial localization in comparison to alternative contactless manipulation methods such as dielectrophoresis [4] and optical tweezers [5]. In the present paper, we demonstrate for the first time multiple spatially separated and confined ultrasonic force fields by microchannel design, with the aim of developing more advanced and complex lab-on-a-chip systems based on USW technology.

One characteristic of the present USW manipulation technology (that differs from the characteristics of dielectrophoresis and optical tweezers), is the possibility to generate a uniform force field in the entire fluid channel in a chip. For example, with USW technology it is possible to guide a particle or a cell through a microfluidic chip at constant velocity and without any contact with the channel walls [3], or to separate particles from a suspension at high flow rates [2]. On the other hand, dielectrophoresis has been used in more complex particle or cell processing systems where several manipulation functions are located at different sites along the fluid channel [4]. Here, different micro-electrode geometries define different addressable manipulation functions, each with high spatial accuracy in terms of both localization and confinement of the corresponding dielectrophoretic force field. Thus, advanced single-particle handling and processing systems are realized by combining several consecutive manipulation functions (such as alignment, parking, sorting, separation, etc.) and a continuous driving fluid flow. In comparison to dielectrophoresis, USW technology has a much lower degree of instrumentation complexity [6], and also better prospects for gentle and long-term handling of sensitive cells [7,8]. Therefore, it is of interest to investigate if USW technology can be used in advanced particle processing systems based on combinations of several spatially separated and localized manipulation functions.

To date, several different methods have been suggested for coupling of ultrasound from a transducer into a well-defined standing wave in a microfluidic chip. The standard approach is based on the one-dimensional resonator that consists of a stack of plane-parallel layers: a PZT layer, a coupling layer, a fluid layer and a reflecting layer [7,9,10], or with the reflecting layer exchanged for another

* Corresponding author. Tel.: +46 8 5537 8134; fax: + 46 8 5537 8466.
E-mail address: martin@biox.kth.se (M. Wiklund).

0041-624X/$ - see front matter © 2008 Elsevier B.V. All rights reserved.
doi:10.1016/j.ultras.2008.06.012

Please cite this article in press as: O. Manneberg et al., Spatial confinement of ultrasonic force fields in microfluidic channels, Ultrasonics (2008), doi:10.1016/j.ultras.2008.06.012

coupling layer and PZT layer [11,12]. However, it has been shown that in silicon/glass-based microfluidic chips, it is not of critical importance how the system is excited. For example, one reported method is based on exciting the channel perpendicularly to the outgoing wave from an external transducer [2]. An alternative approach, developed in our lab, is based on oblique coupling via a refracting wedge on an external transducer for controlled directing of the incident wave into the fluid channel [6]. Another reported method is based on bending vibrations of a glass plate in contact with the fluid channel [13]. However, all these methods typically result in a standing wave field that extends along the whole fluid channel. Thus, it is difficult to confine an ultrasonic field in a chip by wave propagation from an external transducer only.

We note that by integrating the PZT elements in the fluid channel, localization and confinement of an ultrasonic standing wave field can be obtained [14–16]. In such devices, the extent of the ultrasonic field is similar to the size of the PZT element (typically, 0.5–0.8 mm wide square elements designed for operation around 10 MHz). However, the generated standing wave field has a complicated lateral distribution due to strong near-field effects. Furthermore, the experimental arrangement is more complicated and less flexible than in similar devices using external transducers (e.g., in Refs. 2,6). Another restriction with channel-integrated PZT elements is the limited optical access, which excludes trans-illumination microscopy techniques. Finally, since the PZT element is in direct contact with the fluid inside the microchannel, the biocompatibility may be reduced due to, e.g., heating (cf. Ref. 8).

In the present paper, we demonstrate for the first time spatial localization, separation and confinement of multiple ultrasonic standing wave fields in optically transparent microfluidic chips utilizing remote actuation from external transducers. The method is based on local matching of the channel width to the transducer frequency in chips with non-uniform channel cross-sections. We present results from two different chip designs; one for investigating the dependence of the confinement on small differences in channel width, and one with flow splitting elements designed for two-dimensional alignment and addressable merging of particle tracks. The ultrasonic fields are quantified by the use of micrometer-resolution particle image velocimetry (micro-PIV) [17] during actuation of a single channel segment, or of two adjacent channel segments simultaneously. The results are important for the understanding of how ultrasonic resonances are formed in microfluidic chips, as well as for developing future particle handling systems with tailor-made, localized and confined ultrasonic resonances by microchannel design.

2. Theoretical background

As a basic condition for the design process, we assume that an ultrasonic resonance can be localized and confined through proper matching of the width and height (relative to the acoustic wavelength) of a particular channel segment. Furthermore, we assume that the total three-dimensional resonant field in a chip is a superposition of one-dimensional and spatially harmonic resonances in orthogonal directions, and that each such one-dimensional resonance can be remotely excited by an external frequency-specific transducer. These conditions are the starting point for the theoretical background presented below. However, we are aware that the conditions are simplifications. In reality, the resonances in a microfluidic chip should be regarded as full three-dimensional fields that extend not only in the fluid channel but rather in the whole chip structure. Therefore, the degree of localization and confinement of the field into a particular part of the fluid channel is a function of not only the channel geometry, but also the acoustic impedances and geometries of all supporting layers to the channel structure, including the whole fluid channel itself [18]. The validity of our simplified conditions below is further discussed in Section 5.

2.1. Ultrasonic standing wave manipulation

It has long been known that particles in an ultrasonic standing wave will be subjected to a primary radiation force F_{PR}, which attracts suspended particles to the nodes or antinodes of the standing wave depending on the acoustic properties of the particles relative to the surrounding medium [19]. Gor'kov has shown that the force on a particle of volume V in an arbitrary acoustic field is given by [20]

$$F_{PR} = -V\nabla\left(f_1 \frac{\langle p^2\rangle}{2\rho c} - \frac{3}{2}\rho f_2 \frac{\langle v^2\rangle}{2}\right) \tag{1}$$

where the brackets denote time-averaging and ρ and c are the density and speed of sound in the medium. f_1 and f_2 are contrast factors which depend on the speed of sound and the density of the medium and particle according to

$$f_1 = 1 - \frac{\rho c^2}{\rho_p c_p^2} \quad \text{and} \quad f_2 = 2\frac{\left(\rho_p - \rho\right)}{2\rho_p + \rho} \tag{2}$$

where the index p indicates "particle". In the simple case of a one-dimensional spatially sinusoidal standing wave in the x direction, Eq. (1) reduces to [20]

$$F_{PR}(x) = \frac{V p_0^2 k}{4\rho c^2}\left(f_1 + \frac{3}{2}f_2\right)\sin(2kx) \tag{3}$$

where k is the wavenumber, defined as $k = 2\pi/\lambda$ where λ is the acoustic wavelength. As mentioned above, a microchip containing a microchannel is a complex resonator. However, to a first approximation, the forces in such a channel can be obtained by simple superposition of plane-parallel resonators in perpendicular directions, each with a force field given by Eq. (3) [21]. This approximation (i.e., assuming no coupling between the orthogonal fields) is sufficiently accurate if the superposed fields do not operate at frequencies that are multiples of each other [22].

2.2. Force field quantification by micro-PIV

In the present work, the primary radiation force field F_{PR} is quantified in two dimensions (x and z, cf. Fig. 1) using the micro-PIV technique, in which the motion of tracer particles in the form of velocity vector fields is acquired from consecutive image frames [17]. F_{PR} is proportional to the bead velocity given that no other forces or flows are present, and that the time after activating a transducer is well above the time constant τ_p for reaching force equilibrium between F_{PR} and the viscous Stokes drag. The time constant τ_p is given by [23]

$$\tau_p = 2\rho_p r_p^2/9\eta \tag{4}$$

where r_p is the radius of the particle and η is the viscosity of the liquid medium. When representing the relative force fields with velocity fields, possible sources of error are, e.g., acoustic streaming [24] and sedimentation by gravity. Acoustic streaming will, through viscous drag, influence the particles with a force proportional to the particle radius r. As F_{PR} is proportional to r^3, the streaming will typically dominate when the particles are small ($r \sim 0.5$ μm) whereas F_{PR} will typically dominate when the particles are larger ($r \sim 5$ μm), as in our experiments. The time constant τ_{sed} for sedimentation a (vertical) distance h in a fluid channel is given by

$$\tau_{sed} = \frac{h}{v_{sed}} = \frac{9\eta h}{2(\rho_p - \rho)r_p^2 g} \tag{5}$$

Please cite this article in press as: O. Manneberg et al., Spatial confinement of ultrasonic force fields in microfluidic channels, Ultrasonics (2008), doi:10.1016/j.ultras.2008.06.012

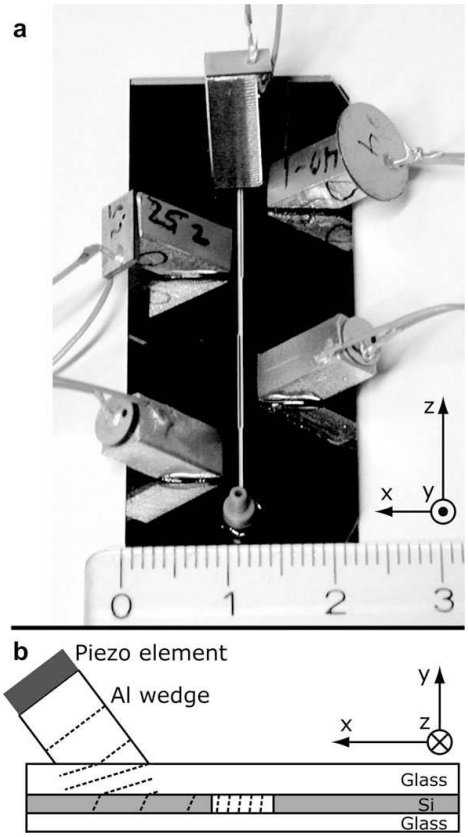

Fig. 1. Photograph (a) and schematic (not to scale) of cross-section (b) of the "Split Chip" with mounted transducers. The ruler scale is in millimeter. In (b), the dashed lines represent wavefronts incident at an angle typical for manipulation in the *x* direction.

where v_{sed} is the sedimentation speed and g is the acceleration of gravity. A typical value of τ_{sed} in our microchannels is 1 minute (for 5-μm-diam. polyamide beads in water, and choosing h as half the channel height), and is therefore of little importance.

2.3. Combined ultrasonic standing wave manipulation and flow

At the employed flow level (~0.1 μL/s) in our flow-through experiments (cf. Section 4.2), the flow is laminar in the whole channel structure (e.g., the Reynolds number is ~1). This means that once the force from the ultrasonic field has positioned a particle in a streamline, it will stay in that streamline until subjected to an external force. In our experiments, we distinguish between a streamline (path of a fluid element) and a particle track (path of a suspended particle).

3. Experimental arrangement

In our experiments, we used two different chip designs (described in detail in the next paragraph). Fig. 1a is a photograph of one of the chips used with mounted transducers and Fig. 1b illustrates the principles of the oblique coupling method (described in Refs. [3,6]). Both chips are fabricated from 51.4 × 22 mm^2 glass-silicon-glass stacks with the microchannel plasma etched into the silicon layer (GeSim, Germany). The bottom glass plate of both chips is 200 μm thick, i.e., close to standard microscope coverslip thickness. This allows investigation of the channel using any kind of high-resolution optical microscopy, including both trans- and epi-illumination techniques. The transducers were fabricated by gluing planar PZT elements (Pz26, Ferroperm, Denmark) to aluminum wedges (cf. Fig. 1a) with a cross-section of 5 × 5 mm^2, and driven at peak-to-peak voltages up to 13 V by separate function generators operating at different frequencies within the range 1.5–7 MHz. The aluminum wedges were attached to the chip (cf. Fig. 1a) using a quick-drying and water-soluble adhesive gel (Tensive, Parker Laboratories, USA).

The channel designs in the two investigated chips are schematically illustrated in Fig. 2. In both designs, the channel height is 110 μm and the widths are specifically designed to spatially confine resonances to a certain part of the channel by matching of width and frequency as to fulfill the simplified resonance condition

$$L = \frac{m}{2} \cdot \lambda = \frac{m}{2} \cdot \frac{c}{f} \tag{6}$$

where L is the channel width in the relevant direction, m is a positive integer, λ is the acoustic wavelength in the fluid, c is the speed of sound in the fluid and f is the acoustic frequency. The first chip (the "Step Chip", cf. Fig. 2a) has a straight channel with three 15-mm long sections of different width (643 μm, 600 μm and 500 μm). This chip is designed to utilize the fields from four different transducers, three of which act to focus particles in the *x* direction in each of the segments and one to levitate them in the *y* direction against the force of gravity. The second chip (the "Split Chip") has a more complex channel structure including two flow splitting elements, as illustrated in Fig. 2b. This chip is designed to use the fields from five different transducers operating at different frequencies to excite resonances in different parts of the chip, as indicated in Fig. 2b. Four of these can perform focusing of the particles in the *x* direction, and one is used to levitate the beads in the *y* direction. Thus, the operator can choose between merging particle tracks 1 + 2, tracks 2 + 3 or all tracks (cf. Fig. 2b). This principle

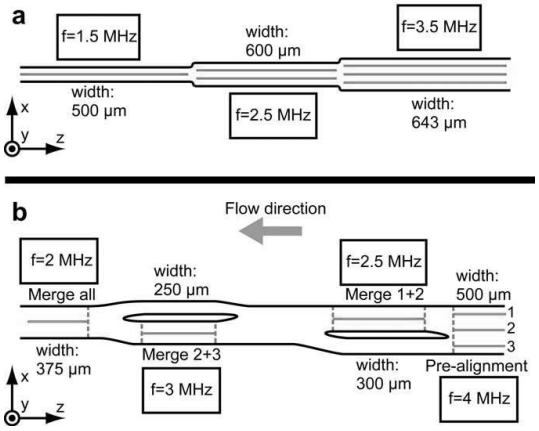

Fig. 2. Schematics (not to scale) top-view of the two employed chips; the "Step Chip" (a) and the "Split Chip" (b). The horizontal lines in the channels indicate the pressure node pattern, i.e., the lines to which particles are focused. The thin dashed lines in (b) mark the boundaries of the spatially confined resonances in each channel segment. The levitator transducers operating at 7.1 MHz is not shown, but is placed to the far right in experiments.

Please cite this article in press as: O. Manneberg et al., Spatial confinement of ultrasonic force fields in microfluidic channels, Ultrasonics (2008), doi:10.1016/j.ultras.2008.06.012

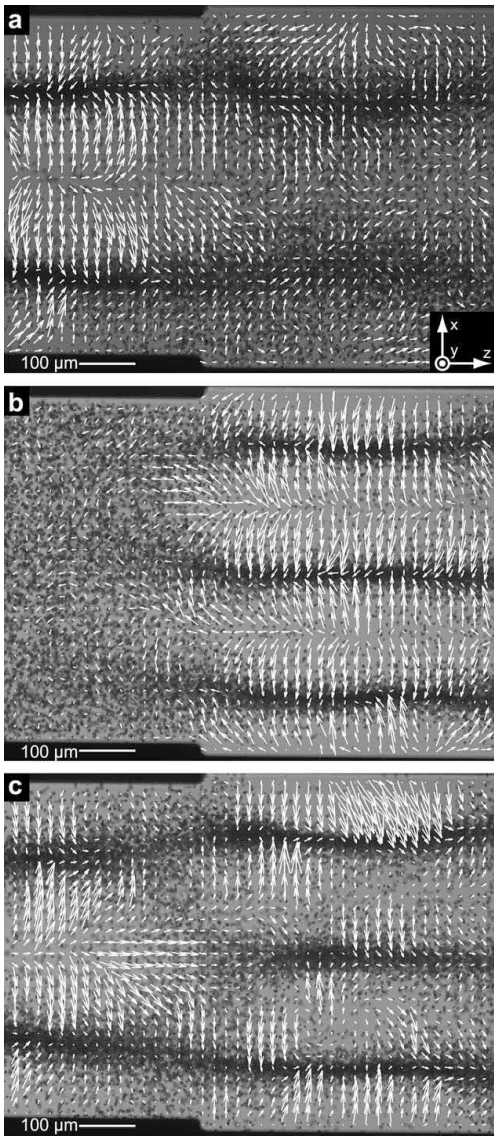

Fig. 3. Characterization of the primary radiation force field F_{PR} in the "Step Chip" (cf. Fig. 2a), measured by micrometer-resolution particle image velocimetry (micro-PIV). Actuation at 2.62 MHz of the left channel segment (a), at 3.51 MHz of the right channel segment (b), and at 2.62 and 3.51 MHz of both channel segments simultaneously (c). White arrows indicate the relative sizes and directions of the forces immediately after actuation is initialized. Dark regions indicate the bead pattern after ~10 s of actuation. The length of the coordinate arrows in (a) corresponds to a velocity of 10 μm/s.

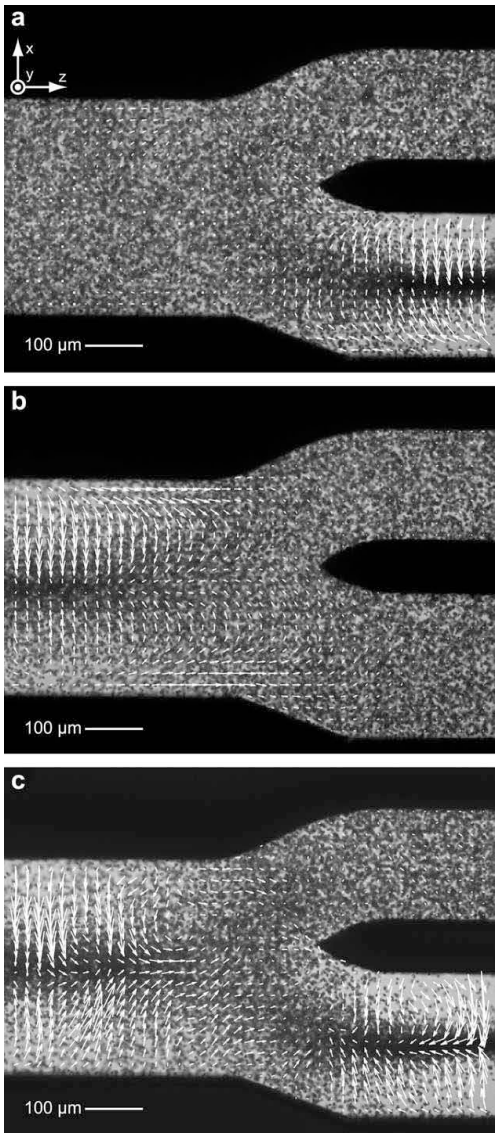

Fig. 4. Characterization of the primary radiation force field F_{PR} in the "Split Chip" (cf. Fig. 2b), measured by micrometer-resolution particle image velocimetry (micro-PIV). Actuation at 2.94 MHz of the lower right channel segment (a), at 2.10 MHz of the left channel segment (b), and at 2.94 and 2.10 MHz of both channel segments simultaneously (c). White arrows indicate the relative sizes and directions of the forces immediately after actuation is initialized. Dark regions indicate the bead pattern after ~10 s of actuation. The length of the coordinate arrows in (a) corresponds to a velocity of 10 μm/s.

could easily be expanded, and more in- or outlets added, to accommodate to the needs of a specific application (cf. Section 5).

Each resonance frequency was identified by tuning the applied transducer frequency in small steps around the expected frequency (according to Eq. 6) and observing the particle manipulation response in the corresponding channel segment. The operating frequency was then manually selected via the optimal ability to position particles quickly and uniformly into the nodes. Micro-PIV measurements were performed at all sites where the channels change width. To investigate the degree of spatial confinement, measurements were made with operation of either of the two or both transducers corresponding to actuation of the channel segments on each sides of the change in channel width (cf. Section

Please cite this article in press as: O. Manneberg et al., Spatial confinement of ultrasonic force fields in microfluidic channels, Ultrasonics (2008), doi:10.1016/j.ultras.2008.06.012

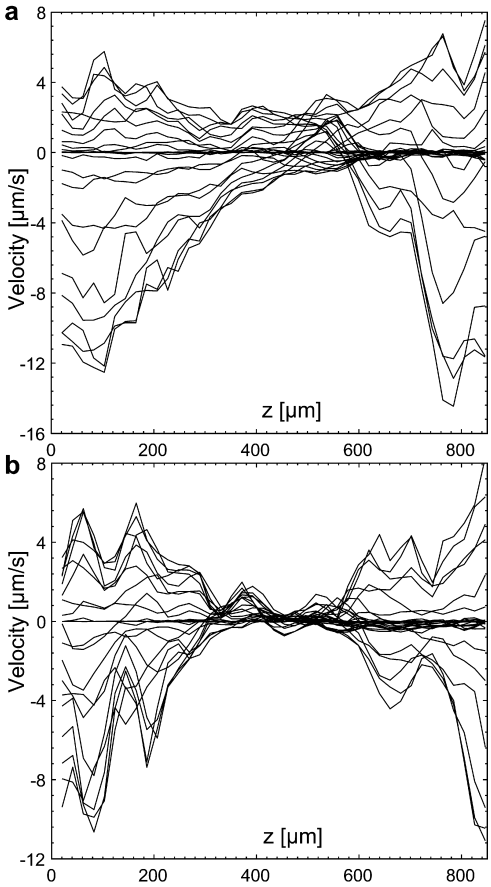

Fig. 5. Quantification of the field confinement and cross-talk in the "Split Chip" (cf. Fig. 4). The diagrams present the *x* components (cf. coordinate system in Fig. 4) of the velocity vectors along 31 *z*-axes equally spaced in the *x* direction. (a) Shows the *x* component of the sum of the velocity fields acquired when actuating the two channel segments separately (cf. Fig. 4a and b). (b) Shows the *x* component of the velocity field acquired when actuating both channel segments simultaneously (cf. Fig. 4c).

4). We also demonstrate flow-through-mode operation with the Split Chip operated with up to four independent transducers simultaneously.

Two different kinds of particles were employed in the experiments;10.4 μm green-fluorescent polystyrene beads (Bangs Labs, USA) for the flow-through experiments and 5 μm polyamide beads (Danish Phantom Design, Denmark) for the micro-PIV investigations. The beads were chosen for their resemblance to cells in both volume and acoustic properties. The beads were diluted in phosphate-buffered saline (PBS), pH 7.4, with 0.05% Tween-20 and introduced into the system by use of a syringe pump and Teflon (FEP) tubing.

In the flow-through-mode experiments (cf. Fig. 6), imaging was performed using an inverted microscope (AxioVert 135 M, Zeiss, Germany) with a 2.5 × /0.075 NA objective and a CCD camera (AxioCam HSc, Zeiss, Germany). In order to visualize both the beads and the microchannel, epi-flourescence and low-level trans-illumination were used simultaneously. For the micro-PIV measurements performed without flow (cf. Figs. 3 and 4), image frames

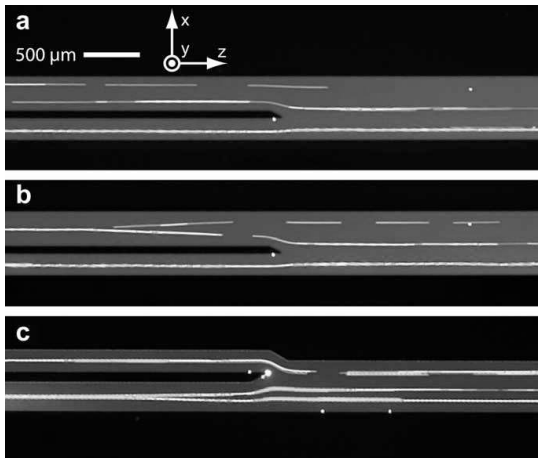

Fig. 6. Demonstration of addressable merging of particle tracks in the "Split Chip". Panels (a) and (b) show the particle tracks without and with actuation of the upper left channel segment, respectively. Panel (c) shows merging of the two lower particle tracks by actuation of the lower left channel segment. The chip site in (a) and (b) is located at the 2.5-MHz transducer, and the chip site in (c) is located at the 3.0-MHz transducer (cf. Fig. 2b).

were recorded in pairs with a CCD camera (HiSense MkII, Dantec Dynamics, Denmark) mounted on an inverted microscope (AxioVert 100, Zeiss, Germany) with a 10 × /0.25 NA objective. The sample was illuminated in back-lit mode by a light emitting diode (K2, Lumileds, USA) [25]. The velocity vector fields were generated using essentially the same protocol as described by Hagsäter et al. [18]. Before each new micro-PIV measurement, the channel was flushed and re-seeded to give a homogenous starting distribution of beads.

4. Results

In this section, we report on micro-PIV results when the two chips (the "Step Chip" and the "Split Chip") are operated without flow during ultrasonic actuation of one or several channel segments. The micro-PIV results are analyzed in order to quantify the spatial separation and confinement of the force fields, and possible cross-talk between two adjacent channel segments. Furthermore, we demonstrate flow-through operation of the Split Chip, which is designed for two-dimensional alignment and addressable merging of particle tracks.

4.1. Micro-PIV measurements

Micro-PIV measurements were made at all sites where the channels change width, both in the Step Chip and in the Split Chip (cf. Fig. 2). However, in order to minimize the number of figures we have chosen to present results from one representative site in each chip, which is sufficient for the important conclusions. The results are presented as plots of the velocity vector fields (white arrows) superimposed with images of beads (dark regions) in the microchannels (bright regions) (cf. Figs. 3 and 4). Typically, the vector field plots are averages of 10–15 data sets. The micro-PIV image frames were recorded immediately[1] after turning on the trans-

[1] "Immediately" means approximately a few tenths of a second after turning on the transducer(s). This is well above the time constant, τ, for reaching equilibrium between the radiation force and the viscous drag ($\tau \sim 1$ ms, cf. Section 2.2), and well below the time to reach a static bead distribution in the channel (~10 s).

Please cite this article in press as: O. Manneberg et al., Spatial confinement of ultrasonic force fields in microfluidic channels, Ultrasonics (2008), doi:10.1016/j.ultras.2008.06.012

ducer(s), thus representing the initial and transient motion of beads. In contrast, the bead images were acquired after a few seconds, thus representing the (near-)steady-state distribution of manipulated beads. Finally, in order to investigate and compare the radiation force fields produced by individual transducers, no levitation (in the *y* direction) was performed during the micro-PIV measurements.

4.1.1. Micro-PIV measurements in the Step Chip

In Fig. 3, the results are presented from measurements at the transition region from a 600 μm wide channel (left side) to a 643 μm wide channel (right side) in the Step Chip. In Fig. 3a the 600-μm-wide segment is actuated at 2.62 MHz, in Fig. 3b the 643-μm-wide segment is actuated at 3.51 MHz and in Fig. 3c both segments are actuated simultaneously at 2.62 and 3.51 MHz, respectively. Ideally, each force field should be confined to its corresponding channel segment (cf. Eq. 6). However, in Fig. 3a we see that the resonance "leaks" over to the adjacent channel segment. Although the forces are larger in the left segment, they are still significant in the right segment (i.e., on average a few times smaller to the right than to the left). Thus, a 7%-change in channel width is here not enough for fully confining the resonance to the proposed channel segment. On the other hand, the performance in Fig. 3b is much better in terms of confinement. Here, the forces in the left channel segment are insignificant in comparison to the right segment, and the transition region (defined as the approximately distance from maximum to insignificant forces in the *z* direction) is of the order of $\lambda/4$. Finally, Fig. 3c shows the results when both channel segments are actuated simultaneously. Interestingly, we see here that the "resonance-leakage" into the right segment originating from actuation of the left segment (cf. Fig. 3a) is quenched by the actuation of the right segment. We also note that the vector field in Fig. 3c is not equal to the sum of the vector fields in Fig. 3a and b. For example, the periodic variation of the force along the *z* direction in the right channel segment in Fig. 3c can not be derived from the vector fields in Fig. 3a and b.

4.1.2. Micro-PIV measurements in the Split Chip

In Fig. 4, the results from measurements at one site in the Split Chip are presented. The sub-figures show actuation at 2.94 MHz of the lower right channel segment (Fig. 4a), actuation at 2.10 MHz of the left channel segment (Fig. 4b), and actuation at 2.94 MHz and 2.10 MHz of both segments simultaneously (Fig. 4c). Here, we see almost no "resonance-leakage" (as seen in Fig. 3a). Instead, the fields are well-confined and independent, and with a transition region along the *z*-axis (cf. Section 4.1.1) of the order of $\lambda/2$. In Fig. 4c, we also note the occurrence of areas having velocity fields of rotational character. Such vortices, produced by acoustic streaming, may influence the particle movement in areas with low radiation forces (e.g., in the transition region between two adjacent channel segments).

In order to quantify more accurately the degree of spatial confinement, we have plotted the lateral velocity components (i.e., in the *x* direction in Fig. 4 where the radiation force is strongest) at different *x*-coordinates across the channel width, as a function of the *z*-position (i.e., along the channel direction). In Fig. 5a, the lateral velocities during single-segment actuation are plotted (i.e., the *x* components of the fields shown in both Fig. 4a and b). In Fig. 5b, the lateral velocities during dual-segment actuation are plotted (i.e., the *x* components of the field shown in Fig. 4c). Interestingly, we note that the forces are weaker in the central region (i.e., $\sim$300 μm < *z* < $\sim$600 μm) of the diagram in Fig. 5b, compared to the corresponding region of the diagram in Fig. 5a. Thus, a mutual force-quenching-effect is present in the transition region between the two channel segments during dual-segment actuation. This effect is even more distinct for the Step Chip, where it is directly visible in Fig. 3. Thus, for both chips, the cross-talk between two adjacent channel segments actuated simultaneously seems to have a character of destructive interference and is limited to a region of typical length $\sim\lambda/2$.

4.2. Flow-through operation of the Split Chip

In Fig. 6, we demonstrate flow-through-mode operation at 0.1 μL/s of the Split Chip by the use of up to four simultaneously driven transducers. This chip is designed for two-dimensional alignment and addressable merging of particle tracks. In contrast to the micro-PIV experiments (cf. Sections 4.1 and 4.2), the levitator transducer (cf. the uppermost transducer in Fig. 1a) was operated in all flow-through experiments, resulting in vertical (*y* direction) centering of the particles in the whole channel system. Together with operation of the pre-alignment transducer (cf. Fig. 2), the result is two-dimensional alignment (i.e., simultaneous focusing of particles in both the *x* and y directions), and thus controlled transport of particles in terms of both spatial position and uniform velocity [3]. In the present proof-of-concept chip design, all particles are injected through the one and only inlet for easier fluidic operation. However, depending on the needs from a future application, splitting of the main channel endpoints in several inlets and outlets is straightforward.

Fig. 6a and b shows the effect of actuating the upper left channel segment in flow-through-mode. In Fig. 6a, only the levitator and pre-alignment transducers are activated, and all aligned particles continue in their respective streamline (also in the upper right un-actuated channel segment). In Fig. 6b, the upper left channel segment is actuated, resulting in localized merging of the particle tracks 1 and 2 (cf. denotation in Fig. 2). The images are taken with a long exposure time, making the particles appear as streaks to better visualize their direction of movement. We clearly see that the particle tracks 1 and 2 merge at a distance longer than the $\sim\lambda/2$-distance after which the force in a channel segment was found to reach its full value (cf. Section 4.1). This is the result of the fluid flow giving the particles a considerable velocity component in the *z* direction relative the radiation-force-induced velocity component in the *x* direction. Fig. 6c shows merging of particle tracks 2 and 3 further down the channel by actuation of the lower left channel segment (cf. Fig. 2). This experiment was performed without any preceding merging of particle tracks 1 and 2. Finally, all particle tracks (two or three, depending on whether any of the above merging steps is performed) can be merged by actuation of the final channel segment (cf. Fig. 2).

5. Discussion and conclusions

In this section, we will consider channel design strategies for implementing several localized manipulation functions in series along a microchannel by the use of ultrasonic standing wave (USW) technology in a microfluidic chip. Ideally, each manipulation function should be represented by a localized and spatially confined force field that can be independently addressed by a frequency-specific external transducer. Furthermore, the overlap or cross-talk between the force fields of two adjacent manipulation functions should be minimized. Below we outline design criteria for advanced particle handling and processing chips based on our experimental observations.

When actuating a single-channel segment in both the Step Chip and the Split Chip, we may conclude that each primary radiation force field F_{PR} is localized to its corresponding segment (cf. Figs. 3 and 4). At the beginning and the end of each segment, there is an intermediate area of force field gradient (from insignificant to full value of the forces) with typical length $\lambda/4 - \lambda/2$ (where λ is the acoustic wavelength in the fluid). However, one exception to

Please cite this article in press as: O. Manneberg et al., Spatial confinement of ultrasonic force fields in microfluidic channels, Ultrasonics (2008), doi:10.1016/j.ultras.2008.06.012

this degree of confinement is seen in Fig. 3a, where the force field gradient in the z direction outside the actuated channel segment is very small. The result is a resonance that "leaks" out into the rest of the fluid channel. We believe that one reason for this poor confinement could be bad matching between the transducer resonance and the channel resonance. As a comparison, for a conventionally designed one-dimensional layered resonator (where the transducer is an active part of the resonator), the forces are typically halved if the driving frequency is changed with only 0.5% from a resonance peak [26]. In Fig. 3, the change in channel width corresponds to a change in resonance frequency of 7%. Thus, given a similar performance in our chip as in Ref. [26], we would not expect any forces of significance outside the actuated channel segment. On the other hand, if the channel segments are considered separately it is also possible that the wider channel segment in Fig. 3a is wide enough to be close to another resonance peak than the peak in the thinner segment. For example, when tuning the actuation frequency for a certain channel segment there are typically several resonance frequencies separated with similar (relative) steps as the relative change in channel width in Fig. 3. Thus, we believe that similar resonances would be found if we could "tune" the channel segment width at a fixed frequency (cf. e.g., Ref. [27]). One simple design strategy to avoid resonance leakage is to employ much larger steps in channel width, as demonstrated in the Split Chip.

When two adjacent channel segments are actuated simultaneously by the use of two transducers operating at different frequencies, we conclude that no cross-talk of significance (for the performance of each manipulation function) occurs in neither of the two chips. Typically, there is a near-force-free transition region between the manipulation functions of length $\sim\lambda/4$ in the Step Chip (cf. Fig. 3c), and $\sim\lambda/2$ in the Split Chip (cf. Figs. 4c and 5). The reason for the longer transition region in the Split Chip is due to the gradually (and not stepwise) increasing channel width in that chip. However, it is important to note that the sum of the force fields during single-segment actuation is not equal the force field during dual-segment actuation. Minor field coupling effects are visible in Figs. 3 and 4, e.g., periodic force variations in the z direction (along the channel), acoustic-streaming-induced vortices in low-force regions, and mutual quenching of "leaky" resonances in the intermediate area between the segments. Neither of these effects causes any reduction in performance of significance of a particle handling/processing chip based on several spatially separated manipulation functions (as demonstrated in e.g., Fig. 6).

Finally, it should be noted that the radiation forces are not constant throughout the segment (i.e., along the z-axis) to which it is confined. There will be periodically recurring areas where the focusing component of the force is very weak, or indeed is almost equal to zero. Actually, this is a general effect that is visible during both single- and multi-segment actuation. The reason is that we do not solely have a simple standing wave in the channel, but rather a three-dimensional resonance which exists in the whole chip structure, including all supporting layers to the fluid channel (such as the silicon layer, the glass layers, the external transducers, and even the microscope chip holder). While it is possible to design the system so that the force field is considerably confined, the rest of the chip will still influence the actual shape of the confined field. Finite-element simulations on our chips (data not shown) using the method described in Ref. [18] predict the existence of such areas, which are confirmed in our experiments (cf. e.g., Fig. 3c) but also in other reports (see e.g., Refs. 18,22,28). The influence of the entire chip (in terms of material choices and geometry) on the resonance shape is the underlying reason for this phenomenon. For example, a simple and straight half-wavelength channel does not focus particles into a straight line, but rather into slightly curved lines and at some places not at all under static (no-flow) conditions. However, this effect is often not visible in flow-through applications for several reasons. Firstly, the laminar flow profile will cause a particle to simply follow its streamline through areas where the forces are low. Secondly, any effect on the bead movement due to the force asymmetry around curved nodes is typically cancelled out in flow-through-mode. In our suggested flow-through application (cf. Section 4.2), these effects will be of little or no importance for the performance of the chip. However, for a chip designed for no or very low flow, or designed for retention of particles in a flow, the effects must be considered as a part of the design process.

Acknowledgements

The authors would like to thank Peder Skafte-Pedersen at MIC/DTU for his simulations of resonances in the chip. This paper was generated in the context of the *CellPROM* project, funded under the 6th Framework Program of the European Community (Contract No.: NMP4-CT-2004-500039). The work was also supported by the Swedish Research Council for Engineering Sciences.

References

[1] M. Wiklund, H.M. Hertz, Ultrasonic enhancement of bead-based bioaffinity assays, Lab Chip 6 (2006) 1279–1292.
[2] T. Laurell, F. Petersson, A. Nilsson, Chip integrated strategies for acoustic separation and manipulation of cells and particles, Chem. Soc. Rev. 36 (2007) 492–506.
[3] O. Manneberg et al., Elementary manipulation functions for gentle and long-term handling of cells in microchannels by ultrasonic standing waves, Proc. of Nanotech-Montreux 2006, Montreux, Switzerland, 2006.
[4] T. Müller, A. Pfennig, P. Klein, G. Gradl, M. Jäger, T. Schnelle, The potential of dielectrophoresis for single-cell experiments, IEEE Eng. Med. Biol. 22 (2003) 51–61.
[5] J. Enger, M. Goksör, K. Ramser, P. Hagberg, D. Hanstorp, Optical tweezers applied to a microfluidic system, Lab Chip 4 (2004) 196–200.
[6] M. Wiklund, C. Günther, R. Lemor, M. Jäger, G. Fuhr, H.M. Hertz, Ultrasonic standing wave manipulation technology integrated into a dielectrophoretic chip, Lab Chip 6 (2006) 1537–1544.
[7] J. Hultström, O. Manneberg, K. Dopf, H.M. Hertz, H. Brismar, M. Wiklund, Proliferation and viability of adherent cells manipulated by standing-wave ultrasound in a microfluidic chip, Ultrasound Med. Biol. 33 (2007) 145–151.
[8] J. Svennebring, O. Manneberg, M. Wiklund, Temperature regulation during ultrasonic manipulation for long-term cell handling in a microfluidic chip, J. Micromech. Microeng. 17 (2007) 2469–2474.
[9] J.J. Hawkes, W.T. Coakley, Force field particle filter, combining ultrasound standing waves and laminar flow, Sens. Actuator B-Chem. 75 (2001) 213–222.
[10] N.R. Harris, M. Hill, S. Beeby, Y. Shen, N.M. White, J.J. Hawkes, W.T. Coakley, A silicon microfluidic ultrasonic separator, Sens. Actuator B-Chem. 95 (2003) 425–434.
[11] K. Yasuda, Non-destructive non-contact handling method for biomaterials in micro-chamber by ultrasound, Sens. Actuator B-Chem. 64 (2000) 128–135.
[12] S. Kapishnikov, V. Kantsler, V. Steinberg, Continuous particle size separation and size sorting using ultrasound in a microchannel, J. Stat. Mech. P01012 (2006) 1–15.
[13] A. Haake, J. Dual, Positioning of small particles by an ultrasound field excited by surface waves, Ultrasonics 42 (2004) 75–80.
[14] T. Lilliehorn, U. Simu, M. Nilsson, M. Almqvist, T. Stepinski, T. Laurell, J. Nilsson, S. Johansson, Trapping of microparticles in the near field of an ultrasonic transducer, Ultrasonics 43 (2005) 293–303.
[15] T. Lilliehorn, M. Nilsson, U. Simu, S. Johansson, M. Almqvist, J. Nilsson, T. Laurell, Dynamic arraying of microbeads for bioassays in microfluidic channels, Sens. Actuator B-Chem. 106 (2005) 851–858.
[16] M. Evander, L. Johansson, T. Lilliehorn, J. Piskur, M. Lindvall, S. Johansson, M. Almqvist, T. Laurell, J. Nilsson, Noninvasive acoustic cell trapping in a microfluidic perfusion system for online bioassays, Anal. Chem. 79 (2007) 2984–2991.
[17] J.G. Santiago, S.T. Wereley, C.D. Meinhart, D.J. Beebe, R.J. Adrian, A particle image velocimetry system for microfluidics, Exp. Fluids 25 (1998) 316–319.
[18] S.M. Hagsäter, T. Glasdam Jensen, H. Bruus, J.P. Kutter, Acoustic resonances in microfluidic chips: Full-image micro-PIV experiments and numerical simulations, Lab Chip 7 (2007) 1336–1344.
[19] M. Gröschl, Ultrasonic separation of suspended particles – Part I: fundamentals, Acta Acustica 84 (1998) 432–447.
[20] L.P. Gor'kov, On the forces acting on a small particle in an acoustic field in an ideal fluid, Sov. Phys. Doklady 6 (1962) 773–775.
[21] M. Wiklund, Ultrasonic enrichment of microparticles in bioaffinity assays, PhD Thesis, Royal Institute of Technology (2004) ISBN 91-7283-723-3.

Please cite this article in press as: O. Manneberg et al., Spatial confinement of ultrasonic force fields in microfluidic channels, Ultrasonics (2008), doi:10.1016/j.ultras.2008.06.012

[22] S. Oberti, A. Neild, J. Dual, Manipulation of micrometer sized particles within a micromachined fluidic device to form two-dimensional patterns using ultrasound, J. Acoust. Soc. Am. 121 (2007) 778–785.
[23] H. Bruus, Theoretical Microfluidics, Oxford University Press, Oxford, 2007.
[24] L.K. Zarembo, Acoustic streaming, in: L.D. Rozenberg (Ed.), High-Intensity Ultrasonic Fields, Plenum Press, New York, 1971, pp. 138–199. vol. 85, part 3.
[25] S.M. Hagsäter, C.H. Westergaard, H. Bruus, J.P. Kutter, Investigations on LED illumination for micro-PIV including a novel front-lit configuration, Exp. Fluids 44 (2008) 211–219.
[26] M. Hill, The selection of layer thicknesses to control acoustic radiation force profiles in layered resonators, J. Acoust. Soc. Am. 114 (2003) 2654–2661.
[27] M. Wiklund, J. Toivonen, M. Tirri, P. Hänninen, H.M. Hertz, Ultrasonic enrichment of microspheres for ultrasensitive biomedical analysis in confocal laser-scanning fluorescence detection, J. Appl. Phys. 96 (2004) 1242–1248.
[28] S.M. Hagsäter, A. Lenshof, P. Skafte-Pedersen, J.P. Kutter, T. Laurell, H. Bruus, Acoustic resonances in straight micro channels: beyond the 1D-approximation, Lab Chip (2008). doi: 10.1039/b801028e.

Please cite this article in press as: O. Manneberg et al., Spatial confinement of ultrasonic force fields in microfluidic channels, Ultrasonics (2008), doi:10.1016/j.ultras.2008.06.012

Appendix E

Stereo holder

The different holders for the mirrors that were used in the stereoscopic micro-PIV project were manufactured by Stig Ahrent Petersen at Danchip's mechanical workshop according to the author's specifications. Fig. E.1 shows a CAD drawing of the holder that was used in the second stereoscopic viewing configuration. The manufacturing of the device was also done by Stig Ahrent Petersen.

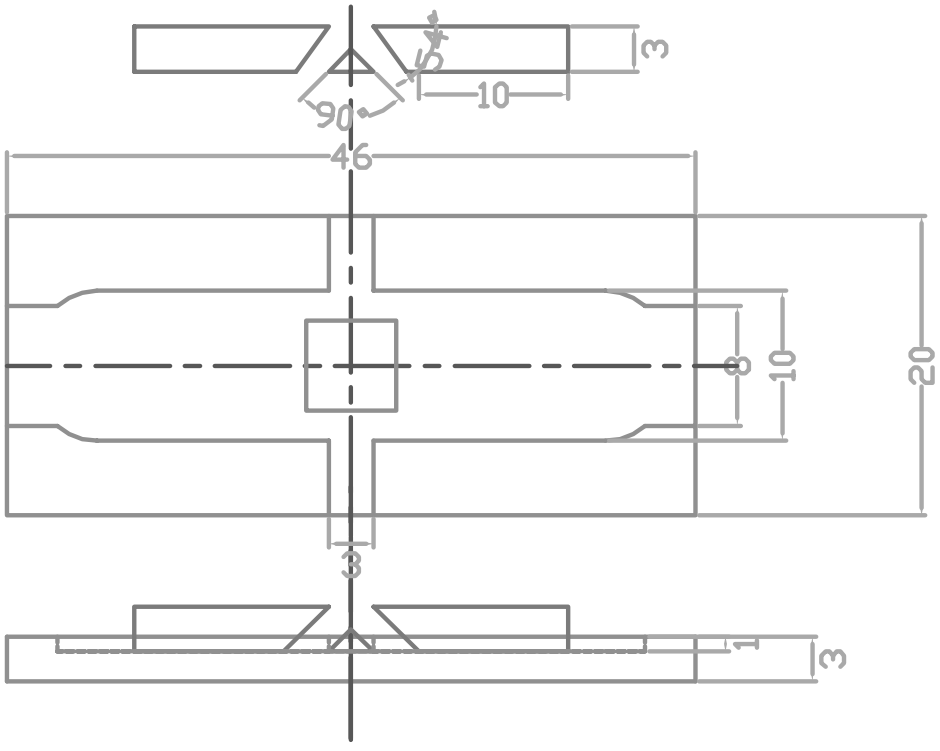

Figure E.1: CAD drawing of the prism holder that was used in the second stereoscopic viewing configuration. The substrate material was aluminium. Dimensions are in mm.

Bibliography

[1] RJ Adrian, "Scattering particle characteristics and their effect on pulsed laser measurements of fluid flow: speckle velocimetry vs. particle image velocimetry", *Applied Optics*, 1984, **23**, 1690–1691.

[2] RJ Adrian, "Twenty years of particle image velocimetry", *Experiments in Fluids*, 2005, **39**, 159–169.

[3] M Raffel, CE Willert, ST Wereley and J Kompenhans, "Particle Image Velocimetry – A Practical Guide (2nd Edition)", *Springer-Verlag*, 2007.

[4] M Raffel, CE Willert and J Kompenhans, "Particle Image Velocimetry – A Practical Guide", *Springer-Verlag*, 1998.

[5] A Schröder and CE Willert, "Particle Image Velocimetry - New Developments and Recent Applications", *Springer Verlag*, 2007.

[6] RD Keane, RJ Adrian and Y Zhang, "Super-resolution particle imaging velocimetry", *Measurement Science and Technology*, 1995, **6**, 754–768.

[7] J Westerweel, "Fundamentals of digital particle image velocimetry", *Measurement Science and Technology*, 1997, **8**, 1379–1392.

[8] JG Santiago, ST Wereley, CD Meinhart, DJ Beebe and RJ Adrian, "A particle image velocimetry system for microfluidics", *Experiments in Fluids*, 1998, **25**, 316–319.

[9] CD Meinhart, ST Wereley and MHB Gray, "Volume illumination for two-dimensional particle image velocimetry", *Measurement Science and Technology*, 2000, **11**, 809–814.

[10] MG Olsen and RJ Adrian, "Out-of-focus effects on particle image visibility and correlation in microscopic particle image velocimetry", *Experiments in Fluids*, 2000, **29**, 166–174.

[11] CD Meinhart, ST Wereley and JG Santiago, "A PIV algorithm for estimating time-averaged velocity fields", *Transactions of the ASME. Journal of Fluids Engineering*, 2000, **122**, 285–289.

[12] MG Olsen and RJ Adrian, "Brownian motion and correlation in particle image velocimetry", *Optics and Laser Technology*, 2000, **32**, 621–627.

[13] MG Olsen and CJ Bourdon, "Random error due to Brownian motion in microscopic particle image velocimetry", *Measurement Science and Technology*, 2007, **18**, 1963–1972.

[14] KS Breuer, "Microscale diagnostic techniques", *Springer-Verlag*, 2005.

[15] SM Hagsäter, CH Westergaard, H Bruus and JP Kutter, "Investigations on LED illumination for micro-PIV including a novel front-lit configuration", *Experiments in Fluids*, 2008, **44**, 211–219.

[16] SM Hagsäter, T Glasdam Jensen, H Bruus and JP Kutter, "Acoustic resonances in microfluidic chips: full-image micro-PIV experiments and numerical simulations", *Lab on a Chip*, 2007, **7**, 1336–1344.

[17] SM Hagsäter, A Lenshof, P Skafte-Pedersen, JP Kutter, T Laurell and H Bruus, "Acoustic resonances in straight microchannels: Beyond the 1D-approximation", *Lab on a Chip*, 2008, **8**, 1178–1184.

[18] SM Hagsäter, CH Westergaard, H Bruus and JP Kutter, "A compact viewing configuration for stereoscopic micro-PIV utilizing mm-sized mirrors", *Experiments in Fluids*, 2008, **45**, 1015–1021.

[19] J Estevadeordal and L Goss, "PIV with LED: Particle shadow velocimetry (PSV)", *43rd AIAA Aerospace Sciences Meeting and Exhibit – Meeting Papers*, 2005, 12355–12364.

[20] O Chételat and KC Kim, "Miniature particle image velocimetry system with LED in-line illumination", *Measurement Science and Technology*, 2002, **13**, 1006–1013.

[21] AK Singh, EB Cummings and DJ Throckmorton, "Fluorescent liposome flow markers for microscale particle-image velocimetry", *Analytical Chemistry*, 2001, **73**, 1057–1061.

[22] L Bitsch, LH Olesen, CH Westergaard, H Bruus, H Klank and JP Kutter, "Micro particle-image velocimetry of bead suspensions and blood flows", *Experiments in Fluids*, 2005, **39**, 507–513.

[23] D Sinton, "Microscale flow visualization", *Microfluidics and Nanofluidics*, 2004, **1**, 2–21.

[24] LabSmith, Livermore, CA, "Svm340 synchronized video microscope", www.labsmith.com/SVM340.html, 2007.

[25] Philips Lumileds Lighting Company, San Jose, CA, "Power light source, Luxeon K2 emitter, technical data DS51", www.lumileds.com, 2007.

[26] C Willert, "The fully digital evaluation of photographic PIV recordings", *Applied Scientific Research*, 1996, **56**, 79–102.

[27] J-M Benavides and RH Webb, "Optical characterization of ultrabright LEDs", *Applied Optics*, 2005, **44**, 4000–4003.

[28] Philips Lumileds Lighting Company, San Jose, CA, www.lumileds.com, 2008.

[29] Cree Inc., Durham, NC, www.cree.com, 2008.

[30] CD Meinhart, ST Wereley and JG Santiago, "PIV measurements of a microchannel flow", *Experiments in Fluids*, 1999, **27**, 414–419.

[31] HC van de Hulst, "Light scattering by small particles", *John Wiley & Sons Inc.*, 1958.

[32] P Vennemann, R Lindken and J Westerweel, "In vivo whole-field blood velocity measurement techniques", *Experiments in Fluids*, 2007, **42**, 495–511.

[33] H Bruus, "Theoretical Microfluidics", *Oxford University Press*, Oxford, 2008.

[34] P Skafte-Pedersen, "Acoustic forces on particles and liquids in microfluidic systems", Master's thesis, MIC – Department of Micro and Nanotechnology, DTU – Technical University of Denmark, January 2008.

[35] T Glasdam Jensen, "Acoustic radiation in microfluidic systems", Master's thesis, MIC – Department of Micro and Nanotechnology, DTU – Technical University of Denmark, April 2007.

[36] LV King, "Acoustic radiation pressure on spheres", *Proceedings of the Royal Society of London*, 1934, **147A**, 212–240.

[37] K Yosioka and Y Kawasima, "Acoustic radiation pressure on a compressible sphere", *Acustica*, 1955, **5**, 167–173.

[38] LP Gor'kov, "On the forces acting on a small particle in an acoustic field in an ideal fluid", *Soviet Physics – Doklady*, 1962, **6**, 773–775.

[39] Lord Rayleigh, "On the circulation of air observed in kundt's tubes, and on some allied acoustical problems", *Proceedings of the Royal Society of London*, 1883, **36**, 10–11.

[40] N Riley, "Steady streaming", *Annual Review of Fluid Mechanics*, 2001, **33**, 43.

[41] K Yasuda, S Umemura and K Takeda, "Concentration and fractionation of small particles in liquid by ultrasound", *Japanese Journal of Applied Physics, Part 1*, 1995, **34**, 2715–2720.

[42] K Yasuda, K Takeda and S Umemura, "Studies on particle separation by acoustic radiation force and electrostatic force.", *Japanese Journal of Applied Physics, Part 1*, 1996, **35**, 3295–3299.

[43] X Zhu and ES Kim, "Microfluidic motion generation with acoustic waves", *Sensors and Actuators A*, 1998, **66**, 355–360.

[44] Z Yang, S Matsumoto, H Goto, M Matsumoto and R Maeda, "Ultrasonic micromixer for microfluidic systems", *Sensors and Actuators A*, 2001, **93**, 266–272.

[45] RH Liu, R Lenigk, RL Druyor-Sanchez, J Yang and P Grodzinski, "Hybridization enhancement using cavitation microstreaming", *Analytical Chemistry*, 2003, **75**, 1911–1917.

[46] JC Rife, MI Bell, JS Horwitz, MN Kabler, RCY Auyeung and WJ Kim, "Miniature valveless ultrasonic pumps and mixers", *Sensors and Actuators A*, 2000, **86**, 135–140.

[47] H Andersson, W van der Wijngaart, P Nilsson, P Enoksson and G Stemme, "A valveless diffuser micropump for microfluidic analytical systems", *Sensors and Actuators B*, 2001, **72**, 259–265.

[48] M Saito, N Kitamura and M Terauchi, "Ultrasonic manipulation of locomotive microorganisms and evaluation of their activity", *Journal of Applied Physics*, 2002, **92**, 7581–7586.

[49] T Lilliehorn, U Simu, M Nilsson, M Almqvist, T Stepinski, T Laurell, J Nilsson and S Johansson, "Trapping of microparticles in the near field of an ultrasonic transducer", *Ultrasonics*, 2005, **43**, 293–303.

[50] A Nilsson, F Petersson, H Jonsson and T Laurell, "Acoustic control of suspended particles in micro fluidic chips", *Lab on a Chip*, 2004, **4**, 131–135.

[51] H Jonsson, C Holm, A Nilsson, F Petersson, P Johnsson and T Laurell, "Particle separation using ultrasound can radically reduce embolic load to brain after cardiac surgery", *Annals of Thoracic Surgery*, 2004, **78**, 1572–1577.

[52] H Li and T Kenny, "High speed particles separation using ultrasound for microTAS and lab-on-a-chip application", *26th Annual International Conference of the IEEE Engineering in Medicine and Biology Society*, 2004, **4**, 2631–2634.

[53] M Wiklund, P Spégel, S Nilsson and HM Hertz, "Ultrasonic-trap-enhanced selectivity in capillary electrophoresis", *Ultrasonics*, 2003, **41**, 329–333.

[54] BR Lutz, J Chen and DT Schwartz, "Microfluidics without microfabrication", *Proceedings of the National Academy of Sciences of the United States of America*, 2003, **100**, 4395–4398.

[55] BR Lutz, J Chen and DT Schwartz, "Microscopic steady streaming eddies created around short cylinders in a channel: Flow visualization and stokes layer scaling", *Physics of Fluids*, 2005, **17**, 1–7.

[56] J Spengler and M Jekel, "Ultrasound conditioning of suspensions – studies of streaming influence on particle aggregation on a lab- and pilot-plant scale", *Ultrasonics*, 2000, **38**, 624–628.

[57] JF Spengler, WT Coakley and KT Christensen, "Microstreaming effects on particle concentration in an ultrasonic standing wave", *AIChE Journal*, 2003, **49**, 2773–2782.

[58] LA Kuznetsova and WT Coakley, "Microparticle concentration in short path length ultrasonic resonators: Roles of radiation pressure and acoustic streaming", *Journal of the Acoustical Society of America*, 2004, **116**, 1956–1966.

[59] LS Jang, SH Chao, MR Holl and DR Meldrum, "Microfluidic circulatory flows induced by resonant vibration of diaphragms", *Sensors and Actuators A*, 2005, **122**, 141–148.

[60] R Manasseh, K Petkovic-Duran, P Tho, Y Zhu and A Ooi, "Acoustic microstreaming applied to batch micromixing", *BioMEMS and Nanotechnology II. Proceedings of SPIE*, 2006, **6036**, 485–495.

[61] M Bengtsson and T Laurell, "Ultrasonic agitation in microchannels", *Analytical and Bioanalytical Chemistry*, 2004, **378**, 1716–1721.

[62] J Lighthill, "Waves in fluids", *Cambridge University Press*, 2005.

[63] F Petersson, A Nilsson, H Jonsson and T Laurell, "Carrier medium exchange through ultrasonic particle switching in microfluidic channels", *Analytical Chemistry*, 2005, **77**, 1216–1221.

[64] JJ Hawkes, RW Barber, DR Emerson and WT Coakley, "Continuous cell washing and mixing driven by an ultrasound standing wave within a microfluidic channel", *Lab on a Chip*, 2004, **4**, 446–452.

[65] F Petersson, L Åberg, A-M Swärd-Nilsson and T Laurell, "Free flow acoustophoresis: Microfluidic-based mode of particle and cell separation", *Analytical Chemistry*, 2007, **79**, 5117–5123.

[66] F Petersson, A Nilsson, C Holm, H Jonsson, and T Laurell, "Separation of lipids from blood utilizing ultrasonic standing waves in microfluidic channels", *Analyst*, 2004, **129**, 938–943.

[67] T Laurell, F Petersson and A Nilsson, "Chip integrated strategies for acoustic separation and manipulation of cells and particles", *Chemical Society Reviews*, 2007, **36**, 492–506.

[68] JF Spengler, M Jekel, KT Christensen, RJ Adrian, JJ Hawkes and WT Coakley, "Observation of yeast cell movement and aggregation in a small-scale MHz-ultrasonic standing wave field", *Bioseparation*, 2001, **9**, 329–341.

[69] LA Kuznetsova, S Khanna, NN Amso and WT Coakley, "Cavitation bubble-driven cell and particle behavior in an ultrasound standing wave", *Journal of the Acoustical Society of America*, 2005, **117**, 104–112.

[70] O Manneberg, SM Hagsäter, J Svennebring, HM Hertz, JP Kutter, H Bruus and M Wiklund, "Spatial confinement of ultrasonic force fields in microfluidic channels", *Ultrasonics*, 2008, DOI: 10.1016/j.ultras.2008.06.012.

[71] M Sundin, A Nilsson, F Petersson and T Laurell, "Binary valving of particles using acoustic forces", *Proceedings of μTAS 2004 – 8th International Conference on Miniaturized Systems for Chemistry and Life Sciences*, 2004, **1**, 662–664.

[72] M Sundin, "Akustisk styrning av partiklar i mikrofluidiksystem", Master of Science Thesis, *The Department of Physics and Measurement Technology, Biology and Chemistry (IFM), Linköping University, Sweden*, 2004.

[73] T Scheimpflug, "Improved method and apparatus for the systematic alteration or distortion of plane pictures and images by means of lenses and mirrors for photography and for other purposes", 1904, GB Patent No. 1196.

[74] C Willert, "Stereoscopic digital particle image velocimetry for application in wind tunnel flows", *Measurement Science and Technology*, 1997, **8**: 1465–1479.

[75] AK Prasad and K Jensen, "Scheimpflug stereocamera for particle image velocimetry in liquid flows", *Applied Optics*, 1995, **34**, 7092–7099.

[76] AK Prasad, "Stereoscopic particle image velocimetry", *Experiments in Fluids*, 2000, **29**, 103–116.

[77] MP Arroyo and CA Greated, "Stereoscopic particle image velocimetry", *Measurement Science and Technology*, 1991, **2**, 1181–1186.

[78] L-G Klasen, A Leder and M Brede, "Entwicklung und aufbau eines stereo mikro PIV-system zur instantanen strömungsfeldmessung", Lasermethoden in der Strömungsmesstechnik – 13. Fachtagung der GALA e.V. 2005, GALA e.V., BTU Cottbus, 9.1–9.8.

[79] R Lindken, J Westerweel and B Wieneke, "Stereoscopic micro particle image velocimetry", *Experiments in Fluids*, 2006, **41**, 161–171.

[80] MR Bown, JM MacInnes, RWK Allen and WBJ Zimmerman, "Three-dimensional, three-component velocity measurements using stereoscopic micro-PIV and PTV", *Measurement Science and Technology*, 2006, **17**, 2175–2185.

[81] H Klank, G Goranovic, JP Kutter, H Gjelstrup, J Michelsen and CH Westergaard, "PIV measurements in a microfluidic 3D-sheathing structure with three-dimensional flow behaviour", *Journal of Micromechanics and Microengineering*, 2002, **12**, 862–869.

[82] JS Park and KD Kihm, "Three-dimensional micro-PTV using deconvolution microscopy", *Experiments in Fluids*, 2006, **40**, 491–499.

[83] S Satake, T Kunugi, K Sato, T Ito, H Kanamori and J Taniguchi, "Measurements of 3D flow in a micro-pipe via micro digital holographic particle tracking velocimetry", *Measurement Science and Technology*, 2006, **17**, 1647–1651.

[84] H Kinoshita, S Kaneda, T Fujii and M Oshima, "Three-dimensional measurement and visualization of internal flow of a moving droplet using confocal micro-PIV", *Lab on a Chip*, 2007, **7**, 338–346.

[85] MR Bown, JM MacInnes and RWK Allen, "Three-component micro-PIV using the continuity equation and a comparison of the performance with that of stereoscopic measurements", *Experiments in Fluids*, 2007, **42**, 197–205.

[86] N Chronis and LP Lee, "Total internal reflection-based biochip utilizing a polymer-filled cavity with a micromirror sidewall", *Lab on a Chip*, 2004, **4**, 125–130.

[87] C Willert, "Stereoscopic digital particle image velocimetry for application in wind tunnel flows", *Measurement Science and Technology*, 1997, *8*, 1465–1479.

[88] B Wieneke, "Stereo-PIV using self-calibration on particle images", *Experiments in Fluids*, 2005, **39**, 267–280.

[89] GE Elsinga, F Scarano, B Wieneke and BW van Oudheusden, "Tomographic particle image velocimetry", *Experiments in Fluids*, 2006, **41**, 933–947.